EXTRACTION OF ARTERIAL AND VENOUS TREES FROM DISCONNECTED VESSEL SEGMENTS IN FUNDUS IMAGES

Touseef Ahmad Qureshi

A thesis submitted for the degree of Doctor of Philosophy

July 2016

I would like to dedicate this thesis to the soul of my father

and to my loving mother . . .

Declaration

I hereby declare that except where specific reference is made to the work of others, the contents of this dissertation are original and have not been submitted in whole or in part for consideration for any other degree or qualification in this, or any other university. This dissertation is my own work and contains nothing which is the outcome of work done in collaboration

This research has been documented, in part, within the following publications:

- Qureshi, T.A., Amin, H., Hussain, M., Qureshi, R.J. and Al-Diri, B., 2012. Automatic localization of the optic disc in retinal fundus images using multiple features. In Bioinformatics & Bioengineering (BIBE), 2012 IEEE 12^{th} International Conference on (pp. 488-493). IEEE. Larnaca, Cyprus.

- Qureshi, T.A., Habib, M., Hunter, A. and Al-Diri, B., 2013, June. A manually-labeled, artery/vein classified benchmark for the DRIVE dataset. In Computer-Based Medical Systems (CBMS), 2013 IEEE 26^{th} International Symposium on (pp. 485-488). IEEE. Porto, Portugal.

- Qureshi, T., Hunter, A. and Al-Diri, B., 2014. A Bayesian framework for the local configuration of retinal junctions. In Proceedings of the IEEE Conference on Computer Vision and Pattern Recognition (pp. 3105-3110). Columbus, USA.

- Qureshi, T.A., Hunter, A. and Al-Diri, B., 2014. A probabilistic model for the optimal configuration of retinal junctions using theoretically proven features. In 22^{nd} International Conference on Pattern Recognition (ICPR) (pp. 3304-3309). IEEE. Stockholm, Sweden.

- Qureshi, T.A., A. Talal., Hunter, A. and Al-Diri, B., 2015. A Bayesian Probabilistic Framework for Accurate Classification of Retinal Vessels and Junction Configuration. In 19^{th} Medical Image Understanding and Analysis Conference (MIUA). Lincoln, UK.

Touseef Ahmad Qureshi

July 2016

Acknowledgements

I am highly thankful to my research supervisor Dr. Bashir Al-Diri, who is a subject specialist. His advices, guidance, and provisions have benefited me in the completion and success of this study. He was always available and supportive whenever I needed.

I would like to express deepest gratitude to my second supervisor Prof. Andrew Hunter, who unconditionally helped me to improve my analytical thinking, and trained me to effectively carry out the research independently. And lastly, he gave me his best to finish this manuscript.

I would like to thank all my family members including my mother, brothers, and sister for their countless prayers for my success. A special thanks to my spouse for the love and encouragement she gave to me throughout this time.

Above all, to the Great Almighty, the creator and author of all knowledge, for his limitless love and kindness.

Abstract

The accurate automated extraction of arterial and venous (AV) trees in fundus images subserves investigation into the correlation of global features of the retinal vasculature with retinal abnormalities. The accurate extraction of AV trees also provides the opportunity to analyse the physiology and hemodynamic of blood flow in retinal vessel trees. A number of common diseases, including Diabetic Retinopathy, Cardiovascular and Cerebrovascular diseases, directly affect the morphology of the retinal vasculature. Early detection of these pathologies may prevent vision loss and reduce the risk of other life-threatening diseases.

Automated extraction of AV trees requires complete segmentation and accurate classification of retinal vessels. Unfortunately, the available segmentation techniques are susceptible to a number of complications including vessel contrast, fuzzy edges, variable image quality, media opacities, and vessel overlaps. Due to these sources of errors, the available segmentation techniques produce partially segmented vascular networks. Thus, extracting AV trees by accurately connecting and classifying the disconnected segments is extremely complex.

This thesis provides a novel graph-based technique for accurate extraction of AV trees from a network of disconnected and unclassified vessel segments in fundus

images. The proposed technique performs three major tasks: junction identification, local configuration, and global configuration.

A probabilistic approach is adopted that rigorously identifies junctions by examining the mutual associations of segment ends. These associations are determined by dynamically specifying regions at both ends of all segments. A supervised Naïve Bayes inference model is developed that estimates the probability of each possible configuration at a junction. The system enumerates all possible configurations and estimates posterior probability of each configuration. The likelihood function estimates the conditional probability of the configuration using the statistical parameters of distribution of colour and geometrical features of joints. The parameters of feature distributions and priors of configuration are obtained through supervised learning phases. A second Naïve Bayes classifier estimates class probabilities of each vessel segment utilizing colour and spatial properties of segments.

The global configuration works by translating the segment network into an $\mathbb{ST}$-graph (a specialized form of dependency graph) representing the segments and their possible connective associations. The unary and pairwise potentials for $\mathbb{ST}$-graph are estimated using the class and configuration probabilities obtained earlier. This translates the classification and configuration problems into a general binary labelling graph problem. The $\mathbb{ST}$-graph is interpreted as a flow network for energy minimization a minimum $\mathbb{ST}$-graph cut is obtained using the Ford-Fulkerson algorithm, from which the estimated AV trees are extracted.

The performance is evaluated by implementing the system on test images of DRIVE dataset and comparing the obtained results with the ground truth data. The

ground truth data is obtained by establishing a new dataset for DRIVE images with manually classified vessels. The system outperformed benchmark methods and produced excellent results.

Table of contents

List of figures

List of tables

Chapter 1

Introduction

1.1 Introduction

Retinal fundus images provide an excellent resource to study the morphology of the retinal vasculature as they can provide a view up to the micro-vascular level *in vivo*. These images contain forests of mutually intersecting and overlapping arterial and venous (AV) vascular trees. These vascular trees show adaptation to various pathological conditions associated with diseases including Diabetic Retinopathy (DR), Cardiovascular and Cerebrovascular Diseases. In addition, the AVR value can be a good indicator of retinopathy of prematurity (Sun et al., 2009). Another complexity is the 'plus' disease that results in retinal vascular dilation and tortuosity (Koreen et al., 2007). Furthermore, hypertension and cardiovascular signs are being frequently associated with dilatation and elongation of retinal vessels (Cheung et al., 2011). Pathological conditions that directly influence the morphology of retinal vascular trees include generalized retinal arterial narrowing, retinal venous dilatation, neovascularization, and alteration to AVR (artery-to-venous width ratio) (Lesage et al., 2009) (Hubbard et al., 1999) (Wong et al., 2004).

Computer based automated systems can assist ophthalmologists in obtaining clinically significant information from the retinal vasculature using fundus images. These systems can potentially detect and/or predict several abnormalities at an early stage, minimize subjective opinions, reduce resource-related costs, and ultimately reduce or prevent vision loss. To support the quantitative evaluation of the clinical significance of the abovementioned morphological changes in the vasculature, efficient extraction of retinal arterial and venous trees is a prerequisite (Vickerman et al., 2009). A preliminary step before extraction of AV trees comprises of accurate segmentation of retinal vessels. Unfortunately, existing image processing techniques developed for the segmentation of retinal vessels are susceptible to several sources of error including inconsistent vessel contrast, fuzzy edges, variable image quality, media opacities, and vessel overlaps; causing them to produce partially segmented vascular networks. This complicates the process of classifying vessel segments, thus accurate AV trees extraction become extremely complex. A sample image selected with partially segmented vasculature obtained using automatic segmentation (Al-Diri et al., 2009) is given in Figure 1.1.

Consequently, the current state of the art lacks a comprehensive system for reconstructing broken segments of retinal vessels and identifying AV trees. There is a limited body of literature which addresses this issue. However, none of the available techniques have reached the level of performance required to efficiently extract AV trees from completely disconnected network of segments with complex junctions. This thesis describes a novel robust method for AV extraction from an incomplete network of segments with moderate-to-complex junctions.

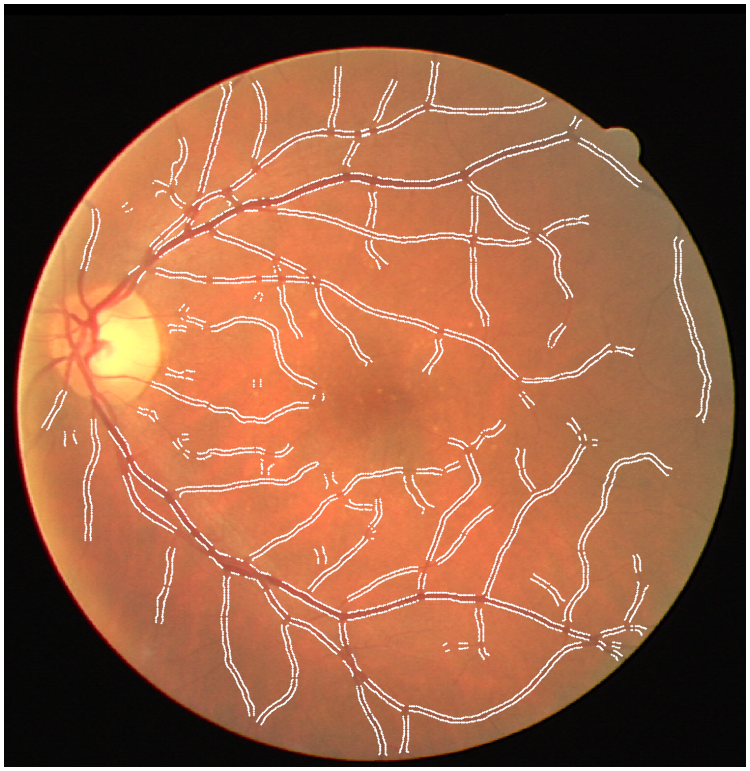

Fig. 1.1 Vessels with yellow colour showing undistinguishable vessel class.

1.2 Hypothesis

An automated image processing technique can efficiently extract arterial and venous vascular trees from a network of vessel segments disconnected at junctions in a fundus image.

1.2.1 Aims and Objectives

The aim of this work is to fully automate the reconstruction of retinal vascular network from incomplete vessel segments and to extract arterial and venous trees in fundus images. To achieve this, the objectives are:

1. To identify vessel segment junction locations.
2. To configure vessel segments at identified junction locations.
3. To classify vessels into arteries and veins.
4. To globally configure the segment networks by resolving conflicts of junction configurations among each other and extract arterial/venous trees simultaneously.

1.3 Methodology and Contributions

This thesis presents a graph based probabilistic framework for accurate extraction of arterial and venous trees from a network of incomplete segments of vessels. The components of the proposed system are based on probability theory (Bayes's theorem (Diaconis and Freedman, 1986) and MAP: Maximum A Posteriori), dependency graph theory (Markov Random Field) (Kindermann et al., 1980) (Geman and Graffigne, 1986), and inference estimation (Graph cut (Boykov et al., 2001),

Ford-Fulkerson algorithm (Ford and Fulkerson, 1956), and Max-Flow Min-Cut theorem (Ahuja et al., 1988)). They exploit underlying morphological properties of segments and bifurcations. A procedure is adopted for the translation of segments network into a dependency graph Markov Random Field (MRF). The formulated graph expresses the joint probability distribution of segment class labels and connectivity (configurations). The Bayesian posterior probabilities are estimated for mutually exclusive and collectively executive configurations at all junctions using a number of vessels' geometrical and colour features. In addition, a supervised Naïve Bayes classifier is used to estimate vessel class probabilities for vessel segments using colour and spatial features. For extraction of AV trees, the inference on the formulated graph is performed by implementing an $\mathbb{ST}$-graph cut. The performance of the proposed system is evaluated at each major phase. The system is highly stable and demonstrates excellent results overall.

The key contributions in this thesis are summarized as follow:

1. A probability-based system for creating junctions consisting of vessel segment ends. The system finds mutual associations of segments with each other at dynamically specified regions at all segment endings. Based on the strength of the segment associations, groups of segment ends are identified as junctions.

2. A Bayesian probabilistic model for estimating posterior probabilities of configuration of vessel segments locally at identified junctions. Together with the prior probabilities of configurations, the model uses conditional likelihoods of configurations estimated by considering intensity and geometrical features at segment endings.

3. A Naïve Bayes classifier for classifying vessel segments using colour and spatial features of arteries and veins.

4. A graph-based automated system for extracting arterial and venous trees. The system represents the segment network as a dependency graph Markov Random Field with a procedure for estimating unary and pairwise potentials for graph edges. A global optimal configuration of the formulated graph is inferred by implementing an $\mathbb{ST}$ graph cut using the Ford-Fulkerson algorithm. The system then re-joins extracted trees of identical class in order to resolve discontinuities occurred due to missing segments.

5. A manually class-identified gold standard vessel image set derived from the DRIVE image database (Staal et al., 2004). This dataset is publically available to the research community for the purposes of evaluation and comparison.

6. A detailed statistical analysis of morphological features of retinal vessels.

1.4 Thesis Overview

This thesis is organized as follows. Chapter 2 provides a brief medical background of the retinal vasculature, its correlation with diseases, and clinical biomarkers. Chapter 3 provides a review of literature including techniques for AV trees extraction and the general purpose techniques utilised in the proposed methodology. Chapter 4 describes two models; one for the identification of junctions to be resolved and the other for estimating posterior probabilities of all possible configurations at identified junctions. This chapter also introduces a new vessel-classified set for DRIVE images. Chapter 5 describes a novel procedure for translating the AV tree extraction problem into a general binary labelling problem expressed as a dependency graph Markov Random Field. Over these graphs, the $\mathbb{ST}$ cut is implemented using the Ford-Fulkerson algorithm. This chapter also includes tasks including detection of disjoint

network of segments, vessel classification, global configuration, and tree joining. Chapter 6 describes the implementation of the proposed system and each major task separately. The experimental evaluation is performed by comparing the system's outcome with the ground truth data and with the outcome of other available systems. This chapter also provides a critical analysis of the techniques used in the proposed methodology. Chapter 7 concludes the thesis and gives recommendations for future work. The overall pipeline overview of the Thesis is shown in Figure 1.2

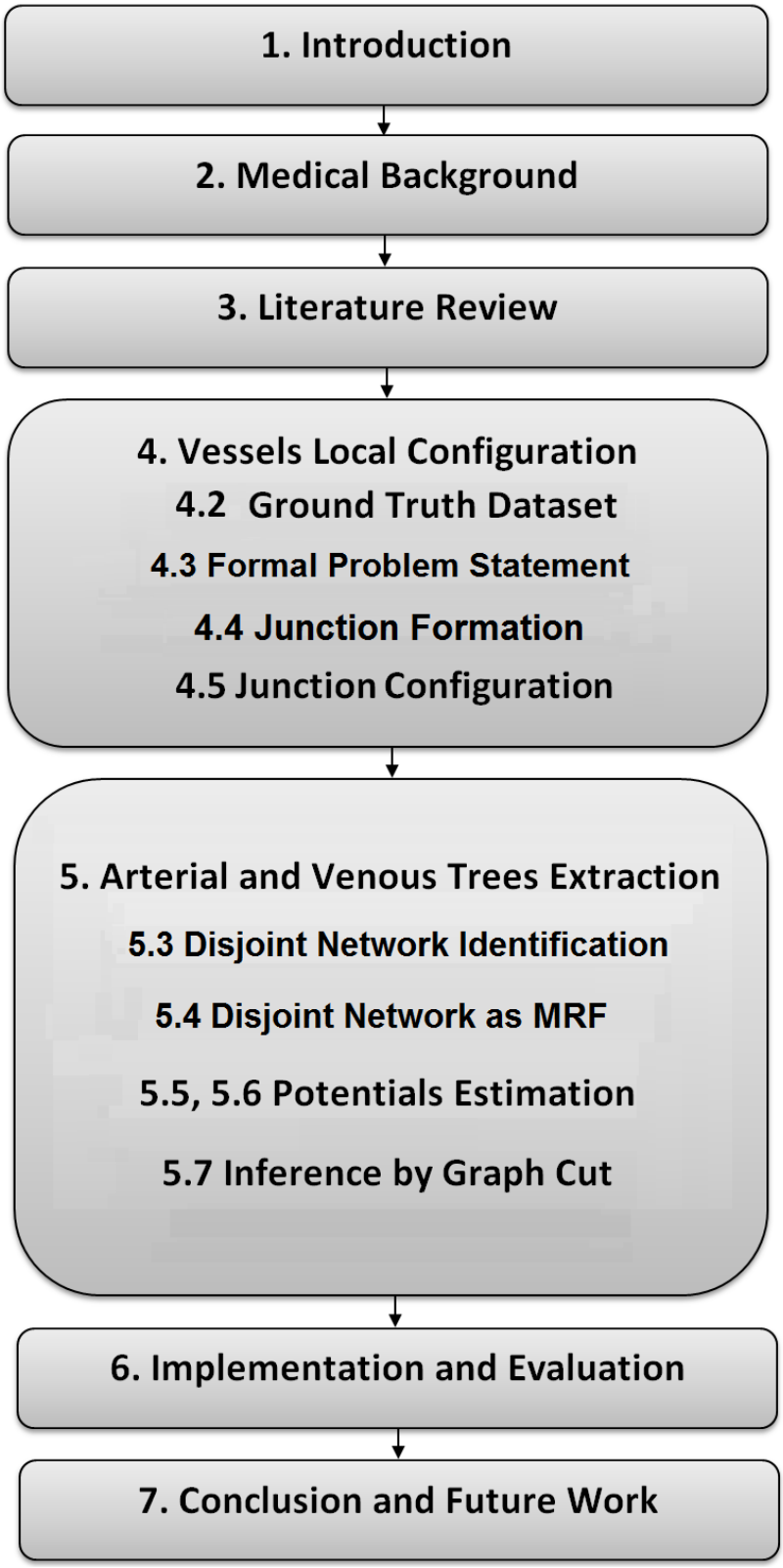

Fig. 1.2 Pipeline Overview for the Thesis

Chapter 2

Medical Background

2.1 Introduction

The human retina is a unique window to the health condition of the whole body. It is of significant value for many non-invasive clinical and subclinical tasks. Diabetic Retinopathy (Danis and Davis, 2008), Macular Degeneration (Bird et al., 1995), Retinal Detachment (Committee et al., 1983), and Retinoblastoma (Knudson, 1971) are some common conditions that may lead to blindness, and are manifested on the retina. Ophthalmologists use a variety of methods including ophthalmoscopy (fundoscopy) to examine the retina for diagnostic and predictive purpose.

Fundoscopy (Hoyt et al., 1973) is a technique for examining the interior of the eye using a specialized fundus camera. The fundus camera is attached to a low-power microscope that provides a moderate-to-high angle (optos) (Silva et al., 2012) view of the retina. For examination, ophthalmologists obtain photographs or real-time videos of the interior of the retina on computers systems attached to these cameras. These systems might come with image processing techniques for automatic detection

of landmarks in the fundus images.

The retinal vasculature is a prominent retinal feature with distinctive importance from the disease diagnostics viewpoint, and can be viewed clearly in fundus images. Morphological changes in the retinal vasculature have been quantified for detection, prediction, and/or grading of a range of pathological disorders. Early detection of clinically-significant features in the retinal vasculature can help to prevent vision-loss and several life-threating diseases including systemic complications such as cardio-vascular diseases. The ocular manifestation of various pathological abnormalities is examined by analysing geometrical and spatial information of vasculature during retinal screening. The AVR (artery-to-vein ratio), vessel bifurcation features, LDR (length-to-diameter ratio), vessel tortuosity, and fractal properties of vascular trees are potential landmarks considered by ophthalmologists for disease diagnostic purpose. This chapter discusses some common retinal vascular features and discusses their clinical significance.

2.2 Anatomy and Functionality of Retina

The retina is the light-sensitive inner layer in the eye. It is a non-invasive brain tissue of the central nervous system (CNS). It consists of two types of neurons (photoreceptor cells): rods and cones. The function of rods is to provide vision in dim light, whilst cones are responsible for colour perception in daylight. Light from the external environment striking the retinal layer is converted into nerve impulses through chemical and electrical reactions and which are then transmitted to the brain along the optic nerve. The anatomy is shown in Figure 2.1.

Described below are the retinal layer components of interests for this thesis. A normal fundus is also shown in Figure 2.2.

- The Macula (Macula Lutea) is an oval-shaped dark pigmented area in the centre of retina and is responsible for central vision. The anatomical macula has diameter 5.5 mm (0.22 in) whilst clinical macula is 1.5 mm (0.059 in) in healthy retina (Lyle, 1995). The macula is of a special importance from a clinical significance standpoint, as any damage to it, generally referred as Maculopathy, may lead to complete loss of central vision. The Fovea (Fovea Centralis) is the small pit in the Macula that provides the sharpest vision details.

- The Optic Nerve Head (ONH) or Optic Disc, the brightest area in the retina, represents the opening of the cranial nerve (optic nerve) which is responsible of transmitting visual information from retina to the brain. The ONH is also the entry point of major blood vessels to the retinal layer. Damage to ONH can be caused by various pathological complications generally referred as Glaucoma diseases that may lead to vision loss.

- The retinal blood vessels nourish the inner layer of the retina. These vessels emerge out of the ONH and spread through the perfusion area by means of branching and thinning, forming mutual overlaps of arterial and venous trees. The smallest diameter vessels arterioles and venules in the retina are connected to each other via the capillary bed making up the microcirculation. The morphology of the retinal vessels follows certain physiological principles, and may alter in response to disease, and thus has great importance from a clinically significance standpoint. There are many medical studies available on qualitative and quantitative aspects of the retinal vascular morphology, associating retinal

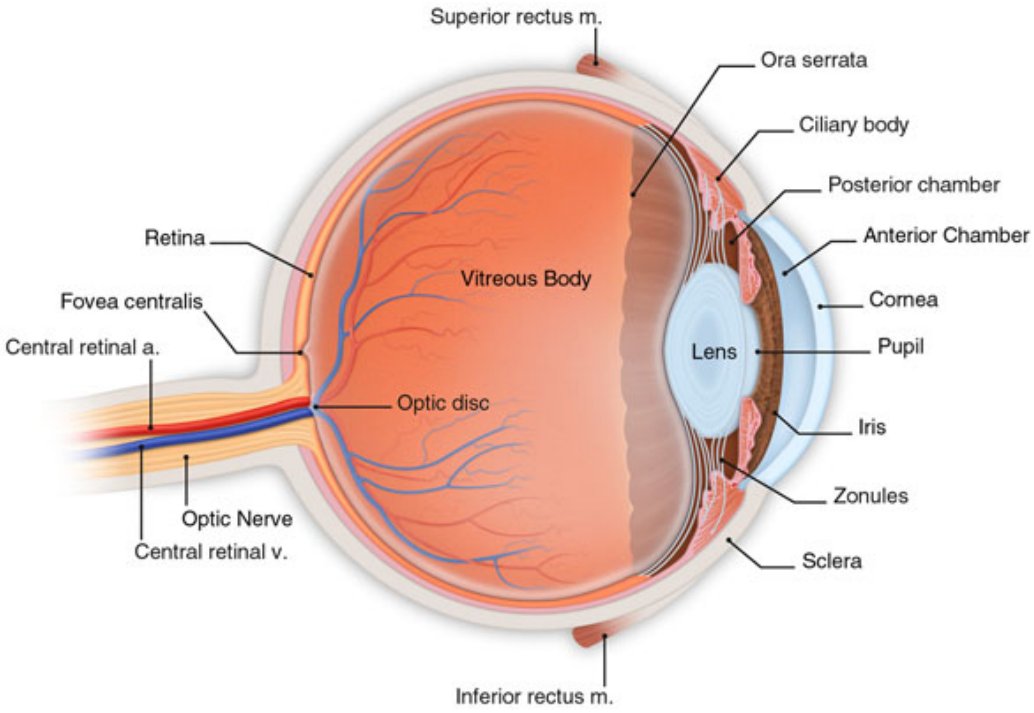

Fig. 2.1 The anatomy of the eye taken from http://www.sneretina.com/retinal-diseases-and-treatments/

vascular adaptation to various life-threatening risks including cardiovascular, cerebrovascular and systemic diseases.

2.3 Retinal Vascular Adaptation to Diseases

Retinal vascular features are the potential biomarkers for a number of disease families including cardiovascular, cerebrovascular and systemic complications. The diseases with their diagnosable symptoms associated to vasculature are described below.

2.3.1 Systemic Diseases

A systemic disease is one that directly/indirectly affects a number of organs and/or tissues potentially including the retina. The systemic diseases affecting the topogra-

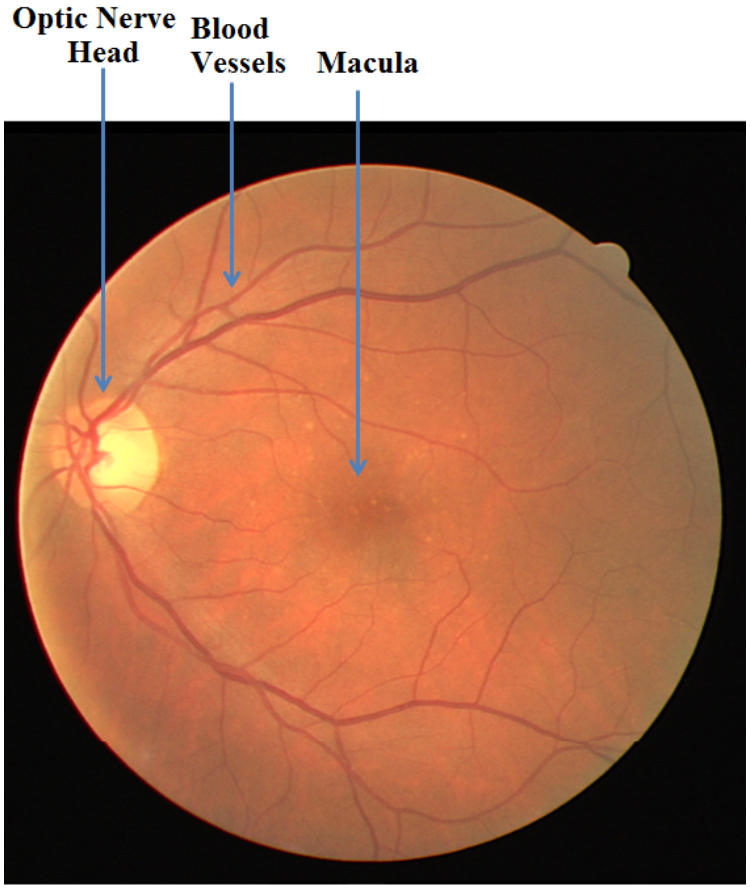

Fig. 2.2 Normal Fundus Image from DRIVE dataset

phy of retinal vasculature (Hayreh et al., 2001) includes nephropathy, atherosclerosis, renal diseases including retinopathy and its variations such as hypertensive retinopathy, and diabetic retinopathy which is one of the leading causes of blindness in developed countries.

2.3.2 Cardiovascular Diseases

Cardiovascular diseases affect the heart and blood vessels. Studies have proven direct associations between physiological and pathological alterations in the retinal vasculature with several cardiovascular complications (Wong et al., 2001) including

hypertension, coronary heart disease (CHD), and congestive heart failure. The most prominent symptom of cardiovascular diseases observed in the retinal vasculature are arterial narrowing, smaller AVR (Artery to Vein ratio), and venular dilation.

2.3.3 Cerebrovascular Diseases

The strongest evidence for the association between the retinal and cerebral vasculature is the identical nature in terms of anatomical features, physiological characteristics, and embryological origin of both vasculatures. It is the common practice to analyze the retinal vasculature to indirectly study the cerebral vasculature (GOTO et al., 1975). For instance, fibrous and fibro-hyalinoid thickenings of the retinal major arteries have direct associated with changes in the intracerebral arteries. Studies have also proved that changes to retinal major arteries are a potential signs of cerebral hemorrhage and infarction (GOTO et al., 1975).

2.4 Retinal Vascular Morphology as a Clinical Biomarker

Alterations to the topological features of vascular trees can provide indications of above-mentioned diseases. These features are discussed below.

2.4.1 Fractal Properties of Retinal Vessel Trees

Several studies have shown quantitative and qualitative correlations of the fractal dimension of retinal trees with a number of conditions. The Fractal analysis of retinal vessel trees characterizes the complexity of the global geometry of the retinal vasculature. In the medical literature, there exists various empirical and theoretical studies regarding the fractal properties of the retinal vasculature; several computer-

based algorithms have been introduced to perform automated analysis of the fractal dimension of retinal vessel trees (Masters, 2004) and (Stošić and Stošić, 2006).

2.4.2 Vessel Bifurcation

The features at vessel bifurcations are perhaps the most studied and significant clinical markers. Each feature at bifurcation has been investigated independently and in correlation with other features; for instance, the vessel diameters and vessel angles at bifurcation have been theoretically proved to have strong interdependence. Zamir (Zamir et al., 1979) and Murray (Murray, 1926) theories on bifurcation features are being widely accepted by the research community. Some of the common bifurcation features include the asymmetry ratio, bifurcation index, diameter ratio, area ratios, length ratios, and bifurcation angles.

2.4.3 Artery to Venous Ratio

A quantitative feature that has been studied by several authors is the ratio of arterial to venous diameter (AVR), which is extracted by measuring major veins and arteries radiating from the optic nerve head. The AVR has been used as a clinical indicator as it is highly sensitive to arterial narrowing. The feature has been empirically observed and several authors have provided a quantitative range of AVR (King et al., 1996). The AVR value is also regarded a good indicator of retinopathy of prematurity. In addition, an abnormal AVR value is the sign of high blood pressure and pancreas disease (Kondermann et al., 2007). These pathologies include venous dilatation, clot blockage in arteries/veins, i.e. Central retinal artery occlusion (CRAO) (Beatty and Eong, 2000) and Central retinal vein occlusion (CRVO) (Hayreh, 2015).

2.4.4 Vessel Tortuosity and Vessel Length to Diameter Ratio

The vessel tortuosity or the degree of vessel tortuousness is a qualitative indicator for abnormalities such as 'plus' disease. However, more recently it has been observed as a quantitative feature and different methods are proposed for its measurements.

The length to diameter ratio or LDR is a significant clinical biomarker and is measured between consecutive bifurcations. The LDR has a direct correlation with general arterial narrowing and rarefaction as it tends to increase in the presence of these complications. Both of these complications arise as the result of hypertension.

2.5 Conclusion

Medical studies provide evidences that a number of cardiovascular, cerebrovascular, and systemic diseases directly affect the morphology of the retinal vasculature. A number of physiological alterations in the retinal vasculature can be served as clinical biomarkers for complications such as hypertension, stroke and diabetic retinopathy. The literature provides various measurement tools for describing vascular features including AVR, LDR, vessel tortuosity, and bifurcation features. It is therefore arguable that a comprehensive analysis of the retinal vasculature in terms of feature measurements may provide the basis for early diagnostics and prevention of several diseases. However, extracting such measurements manually or semi-manually is time consuming exercise and unreliable, which suggests that automated extraction of measurement is desirable. A vital step towards this analysis is the accurate extraction of arterial and venous trees.

Chapter 3

Literature Review

3.1 Introduction

The retinal vasculature consists of mutually overlapping arterial and venous trees. These trees show adaptation to several pathological disorders manifested in fundus images. To study the association of retinal vascular changes to various diseases, segmentation and classification of retinal vessels is a prerequisite. Inefficient segmentation yields errors including disconnected, missing, and/or false segments.

This chapter describes the state of art techniques for solving problems including classification of retinal vessels, local configuration of vessel segments, and extraction of AV trees by globally configuring and classifying disconnected vessel segments. The classification of retinal vessels is challenging but a long known problem, and therefore a good number of techniques are available. Some elegant techniques have been reported that disregard the classification of retinal vessels and locally resolve dis-connectivity in a partially segmented vasculature to obtain binary segmented

trees. This approach has two major limitations; firstly the configurations at junctions in extracted binary trees may conflict with each other as the junctions are resolved independently from each other. This may yield non-consistent binary trees. Secondly, the system doesn't classify the extracted trees. Efficiently extracting AV trees from fully disconnected network of vessel segments by globally configuring all the junctions and classifying all segments is relatively new area. To the best of our knowledge, only three techniques have been reported so far that purely address this problem. This thesis addresses the same task.

In the second half of this chapter (in Section 3.3), the techniques utilised in the proposed methodology described for AV trees extraction in this thesis, are briefly reviewed. The overall methodology is designed under the domain of dependency graph and probability theory. This includes, Bayesian probability models that have been designed for many purposes including classification in a vast range of domains. In addition, an advanced graphical model named Markov Random Field, which is the premier choice for expressing the joint probability distribution of priors and likelihoods. Moreover, a number of inference techniques including Maximum a Posteriori estimation through exhaustive search, as well as graph cuts to get optimal solutions, are being frequently used by experts, and which are also the part of the proposed methodology.

3.2 Review of the Current State of Art

3.2.1 Local Configuration of Vessel Segments

The local configuration of retinal vessel segments refers to connecting the segment ends with each other locally at each junction. All possible configurations at each junction are considered independently, i.e. without the knowledge of configurations at other junctions–followed by selecting the most likely configuration estimated by probability or any cost functions. Very few comprehensive techniques have been developed for configuring the segments at junctions.

The most recent technique, developed in (Favali et al., 2015), obtains a connectivity kernel using the Fokker-Planck equation that utilises the geometrical structure of multi-orientation cortical connectivity of vessels. By using the spectral clustering on a large local affinity matrix, constructed by both the connectivity kernel and the feature of intensity, the vessels are identified successfully in a hierarchical topology each representing an individual perceptual unit. The method resolves crossings by considering the local variation of orientation and intensity features using the Euclidean distance between the intensities of blood vessels. The approach is implemented using normalized affinity matrix that keeps the discriminative information vessels at crossings.

The work produced in (Al-Diri et al., 2010) performs perceptual grouping of retinal segments at disconnected junctions using self-organizing feature map (SOFMs) that uses the cost functions for configuration. This method works by first identifying isolated segment ends as leaves (terminal segments), with the others labelled as *joinable segment ends* (JSEs). The centrelines of JSEs are progressively extended until

it terminates or reaches the body of another segment. Using a set of rules, the groups of segment ends are identified in local JSE sets. These sets are then independently resolved using cost functions that gives low value for plausible junction geometry by considering the plausibility of all possible configurations. The cost functions utilise the intensities, widths and angles of the segment ends at local JSE sets. In addition, the method detects overlapping segment whenever a segment appears with over-width.

In addition, a vessel tracing algorithm reported in (Tsai et al., 2004) can identify simpler cases such as bifurcations and crossings at disconnected/connected junctions. The method works in three phases. Firstly, the seed points on the vessels are gathered, then by recursively tracing the seed points along the vessel centreline assuming an antiparallel edge model, and finally the local regions are identified. Each region is the point of intersection of vessel directions, and is identified as bifurcation or crossing depending on the number of vessels composing the region.

Moreover, a supervised probabilistic model is developed for local configuration of segments at true junctions in (Qureshi et al., 2014) and which is also one of the contributions of this thesis. The details of this method are provided in next chapter.

Furthermore, to the best of our knowledge, there are two techniques (described below) in the literature that performs global configuration of segments to obtain forests of binary trees.

Lin et al. (Lin et al., 2012) used curvature, width and intensity of segments as features, and an extended Kalman filter to resolve the connectivity at bifurcations

and crossings for extracting binary trees. This methodology works in three steps: 1) the extended Kalman filter is used to iteratively correct and learn the continuity pattern of a disconnected segment; 2) the system selects the next segment, with the highest continuity, in the close neighbourhood of previous segment; 3) grouping of previous and next segment using minimum cost matching algorithm to resolve the conflicts in configurations. In addition, their method performs global configuration, and extracts trees, however doesn't identify the classes of trees.

A similar approach adopted by Lau et al. (Lau et al., 2013) that extracts optimal forests of binary trees in a specified region of interest (ROI). Their methodology works by detecting the crossover points, and then by extracting optimal forests of trees using on a rule-based model. The crossover points are detected using the segment intensity, angle, and width. This technique attempts to globally configure binary trees consisting of major vessels in limited zones.

3.2.2 Classification of Vessel Segments

The accurate classification of retinal vessels provides an opportunity to extract potential clinical features (such as AVR, etc.) for diagnosis of various pathologies. In addition, the classification of retinal vessels is also a prerequisite for studies involving analysis of microcirculation of retinal vascular system, and hemodynamic of blood flow in arterial and venous vessels. A number of techniques have been presented for classifying the retinal vessels in fundus images, which utilise features including geometry (e.g. arteries are thinner than veins), colour (e.g. arteries are brighter than veins), and topographical information (e.g. crossing vessels are invariably from

opposite class) of vessels. These features are local and relative, and thus classification is challenged by variable local and image contrast, media opacities, and variable reflective properties of vessels (specular highlights, “silver wiring”). Some of these classifiers are discussed below.

One of the earliest attempts to classify retinal vessels in fundus images was made by Li et al. (Li et al., 2003). They presented a very efficient piecewise Gaussian model for extracting the intensity profile of major retinal vessels. The model put considerable importance to central reflex in the vessels which is utilised as a filter on the image for classifying vessels. They used a minimum Mahalanobis distance classifier to differentiate retinal vessels. In addition, they performed a comparison of single Gaussian with piecewise Gaussian model and concluded that the latter is far appropriate than former. They utilise intensity distribution of the cross section of blood vessel in the green channel of the image. They argue that green plane is the clearest channel in the retinal images whilst red is usually saturated and blue is too dark. They tested their model using a large number of major segments and reported good results. During the same year, Grisan et al. (Grisan and Ruggeri, 2003) reported a technique in which the colour features including red values and the mean of the hue values of the pixels were used to classify vessels. They first divided the retinal image into four quadrants within concentric zone around the optic nerve head. This enabled their system to control the discrimination of vessels locally in each quadrant. Features extraction and classification process is performed in each quadrant independently from other quadrants.

In addition, Kondermann et al. (Kondermann et al., 2007) trained two classifiers based on neural networks and SVM (Support Vector Machine); and was able to

classify major vessels to a good extent. They also introduced two feature extraction methods-one for vessel profile features and other for vessel ROI based feature vectors. The multiclass PCA method was used to reduce to dimensionality of feature vectors. In addition, before extracting the features, they process the image to remove the shading effect. Similarly, Narasimha-lyer et al. in (Narasimha-Iyer et al., 2007) reported an SVM classifier that uses both functional and structural features of retinal vessels. The structural features exploited the central reflex of vessels whilst the functional feature includes ratio of the vessel optical densities for oxygen-sensitive and oxygen-insensitive wavelengths obtained from arteries and veins.

Moreover, Zamperini et al. (Zamperini et al., 2012) has used width and colour features of vessels for a number of classifiers including K-Nearest-Neighbour, Support Vector, and Quadratic Bayes Normal classifiers. They compared the outcome of all classifiers, founding Quadratic Bayes Normal classifier with best results. Furthermore, A graph-based technique is introduced in (Rothaus et al., 2009) for classifying retinal vessels. The anatomical characteristics of the retinal vasculature are modelled as dual constraint graph. The technique works by means of manually labelling few major segments, followed by propagating the labelling across the vascular graph using a set of domain specific rules.

Recently, a graph-based approach for classifying vascular trees is introduced in (Dashtbozorg et al., 2014). They used the segmented retinal vasculature to obtain a graph consisting edges and nodes that denote segments and segment intersection points respectively. The graph links (segments) at intersection points are labelled from one of two vessel classes. For labelling of links, they utilise vessels features

including intensity, angle, orientation, and width. Another recent work published in (Eppenhof et al., 2015) has proposed an AV classification model via graph cut optimization. The main focus of their work is on classification of major vessels using the contextual information mainly obtained from bifurcations and crossings. There is a significant difference between their proposed technique and ours in terms of the inference techniques utilised, segments and dataset used, and the pairwise potentials proposed.

It is noted that in all the publications discussed above the basic features utilised for discriminating vessels into arteries and veins are nearly the same, i.e. hue, saturation and intensity of vessels. The only difference is the classification model proposed to use these features. In this thesis, a novel method for classifying vessel segments using colour, physiological, and the spatial features of retinal vasculature is introduced. To the best of our knowledge, this is the first time spatial features of retinal vessels are thoroughly analysed and used as potential indicator for vessels classification. The classification framework is designed using a Bayes probability model in conjunction with graph cut for global labelling of both major and minor vessels.

3.2.3 Global Optimal Configuration for Extracting Arterial and Venous Trees

Automated extraction of arterial and venous trees from a network of disconnected retinal vessel segments at junctions is an important and relatively new task. This task comprises of local configuration and classification of segments simultaneously through a sophisticated procedure ensuring no conflicts of local configurations (i.e.

global configuration) among each other. To the best of our knowledge, there are only two techniques available in literature (Joshi et al., 2014) and (Hu et al., 2015) that purely address this task.

The most recent method introduced in (Hu et al., 2015) for extracting AV trees by globally configuring the segment network. The method works in three major steps: 1) identifying and separating the connected points in the segmented vasculature, followed by estimating costs of local configurations, 2) calculating global configuration costs, followed by extracting multiple anatomical trees using graph-based metaheuristic algorithm for optimization, 3) classifying the extracted binary trees into AV trees.

Joshi et al. (Joshi et al., 2014) have introduced a method for extracting AV trees by finding an optimal Dijkstra's graph search using orientation, width and intensity for segments' configuration whilst colour properties of vessels for classification. The first phase of their method works by obtaining the binary segmentation of retinal vasculature. In the segmented vasculature, the bifurcation, crossing and terminal points are identified and separated to obtain singleton segments. In the second phase, the segment network is represented as graph by denoting the segments as nodes, and their associations as edges. The Dijkstra's graph searches the minimum edge cost path between nodes. The function that estimates the cost path between any two nodes uses orientations, widths and intensities of segments corresponding to nodes. The Dijkstra's graph search yields several paths (sub-graphs), each consisting of a number of segments. In the third phase, they used fuzzy C-means clustering method to classify the extracted graphs (trees) into one of the two vessel classes.

For an efficient extraction of AV trees, a novel graph based comprehensive procedure is presented in this thesis. The method is highly appropriateness for the given application (AV trees extraction task) from both algorithmic and theoretic viewpoint. The main advantage of our system over the existing techniques is that it addresses two problems (classification and connectivity) by integrating them into a single model. On the contrast, the existing techniques solve each of these tasks separately losing the opportunity to efficiently make the two tasks as complimentary processes. Moreover, the existing models don't fully exploit spatial features of vessels as we did. Finally the existing techniques use greedy algorithms and don't exhaustively go through the search space for vessel configurations. A complete comparison of technical issues between proposed AV extraction method and the current state of art is provided in evaluation Chapter 6.

3.3 Review of Techniques for Proposed Methodology

The framework of the proposed methodology is designed mainly under the domain of probability theory. The principle elements utilised are the Naïve Bayesian formulation, dependency graph model, and graph-cut based inference using the Ford-Fulkerson algorithm. The following sections of this chapter provide theoretical and application based details of the aforementioned techniques.

3.3.1 Naïve Bayes Probability

The Naïve Bayesian probability model (Bernardo and Smith, 2001) is a statistical model which forms its basis on Bayes' theorem (Bayes' law or Bayes' rule). The Bayes' theorem states that the posterior probability of an event A given event F is

equal to conditional probability of event F given A times the prior probability of A. Mathematically, it is written as:

$$p(A|F) = \frac{p(F|A)p(A)}{p(F)} \tag{3.1}$$

Whereas, $p(A|F)$ is posterior probability, $p(F|A)$ is conditional probability of event F given A, $p(A)$ is prior probability of event A, whilst $p(F)$ is the prior probability of event F and is used as normalizing constant in Bayes' theorem.

In addition, the Maximum a Posteriori (or *MAP*) estimation is the mode of posterior distribution. Precisely, it refers to the object class with highest posterior probability estimated through bayes' formula as given:

$$\hat{\delta}_{MAP}(x) = \underset{\delta}{argmax}\, p(x|\delta)p(\delta) \tag{3.2}$$

Whereas, δ is the class label and x is feature vector.

3.3.2 Markov Random Field

Dependency graph models are the probabilistic tools for expressing the joint probability distribution of a system. The Bayesian Network (Friedman et al., 1997) and Markov Random Field (MRF) (Kindermann et al., 1980) are two major 2-D graph models capable to express dependencies (as edges) among random variables (nodes). The key difference between the two models is that formulizing Bayesian Network requires distinct dependencies, i.e. directions of edges among the nodes are required such that the established graph remain acyclic; whilst Markov Random Fields can be undirected (or bidirectional) and can be cyclic.

Formally, the Markov Random Field is a graphical model (2D Graph), as shown in Figure 3.1 of a set of random variables with Markov properties expressed as an undirected graph. The three Markov properties of an MRF graph are explained as:

Let $G = (V, E)$ is an undirected graph of random variables $Z = (Z_a)_{a \in V}$, then the graph G is said to be MRF if following are true:

- Pairwise Markov Property: Any two non-adjacent variables (nodes) in G are conditionally independent given all other variables, i.e.

$$Z_a \perp Z_b | Z_{V \setminus \{a,b\}}, if \{a,b\} \notin E \tag{3.3}$$

- Local Markov Property: Given its neighbor, a variable in G is independent of all other variables, i.e.

$$Z_b \perp Z_{V \setminus close(b)} | Z_{neigh(b)} \tag{3.4}$$

- Global Markov Property: Any two subsets (A and B) of G are conditionally independent given a subset S of G partitioning A and B, i.e.

$$Z_A \perp Z_B | Z_S \tag{3.5}$$

3.3.2.1 Markov Random Field in Computer Vision

During the last few years, the MRF models have become the premier choice for addressing numerous high, mid and low-level vision problems (Wang et al., 2013) (Li, 2009). A variety of vision problems including classification (Solberg et al.,

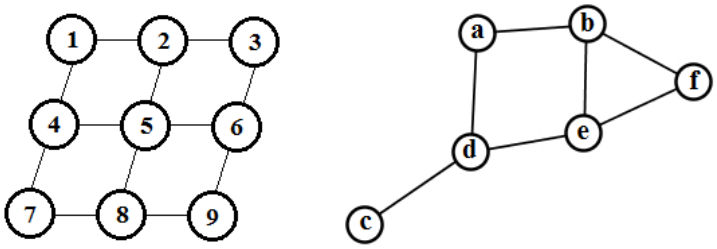

Fig. 3.1 A sample of two possible MRF graphs

1996), segmentation (Yang and Jiang, 2003) (Kato and Pong, 2006), optical flow (Heitz and Bouthemy, 1993), motion analysis (Tsai et al., 2012), and many others have been expressed in pair-wise or higher-order MRFs.

Vision problems in the context of MRF models are typically treated as energy minimization problems (Szeliski et al., 2006). In segmentation, individual pixels may be treated as nodes with four or eight connected dependencies to their neighbours (see Figure 3.1). Each node (pixel) possess unary potential (or singleton potential), whilst the edges between nodes encode the contextual constraints referred as pairwise potential. Informally, the unary potential (unary term) is the compatibility of the pixel with a specific label, and the pairwise potential is the compatibility of neighbouring labels. The MRF energy has the following form:

$$E(Z) = \sum_{i \in V} \Phi_i(z_i) + \sum_{(i,j) \in E} \Phi_{ij}(z_{ij}) \tag{3.6}$$

For instance, given an MRF representing a grid of pixels of an image (shown in Figure 3.2), the objective is to find an optimal classification of pixels into foreground and background. In this case, the unary potential of each pixel is the likelihood of the pixel as background or foreground. This could be a value representing the probability of the pixel belonging to a specific class based on its own features. The

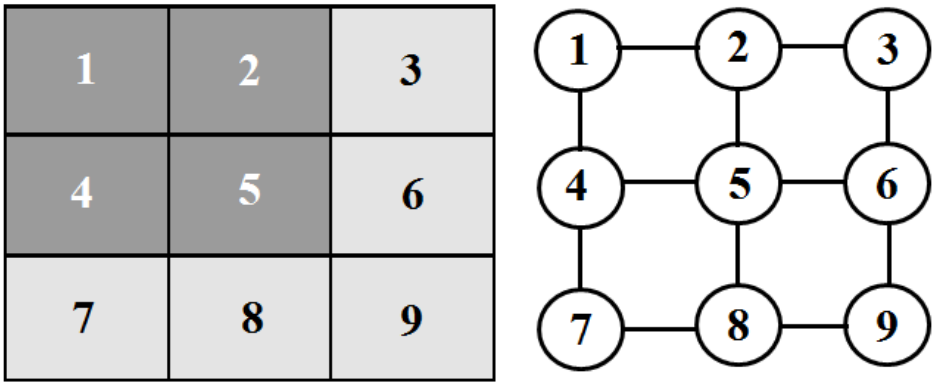

Fig. 3.2 A grid of pixels with its corresponding MRF.

pairwise potential typically expresses smoothness between neighbouring pixels defined as strength of connectivity in the graph. Thus, the pairwise potential expresses a cost term (probability of connectivity) that penalizes the variation of states between neighbouring nodes.

In the domain of computer vision, most of the MRF-based applications denote nodes as the grid of image pixels; however, the representation is not limited to image pixels only. There are several applications such as in (Saund, 2006) and (Bianco et al., 1999) in which the nodes of MRF-graph denote objects/states rather than image pixels. The crucial step is the formulation of the logic of interaction among these variables (objects) in the framework of heterogeneous Markov Random Fields.

To this end, minimizing the aforementioned energy function using an appropriate inference technique could yield in disjoint graphs that correspond to optimal classification of pixels.

3.3.3 Inference on Markov Random Field

Inferring an optimal configuration on the formulated MRF is a key task. Various families of inference techniques exist each with its strength and weakness including Iterated Conditional Mode, Simulated Annealing , Loopy Belief Propagation, and Graph Cuts. The Iterated Conditional Modes (Besag, 1986) are the most computationally efficient methods for optimizing MRF energy, which work by iteratively maximizing the joint probability of each variable conditioned on rest. However, these methods lack the ability to obtain good optimums (Wang et al., 2013). On the other hand, the Simulated Annealing (SA) (Geman and Geman, 1984), (Blake and Zisserman, 1987), (Tupin et al., 1998), are the probabilistic techniques to obtain global optimum solution in large search space. The SA is a metaheuristic approach which works by interpreting slow cooling as a slow decrease in the probability of inferring bad solutions. In theory, Simulated Annealing methods obtain guaranteed global optimum solutions; however, these methods are considered impractical from computational cost viewpoint (Wang et al., 2013). A relatively advanced approach is Loopy Belief Propagation (Weiss and Freeman, 2001), (Freeman et al., 2000), (Felzenszwalb and Huttenlocher, 2006), for estimating approximate inference on probabilistic graphical models. These methods, also known as sum-product message passing techniques, are the message passing algorithms that calculate the marginal distribution of unobserved nodes conditioned on observed nodes. These methods perform very well in regard to computational cost, and obtaining optimum solutions.

In recent years, the graph cut approach (Boykov et al., 2001), (Greig et al., 1989), (Roy and Cox, 1998), (Boykov et al., 1998), (Ishikawa and Geiger, 1998) gained importance due to the strong theoretical support of max-flow min-cut theorem

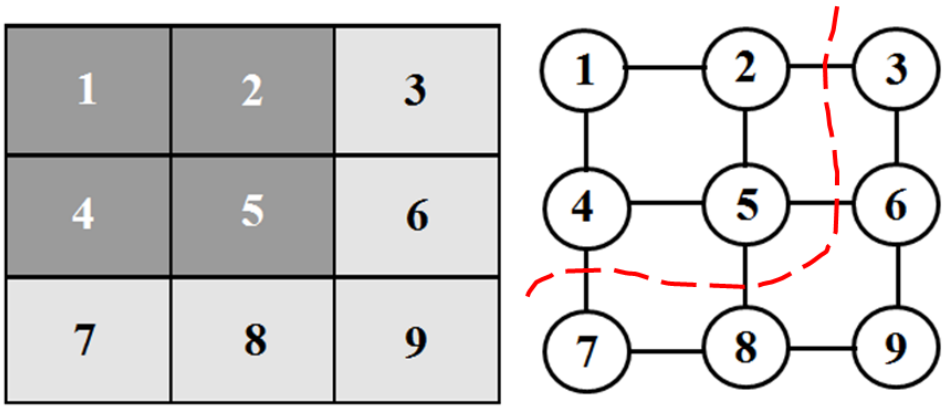

Fig. 3.3 An optimal cut is shown severing the graph that results in pixels classification.

and computational efficiency. These are powerful alternatives to abovementioned techniques and thus have been utilised in numerous vision problems, including binary labelling problems. In this thesis, the graph cut approach is utilised for finding the global optimal configuration on MRF.

3.3.3.1 Graph Cuts

In the domain of graph theory, a graph-cut is the separation of a given graph by means of partitioning the vertices into two or more disjoint subsets (as shown in 3.3) that is minimum or maximum in some sense depending on the application purpose. To this end, the minimum graph cut techniques can be employed to efficiently solve a wide range of computer vision problems (represented in MRF graphs) including image smoothing, segmentation, labelling, and energy minimization tasks. The MRF based energy minimization tasks (Equation 3.6) are typically reduced to the maximum flow problem; and thus, solved by finding the minimal cut using the max-flow min-cut theorem. Under binary problem formulation, the minimum energy solution using graph cut finds a globally optimal solution, which often corresponds to maximum posteriori estimate solution. In the following paragraphs, the max flow problem, the

Ford-Fulkerson algorithm, max-flow min-cut theorem, and ST-cut is described in detail.

3.3.3.2 Max Flow Problem

In optimization theory, max flow problems are described maximizing the flow in a source-sink flow network as shown in 3.4(a). In a flow network, the edges have specific directions and capacities (weights). The objective is to maximize the flow from source node (S) to sink node (T) such that the capacities of the edges are not saturated. This formulation of Max Flow was coined for the first time by T.E. Harrris and F. S. Ross to model Soviet railway traffic flow in 1954. Later in 1955, two mathematicians Lester R. Ford, Jr. and Delbert R. Fulkerson solved the max flow problem by introducing the Ford–Fulkerson algorithm.

3.3.3.3 Ford-Fulkerson Algorithm

The Ford-Fulkerson algorithm (Ford and Fulkerson, 1956) or FFA is a method to find the maximum flow in a flow network by iteratively finding the augmenting paths in a residual graph until there is no path left from source to sink. With this approach, several implementation of FFA are available in literature. Let $G(V,E)$ be a graph with source ($\mathbb{S}$) and sink ($\mathbb{T}$) node, capacity $c(u,v)$ for each edge $e(u,v)$ from u to v, and flow $f(u,v)$ from u to v. The FFA finds the maximum flow from $\mathbb{S}$ to $\mathbb{T}$ while maintaining the following constraints:

The flow along an edge never exceeds its capacity, i.e.

$$\forall(u,v) \in E f(u,v) \leq c(u,v) \tag{3.7}$$

The total flow from u to v is always equal to total flow from v to u, i.e.

$$\forall(u,v) \in E f(u,v) = -f(v,u) \tag{3.8}$$

The net flow leaving source node S must be equal to net flow arriving at T, i.e.

$$\sum_{(\mathbb{S},u)\in E} f(\mathbb{S},u) = \sum_{(v,\mathbb{T})\in E} f(v,\mathbb{T}) \tag{3.9}$$

The computer vision community frequently uses a special version of MRF; the $\mathbb{ST}$-graph, for minimum cut (or $\mathbb{ST}$-cut) for binary optimization problems using Ford-Fulkerson algorithm. In $\mathbb{ST}$ graph for binary problems, the source node represents one of the class label whilst the sink node represents the opposite class label. An example given in Figure 3.4 demonstrates implementation of Ford-Fulkerson algorithm on a $\mathbb{ST}$ graph. All edges from *source* to nodes and all edges from nodes to *sink* are called t-links, whilst edges between all other intermediate nodes are termed as n-links. In each iteration from Figure 3.4(a) to Figure 3.4(f), the algorithm finds the new path $\mathscr{P}_i$ from *source* ($\mathbb{S}$) to *sink* ($\mathbb{T}$) in the residual graph. The flow f sent along each path $\mathscr{P}_i$ is equal to the minimum of the available capacities of edges that form path $\mathscr{P}_i$. For instance, a path $\mathscr{P}_1$ found in Figure 3.4(a) from *source* to *sink* is via ($\mathbb{S}$, n_1, n_3, $\mathbb{T}$). The maximum flow f can be sent along $\mathscr{P}_1$ is 0.25. After sending flow along $\mathscr{P}_1$, the capacity of each edge forming path $\mathscr{P}_1$ is decreased by amount f as shown in Figure 3.4(b). Also, to keep the flow equilibrium in n-links, the capacity of each edge opposite to the direction of edge forming $\mathscr{P}_1$ is increased by amount f, as shown in case of n_1 and n_3, the capacity $c(n_3,n_1)$ is increased by 0.25. Since the total capacity of t-link $e(n_3, \mathbb{T})$ is utilised in path $\mathscr{P}_1$, no more flow can be sent through this link and hence the direction of edge $e(n_3, \mathbb{T})$ is changed. In each iteration, the f is increased by amount of flow of the new path. The algorithm

stops when there is no path left to send flow from $\mathbb{S}$ to $\mathbb{T}$. The final flow f is the maximum flow sent from $\mathbb{S}$ to $\mathbb{T}$ via 5 unique paths shown in Figure 3.4(a) to Figure 3.4(f), i.e. f=0.25+0.28+0.21+0.2+0.21=1.15. In the final residual graph Figure 3.4(f), any node, to which the *source* node can still send flow directly or via another node(s), is remain connected to *source* and disconnected from $\mathbb{T}$, i.e. the node is labelled $\mathbb{S}$. All other nodes, to which the *source* node cannot send flow in the final residual graph, are disconnected from *source* and remained connected to $\mathbb{T}$, i.e. the nodes are labelled $\mathbb{T}$. Thus, in Figure 3.4(f), the node n_1 and n_3 are assigned $\mathbb{S}$ label, and node n_2 is assigned with $\mathbb{T}$ label.

3.3.3.4 Max-Flow Min-Cut Theorem

The Max-Flow Min-Cut theorem states that in a flow network, the minimum capacity required to separate the network in such a way that no flow can pass from *source* to *sink* node is equal to the maximum amount of flow from source to sink. This implies that in the example provided in Figure 3.4, the maximum flow (i.e. 1.15) obtained through running Ford-Fulkerson algorithm is equal to the minimum cost required to sever the graph such that no flow can pass from source to sink, as shown in Figure 3.4(f). This theorem provided a strong basis for solutions developed for a wide range of MRF based energy minimization problems including image segmentation, classification and optical flow.

3.4 Conclusion

Under the domain of probability theory, graph based methods provide an effective framework for many computer vision problems. Probability and graph theory are well understood areas offering a range of algorithms based on the strong theoretical

concepts. The Bayesian base posterior probability, for estimating global optimal solution using graphical expressions is the comprehensive approach, utilised to achieve to milestones of this project. Since the underlying models for local configuration and classification are trained under probabilistic framework, the MRF graphical model is the highly appropriate for the current domain. Out of the two probabilistic graphical models (MRF and Bayesian Network), the MRF model is most suitable for the current problem as it allows cycles in the formulated graph, i.e. its bidirectional. During the experiments and evaluation, the applicability of Naïve Bayes' law, Markov Random Field, Ford-Fulkerson Algorithm, and $\mathbb{ST}$ graph cut for inference, is found highly subtle for major tasks of the current project.

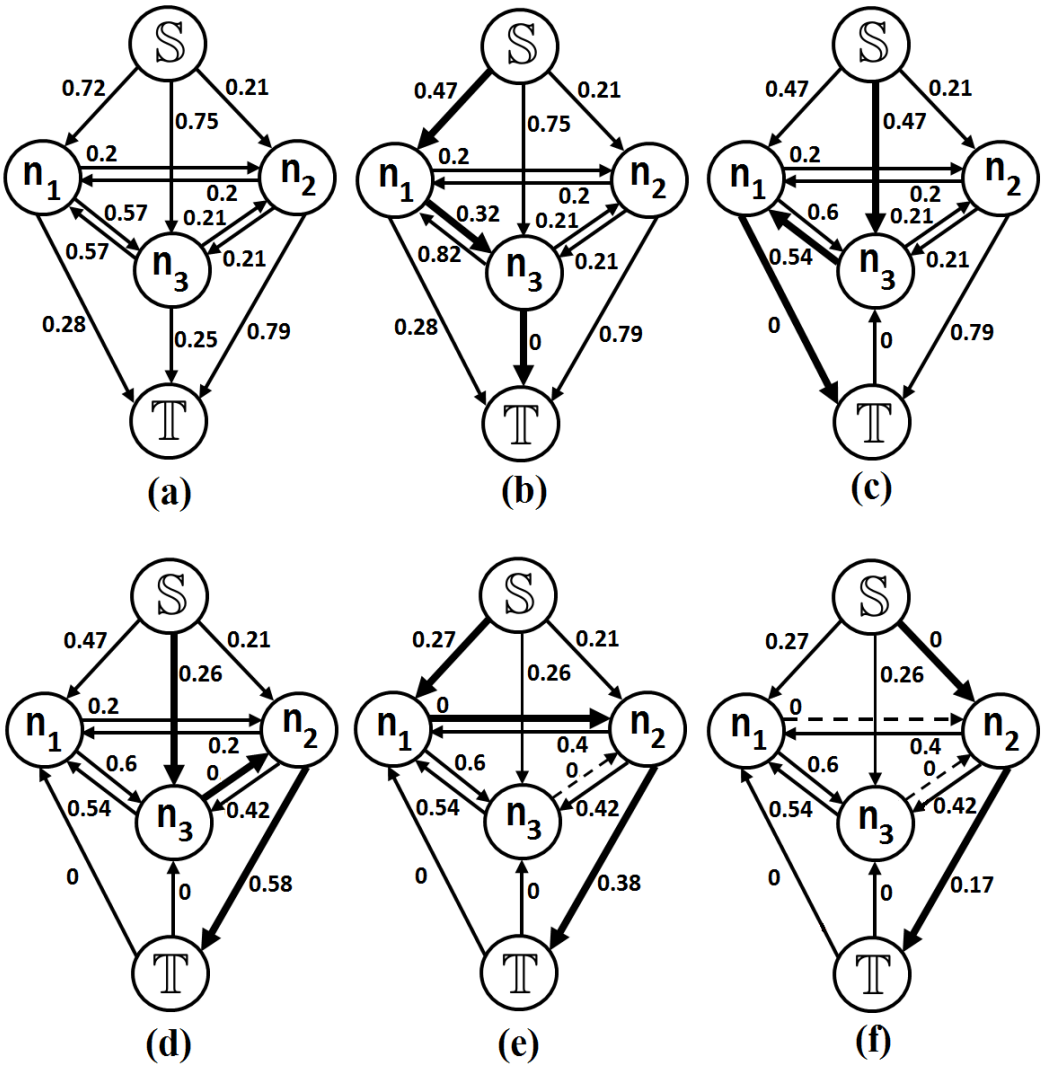

Fig. 3.4 The Ford-Fulkerson algorithm is applied on each graph. In each iteration from (a)-(f), the algorithm finds a new path from *source* to *sink* and send the flow along it. In each iteration, the algorithm updates the residual graph by decreasing the capacities of edges utilised in sending flow. The algorithm stops when there is no path left from *source* and *sink*.

Chapter 4

Vessels Local Configuration

4.1 Introduction

This chapter has three major contributions summarized in the following paragraphs.

First, a new probability based system is described (in Section 4.4) that is designed to efficiently form junctions. A junction is a set of segment ends in close proximity which may be interconnected; whereas segment interconnections are called joints including bridges (two segments joining), bifurcations (a parent segment joining two child segments), and terminals (single segment degenerate case). These junctions are formed by a novel dynamic region growing algorithm. This does not require hand-tuning of parameters, rather it is controlled by dynamically derived parameters for each region. The system ensures accurate assignment of segment ends to appropriate junctions and largely avoids forming large, false, or complex junctions.

Second, a supervised Bayesian probabilistic model is developed (in Section 4.5) for estimating the posterior probabilities of possible connection configurations of

segment ends within each junction. The geometrical and intensity features of retinal vessels at junctions follow certain principles which help to identify the true joints of broken segments. A detailed statistical analysis of these features, extracted from the landmark segment joints at junctions, is conducted using the training data. The representative parameters of frequency distributions of these features are identified and utilised for estimating priors and conditional likelihoods of configurations in the test data. The advantage of the Bayesian probability model is that it is trained to represent all mutually exclusive configurations at each junction.

Third, a new image set is established (in Section 4.2) consisting of standard binary vessel segmented images of DRIVE augmented with vessels classified as arteries and veins. The vessels are manually labelled in three phases by a trained ophthalmologist and two computer vision experts. This dataset is used to evaluate the proposed system. The dataset is freely available for study and research purpose.

Section 4.2 provides the details of methods introduced in (Al-Diri et al., 2009) and (Bankhead et al., 2012). These methods are used to obtain two sets of segmented vessels in DRIVE images and are used for training and testing. Section 4.3 formally states the research problem and the expected outcome of the thesis. This section also provides formal definitions of all the major components of retinal vascular system.

Parts of this chapter are published in (Qureshi et al., 2013) and (Qureshi et al., 2014).The overall pipeline overview of Implementation is shown in Figure 4.1.

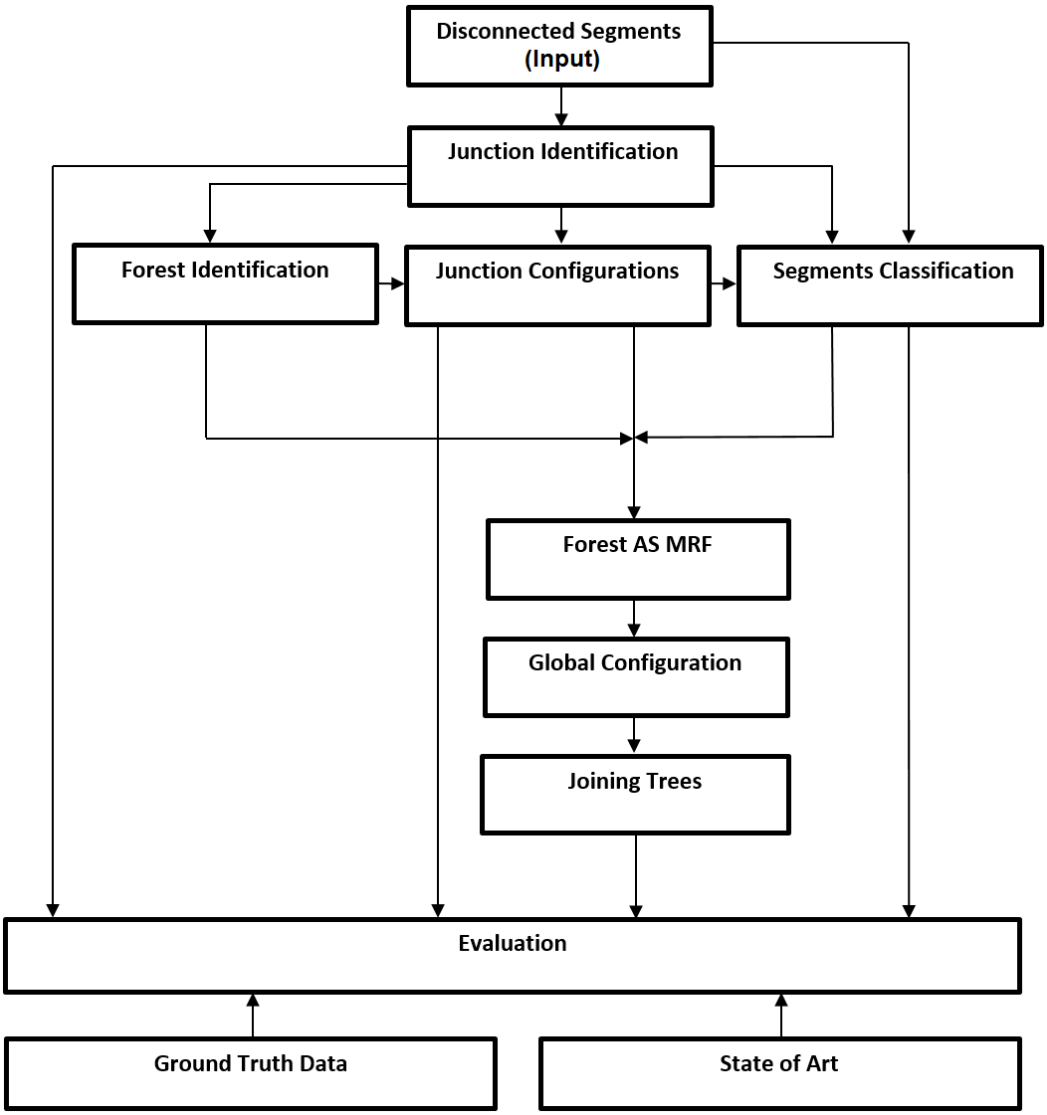

Fig. 4.1 Pipeline Overview for Implementation

4.2 Material

A number of retinal image sets are publically available for study and research purpose. These image sets are frequently used by researchers to comparatively assess algorithms for localization, segmentation, registration, classification, and identification of several retinal components in fundus images. The publically available datasets include STARE (Hoover, 1975), DRIVE, and diaretdb0/1 (Kauppi et al., 2006). The DRIVE dataset is also utilised in this thesis.

4.2.1 DRIVE Dataset

The DRIVE (Digital Retinal Images for Vessel Extraction) dataset is designed for the comparative study and analysis of retinal vessels. It is one of the most widely used dataset for vessel identification, vessel segmentation, and analysis of other retinal components, as used in (Jelinek et al., 2007), (Adjeroh et al., 2007), (Martinez-Perez et al., 2007), (Perfetti et al., 2007), and (Wang et al., 2007). The DRIVE contains 40 colour retinal images obtained through a screening program in the Netherlands from 400 diabetic subjects aged between 25-90 years, using a Canon CR5 non-mydriatic 3CCD camera with a 45 degree field of view (FOV). All images are of size 768 $\times$ 584 pixels with 8 bits per colour channel, and are divided into a training set and test set, each with 20 images, of the 40 images, 33 images do not show any sign of diabetic retinopathy, signs of mild early diabetic retinopathy including exudates, hemorrhages and pigment epithelium changes.

The dataset also contains three sets of binary images segmentations given manual of vessels (vessels identified as white pixels). These sets are Single Manual Set (20 images) for training set; First Manual Set (20 images) and Second Manual Set

(20 images) for test set. These sets were manually segmented by three observers (originally vision experts trained by ophthalmologists) from the DRIVE research group. For all the 40 images, there is also a set containing mask images that delineates the Field of view. A sample colour fundus image and its equivalent binary vessel segmented image from DRIVE is shown in Figure 4.2.

4.2.2 DRIVE Vessels-Classified Set

The research community lacks ground truth vessel labels (Artery/Vein) for the DRIVE dataset. This may lead to subjective errors when algorithms are evaluated using DRIVE images. In the following section (Section 4.2.2.1), a new gold standard image set with classified vessels as an extension of DRIVE dataset is presented, offering a highly reliable benchmark set for the future research.

4.2.2.1 Classified Vessels for DRIVE (CVD)

The Classified Vessels set for DRIVE images or CVD is established as an extension of the DRIVE images using the Single Manual Set (training set) and the First Manual Set (test set). The CVD set contains 40 images, resolution 565x584, consisting of manually segmented vessels with arteries marked red, veins blue, undistinguishable/orphan vessels as yellow, and distracting vessels (vessel-like data) marked with green colour. The green distributors might be true vessels in some cases; however their type is difficult to judge. A sample classified image is shown Figure 4.3.

4.2.2.2 Vessels Labeling Criteria

Following is a list of few characteristics of the retinal vasculature used as guidelines during the labeling process.

(a)

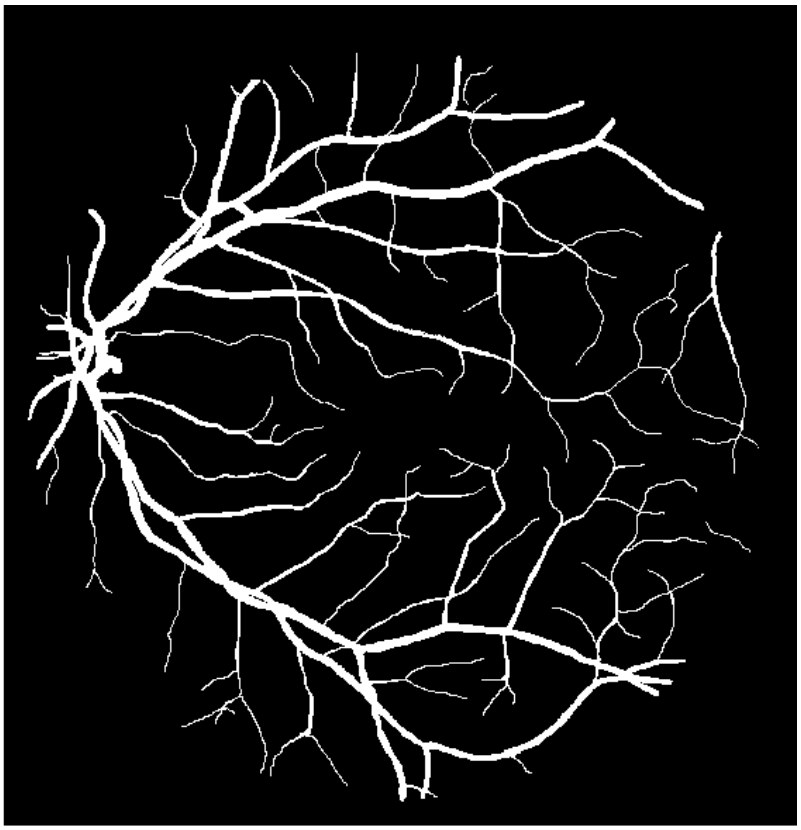

(b)

Fig. 4.2 (a): A healthy retinal image from DRIVE image set with (b): its manually segmented vessels in binary image.

(a)

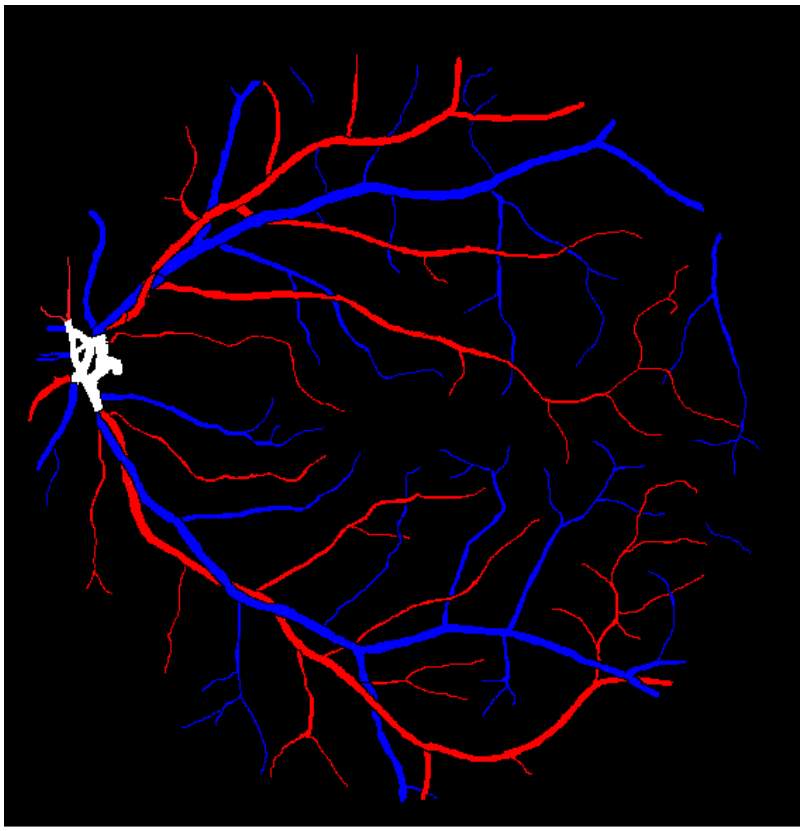

(b)

Fig. 4.3 (a): A sample colour retinal image from DRIVE image set and (b): its equivalent vessels-classified image from CVD image set.

1. Vessels crossing each other must belong to opposite classes. (Kondermann et al., 2007), (Larsen et al., 2005).

2. Arteries are usually thinner than veins in a close neighborhood (Liew et al., 2007) (Tramontan et al., 2008).

3. Parallel vessels in a close neighborhood usually belong to opposite classes.

4. The width of a parent vessel at a bifurcation is normally larger than that of its children vessels (Zamir, 1976), (Zamir and Chee, 1986), (Zamir and Brown, 1982) and (Zamir, 1978).

5. Arteries are brighter than veins in their neighborhood.

6. The central reflex is usually brighter/wider in arteries than veins (Narasimha-Iyer et al., 2008), (Brinchmann-Hansen and Heier, 1986), (Lowell et al., 2004b), and (Brinchmann-Hansen et al., 1986).

7. The vessels inside the optic nerve head are usually twisted and don't provide meaningful information, thus are not considered, unless exceptionally clear and prominent.

4.2.2.3 Vessel Labeling Process

Three observers labelled the vessels: two computer vision experts (including the author) at the School of Computer Science, University of Lincoln, UK, and one trained ophthalmologist at Sunderland Eye Infirmary, UK. The labeling is performed with a thorough analysis of enhanced colour images of DRIVE.

A three phase labeling process is conducted to perform labeling and to resolve labeling conflicts. In the first phase, all three observers independently labeled the

vessels. Around 85% of the vessels were consistently classified by all observers in first phase. The remaining of 15% vessels included a small percentage of unlabeled and distracting vessels.

In the second phase, the three observers shared their labeling with each other, and reconsidered their initial decisions. The observers were allowed to update their labeling upon change in opinion. This phase resolved 3% of vessels labeling.

In the third phase, the 12% of inconsistently labelled vessels were labelled by voting using the following criterion:

1. If any two observers ($O1$ and $O2$) label a vessel as x_i, whilst the third observer ($O3$) labels the same vessel as x_j, then the final label of that vessel is set as x_i.

2. If three observers ($O1$, $O2$, and $O3$) label a vessel differently from each other, i.e. x_i, x_j and x_k respectively, then vessel is marked Unlabeled.

3. An exceptional case of rule 2 is that if all three observers ($O1$, $O2$, and $O3$) have different label for vessel, however the ophthalmologist observer (say $O1$) is confident on his labeling x_i, then the vessel is set with x_i as its final label.

The three phase process resulted in 96% of vessels classified into arteries and veins, 3% of vessels as unlabeled, and 1% of vessels as distraction. In addition, the bifurcation and crossover locations in the labeled set are compared with the junction locations provided in (Azzopardi and Petkov, 2011) and have been found completely consistent. The dataset is publically available for evaluation purposes. The labeling opinion for unlabeled (shown in Figure 4.4) and distracting vessels (shown in Figure 4.5) from experts is welcome.

4.2.2.4 Labelling Complications

The unlabeled vessels (shown in Figure 4.4) refer mostly to those vessels emerging from the temporal (brighter side) of the optic nerve head, and/or thin vessels with insufficient features to be distinguished. During the labeling phases, two images were found with a few missing vessel segments in their corresponding binary segmented manual images (see Figure 4.6). In such cases, the labels of the nearby vessels are judged using spatial information, i.e. by observing the labels of neighboring vessels.

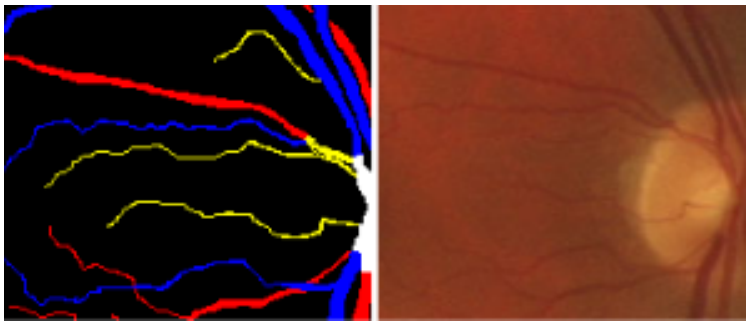

Fig. 4.4 Vessels with yellow colour showing undistinguishable vessel class.

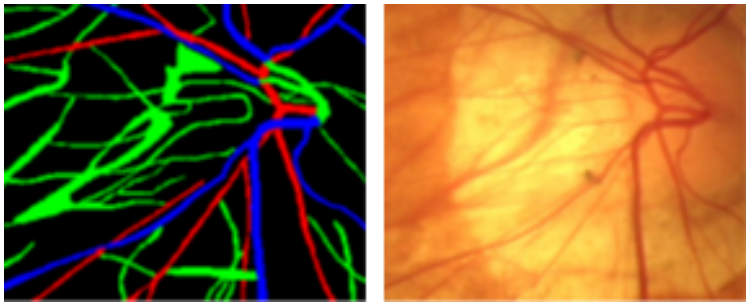

Fig. 4.5 The type of vessels (identified as green) is uncertain or these are not true vessels.

4.2.3 DSJS for Analysis and Experiments

Many robust techniques for automated segmentation of retinal vessels have been reported to date, (Hunter et al., 2005), (Marín et al., 2011), (Mendonca and Campilho,

Fig. 4.6 The arrow in the labeled image indicates a missing artery segment; while the corresponding binary equivalent (taken from Manual Set) doesn't provide any information about this missing segment.

2006), (Ricci and Perfetti, 2007), (Ricci and Perfetti, 2007), (Lupaşcu et al., 2010), (Odstrcilik et al., 2013), (Li et al., 2015), (Li et al., 2015), (Al-Diri et al., 2009) and (Roychowdhury et al., 2015). The proposed system presented in this thesis is capable to extract A/V trees from disconnected vessel segments obtained using any segmentation technique.

A probabilistic tracking method is proposed in (Roychowdhury et al., 2015) to detect blood vessels in retinal images. In this process, the vessel edge points are detected iteratively using local grey level statistics and vessel's continuity properties. At a given step, a statistical sampling scheme is adopted to select a number of vessel edge point's candidates in a local studying area. Local vessel's sectional intensity profiles are estimated by a Gaussian shaped curve. A Bayesian method with the Maximum a posteriori (MAP) probability criterion is then used to identify local vessel's structure and find out the edge points from these candidates. Different geometric shapes and noise levels are used for computer simulated images, whereas real retinal images from the REVIEW database are tested.

In (Zhang et al., 2015) an automatic unsupervised blood vessel segmentation method for retinal images is proposed. Firstly, a multidimensional feature vector is constructed with the green channel intensity and the vessel enhanced intensity

feature by the morphological operation. Secondly, self-organizing map (SOM) is exploited for pixel clustering, which is an unsupervised neural network. Finally, they classify each neuron in the output layer of SOM as retinal neuron or non-vessel neuron with Otsu's method, and get the final segmentation result.

An automated framework for segmenting retinal vasculatures is proposed in (Zhao et al., 2015). The proposed framework consists of three technical components: Retinex-based image inhomogeneity correction, local phase-based vessel enhancement and graph cut-based active contour segmentation. These procedures are applied in the following order. Underpinned by the Retinex theory, the inhomogeneity correction step aims to address challenges presented by the image intensity in-homogeneities, and the relatively low contrast of thin vessels compared to the background. The local phase enhancement technique is employed to enhance vessels for its superiority in preserving the vessel edges. The graph cut-based active contour method is used for its efficiency and effectiveness in segmenting the vessels from the enhanced images using the local phase filter. They have demonstrated its performance by applying it to four public retinal image datasets (3 datasets of colour fundus photography and 1 of fluorescein angiography).

For training and evaluation of the proposed automated system, two segmentation techniques ((Al-Diri et al., 2009) and (Bankhead et al., 2012)) are used to obtain the network of disconnected vessel segments in DRIVE images. These are termed the 'DRIVE Segment-Junction Set' $DSJS_1$ and $DSJS_2$ respectively. The technique in (Al-Diri et al., 2009) works by using two pairs of active contours to capture each side of the vessel edge, whilst in (Bankhead et al., 2012) vessels are segmented through an iterated procedure of wavelet thresholding. The segmented sets $DSJS_1$ and $DSJS_2$

differ from each other in many aspects, including the number of segmented vessels in each image, number of false segments, number and locations of disconnected points of segments network, and complexity of junctions. From the viewpoint of such aspects, the difference in $DSJS_1$ and $DSJS_2$ gives an opportunity for a fair evaluation of the proposed system.

In addition, the optic nerve head is a highly vessel-congested area in which vessel segments are usually twisted and/or broken; thus segments inside ONH are not considered during the analysis and experiments. To eliminate vessel segments from the ONH, the centre is manually located and vessel segments are removed from a region of size 100×100 pixels cantered at the ONH centre.

A sample of images selected from $DSJS_1$ and $DSJS_2$ is given in Figure 4.7.

As mentioned earlier that the DRIVE dataset comes with gold standard binary images with manual segmentation of vessels for all of its 40 colour images; the key reason for not utilizing the gold standard binary image set of manually segmented vessels for training and testing purpose, is because the measurements obtained from binary images are not as precise as extracted from colour images using some automatic segmentation technique. For instance, the pixel coordinates of vessel edges in the manually segmented binary images are expressed as whole numbers; whilst an elegant automatic vessel segmentation technique provides accurate vessel boundaries with fraction of pixels. Also, the centrelines obtained from manual segmentation using some thinning function are usually not as accurate, particularly at the junction location. In addition, the gold standard binary image set consists of vessel segmentation with no false or missing segments, making the problem of connectivity and classification of segments fairly simple. Thus evaluating AV

extraction technique using such dataset would keep the state of the art ambiguous as any automatic segmentation technique usually results in few false and/or missing segments. However, in this thesis, the gold standard binary set is used only for comparing the results obtained from automatic connectivity and classification of broken segments which were obtained using automatic segmentation technique.

4.3 Formal Problem Statement

This section formally describes the problem and expected outcomes, defining the terminology, and elements constituting the vascular system using set builder notation.

4.3.1 Preliminaries

- **Definition 1.** *Tree*: A retinal fundus image consists of a forest of single or multiple vascular trees T_j^l of arteries (A) and veins (V). In a completely segmented retinal vasculature, a tree T_j^l comprises of connected vessel segments of identical classes.

- **Definition 2.** *Segment*: In an incompletely segmented vasculature (such as $DSJS_1$ and $DSJS_2$), a segment s_a is an atomic section of (apparent) vessel with no bifurcations, crossings or breaks. It has two ends: the head h (which is nearest to optic disc) and tail t. The following rules are applicable:

  1. $\mathbf{S} = \{\{S_1\},\{S_2\},...,\{S_k\}\}$

  Whereas, S_j is the subset of superset **S**.

  2. $S_j = \left\{s_a^r | a = 1,2,3,... \wedge r \in \{h,t\}\right\}$

  3. $T_j^l = \{S_j | \forall s_a^r \in S_j, s_a^r = l\}$

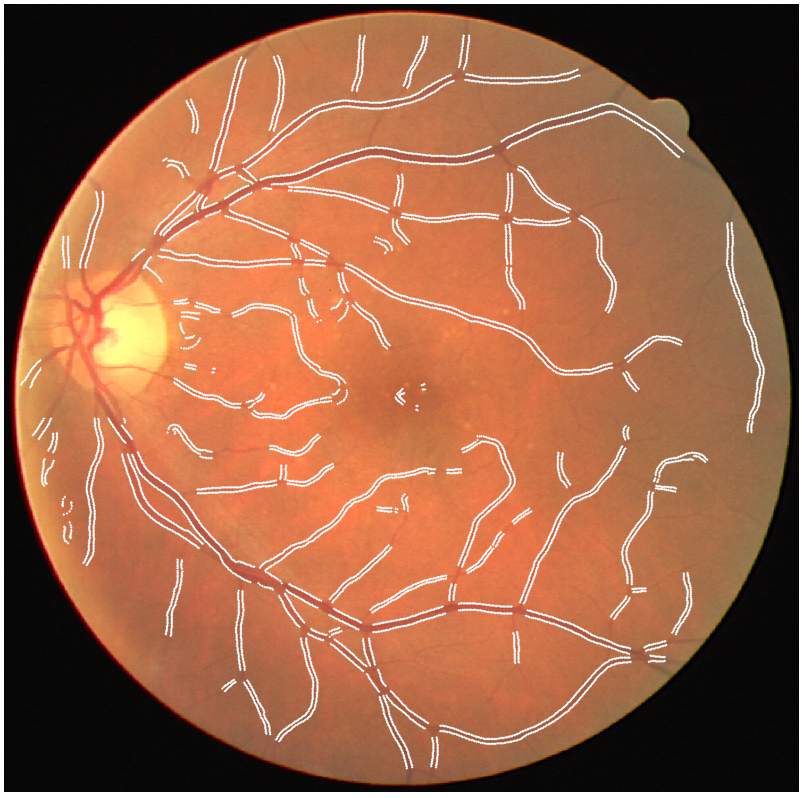

(a)

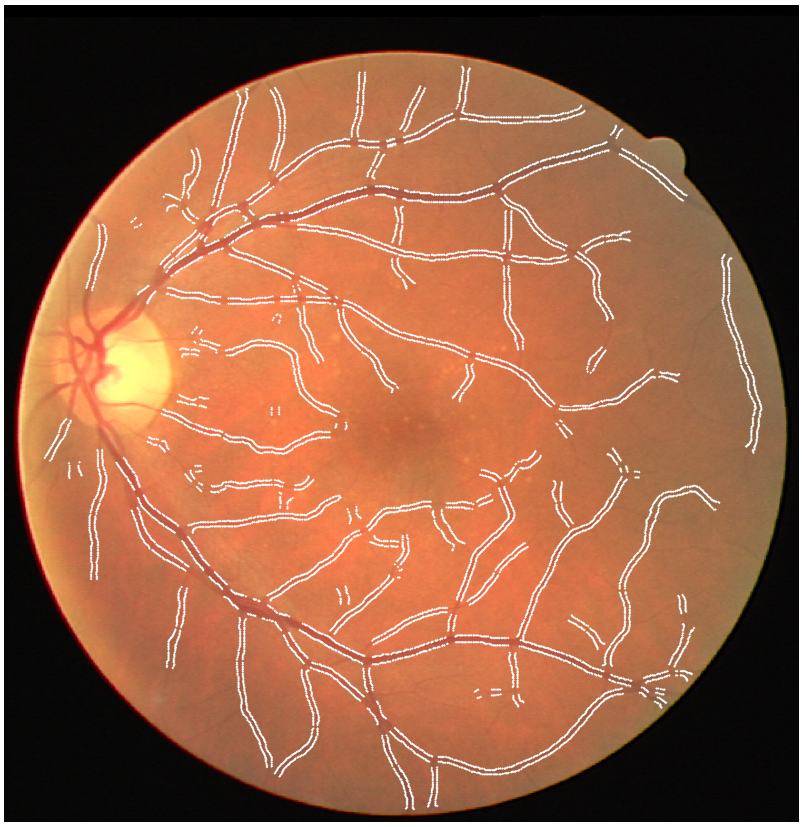

(b)

Fig. 4.7 Vessel segments obtained using technique Bankhead et al. (2012) in (a) and Al-Diri et al. (2009) in (b).

4. $\forall s_a^r \in T_j^l \Rightarrow s_a^r = l$

5. $\cup_p \{S_p\} = \mathbf{S}$ s.t. $S_a \cap S_b = \emptyset$.

A segment must have both of its ends belong to the same tree, i.e.

6. $\forall s_i \in T_j \Rightarrow \{s_a^h, s_a^t\} \in T_j$

A segment is the part of only one tree at a time , i.e.

7. $\forall s_a \in T_k, s_b \in T_q \Rightarrow a \neq b$

The superscript r with segment s_a is ignored whenever unnecessary.

- **Definition 3.** *Joint*: A joint L^u is a knot (a type of connection) of segment ends. There are three types of joints: a bridge is a joint of two segments ends with one head and one other tail (s_a^h, s_b^t), a bifurcation is a joint of three segment ends with one tail and the heads of other two segments (s_a^t, s_b^h, s_c^h), and a terminal is a segment tail end (s_a^t) that is not connected to anything. All segments forming any joint must belong to the identical vessel class.

8. $\forall (s_a, s_b) \in L^u \Leftrightarrow (s_a, s_b) \in l$

Segments forming any joint must be directly connected to each other.

9. $\forall (s_a, s_b) \in L^u \Leftrightarrow s_a \leftrightarrow s_b$, Symbol '$\leftrightarrow$' denotes connectivity.

From 8 and 9, we can deduce

10. $\forall (s_a \leftrightarrow s_b) \Leftrightarrow (s_a, s_b) \in l$

A segment s_a can't have both of its ends belong to same joint, i.e.

11. $\forall (s_a^r, s_b^{r'}) \in L^u \Rightarrow i \neq j$

- **Definition 4.** *Junction*: A junction j_k is a spatial location where a number of segment ends either meet or come into close proximity. Let **J** be a superset of sets J_i, whereas each J_i consists of junctions j_k, then the following rules are applicable:

  12. $\mathbf{J} = \big\{\{J_1\},\{J_2\},...\{J_m\}\big\}$

  13. $J_i = \{j_k | k = 1,2,3...\}$

  A junction cannot contain both the ends of a segment, i.e.

  14. $\forall a,b,s_a^h,s_b^t \in j_k \Rightarrow a \neq b$

  It must be noted that much of the literature uses 'junction' as a term for a 'bifurcation' joint only; here, a junction refers to a set of segment ends in a spatial location that connected by a number of joints.

- **Definition 5.** *Junction Configuration*: A junction configuration, C_q^k (the q^{th} configuration of the k^{th} junction is a combination of joints, such that every segment end in the junction is assigned to exactly one joint, $C_q^k = \{L_k^u | \bigcup_u s_a^r \in L_k^u = j_k\}$. The superscript u represents joint index.

- **Definition 6.** *Label Set*: The label set $\mathscr{L}$ is the set of vessel class labels which are assigned to vessel segments during the inference process, and is given as $\mathscr{L} = \{l_i | l_i \in (A,V)\}$.

- **Definition 7.** *Global Configuration*: A global configuration refers to a set of configurations at all junctions across the network. A local configuration, on

the other hand, refers to the one identified at specific junction independently from configurations at other junctions.

- **Definition 8.** *Disjoint Network*: Assuming the entire segment space **S** as a segment network **F**, a disjoint network F_i is a subset of **F** such that all segments that belong to F_i must be associated to each other directly via a single junction or indirectly via multiple junctions. The configuration of each disjoint network F_i may result in one or multiple vascular trees, thus:

  15. $\mathbf{F} = \big\{\{F_1\},\{F_2\},\{F_3\},..,\{F_k\}\big\}$

  16. $F_i = \big\{T_j^l | j = 1,2,3... \wedge l \in \{A,V\}\big\}$

  Also, a junction j_k can belong to only one disjoint network F_i at a time, i.e.

  17. $\forall s_a \in F_p, s_b \in F_q \Rightarrow \nexists j_k$ s.t. $(s_a, s_b) \in j_k$

  A fundus image with several vascular disjoint networks is given in Figure 4.8.

The segments form single joints or multiple overlapping joints at their associated junctions. This proves that any two segments (s_a, s_b) associated to a junction j_k don't necessarily connected to each other, i.e. they might belong to different overlapping joints. In addition, the cardinality of junction, denoted by $|j_k|$, is the total number of segment ends associated to j_k.The list of symbols used in this thesis with their descriptions are provided in Table 4.1.

4.3.2 Problem Statement

The configurations of different disjoint networks are independent of each other, thus the proposed method is applied on each disjoint network F_i separately. Formally, given a disjoint network F of set of unlabeled segment set S with their joints disconnected at respective junctions j_k of junction set J, the objective is to find a highest

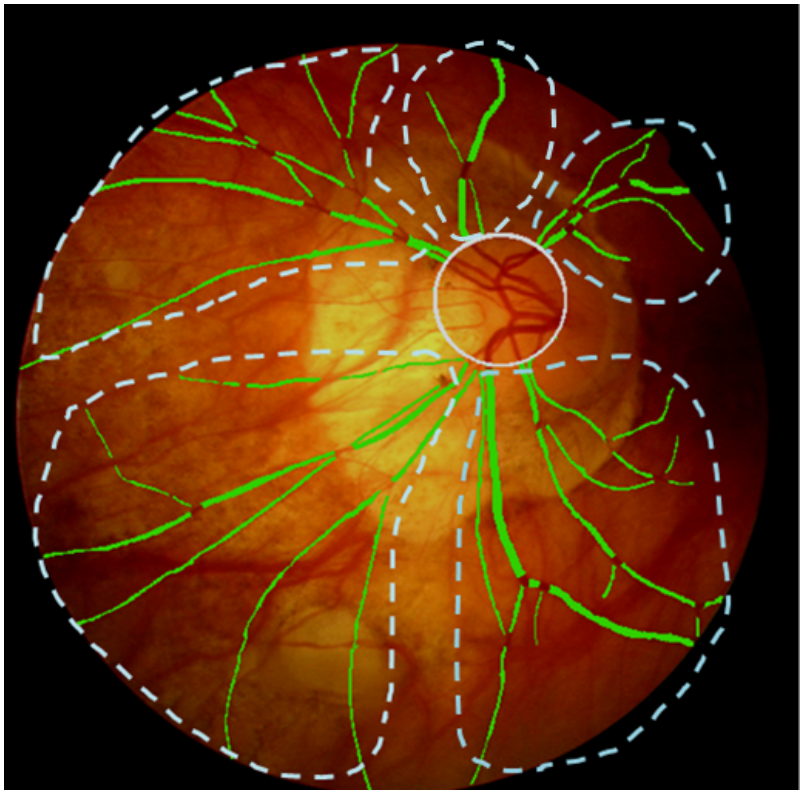

(a)

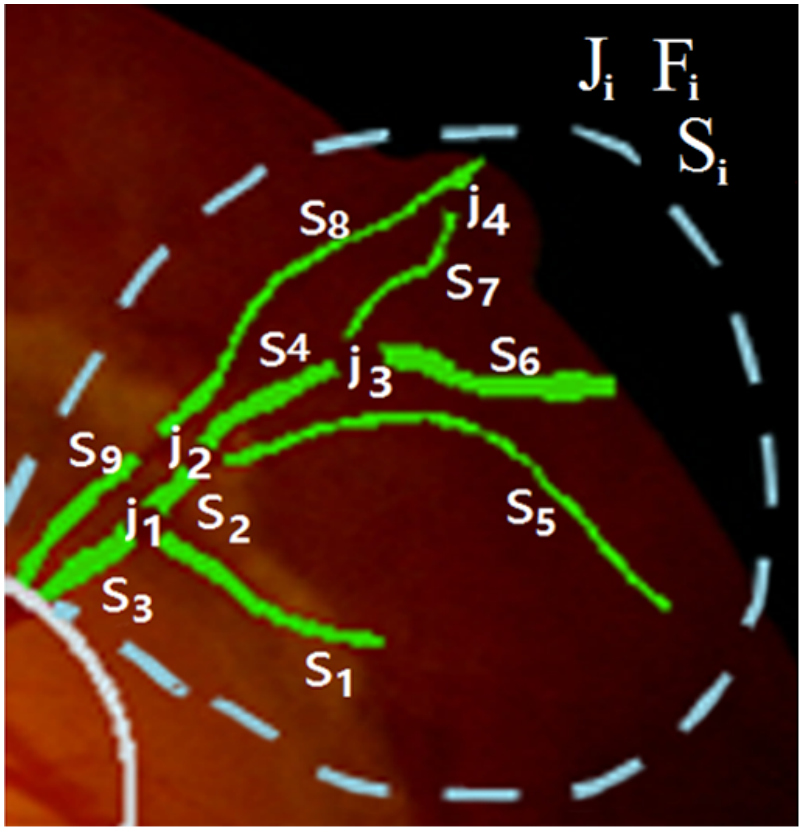

(b)

Fig. 4.8 (a) A retinal image from DRIVE with several disjoint networks. (b) A single disjoint network F_i consisting of nine segments and four junctions.

Symbols	Descriptions
A	Label of an arterial segment
V	Label of a venous segment
l	Class Label (representing either Artery or Vein)
s_i	i^{th} segment
s_i^r	Specific end of i^{th} segment, where r represents either head or tail end of segment
$\mathbf{S}$	Segment Space (Set of all segments)
S	Set of selected segments (Subset of $\mathbf{S}$)
T_j^l	j^{th} tree of vessels of class label l
$j_k, \mathbf{J}$	j_k : k^{th} junction; $\mathbf{J}$: Junction Space
J	Set of selected junctions (Subset of $\mathbf{J}$)
C_q^k	q^{th} configuration of segment ends at k^{th} junction
h, t	h : Head of the segment; t : Tail of the segment
L^u	u^{th} joint (such as Bifurcation, Bridge etc)
η, η_i	η : Hue (extracted from entire segment); η_i : Hue of i^{th} segment
ψ, ψ_i	ψ : Saturation (extracted from entire segment); ψ_i : saturation of i^{th}*segment*
v, v_i	v : Intensity (extracted from ending profiles of segment); v_i : intensity of i^{th} segment
w, w_i	w : Average segment Width; w_i : average width of i^{th}*segment*
r	Orientation (refers to segment head or tail)
m, m_i	m : Slope of centreline of segment at specific end; m_i : slope of centreline of i^{th} segment at its specific end
α	Angle between slopes of two segments at some junction
β	Width-Ratio of two segments
γ	Difference between intensities of two segments
δ_j	j^{th} intensity profile
ϕ ϕ^1 ϕ^k	Difference between orientations of two segments at a junction Orientation of a Terminal ($\phi^1 = r$) For Bridges (k=2), Bifurcations (k=3)
f	Feature Vector specific to the model
χ_a^r	Segment end region at r^{th} end of a^{th} segment
$\Omega_{a,b}$	Shared region between segment end regions of segment a and b, i.e. χ_a^r and χ_b^r
f_p	Front point (pixel) of the centreline of a segment at its specific end
b_p	Back point (pixel) of the centreline of a segment at its specific end
Υ_a^r	Length between points f_p and b_p
$\mathcal{V}$	Set of nodes in the formulated MRF graph
$\mathcal{E}$	Set of edges in the formulated MRF graph
$e(s_a, s_b)$	Edge between node s_a and s_b in formulated MRF graph
$\vec{\mathcal{G}}_{\mathbb{ST}}$	Formulated $\mathbb{ST}$ graph
$\mathbb{S}$	Source node in formulated graph
$\mathbb{T}$	Sink node in formulated graph
$\acute{F}$	Configured disjoint network
$\mathcal{G}'_{\mathbb{ST}}$	Residual graph after running Ford-Fulkerson algorithm
$\hat{s_a}$	Major Segment
$\bar{s_a}$	Minor Segment

Table 4.1 Symbols and Descriptions.

probability global configuration $\mathbf{C_i}$ of vessel segments at junctions by means of forming joints and classifying vessel segments of joints in order to extract AV Trees (T_i^l) such that extracted trees don't violate any of the aforementioned constraints (1-17).

This objective is achieved in a pipeline of four major phases given as

1. Forming junctions.
2. Estimating probabilities of local configurations.
3. Estimating class probabilities of segments.
4. Extraction of AV trees though global configuration.

The first two phases are explained in Section 4.4 and Section 4.5, whilst the remaining two phases are detailed in Chapter 5.

4.4 Junction Formation

Forming junctions is the first and the most critical task in the process of AV trees extraction. In this process, a number of geometrical locations are identified as junction points in the network of disconnected segments, with each junction point composed of (associated with) a small number of segment ends which may be interconnected. Accurate identification of these points is very important to ensure good performance at later stages. The literature does not offer any efficient technique that guarantees correct identification of junctions across segment network, and thus often resulting in non-true junctions such as wrong association of segment ends to the

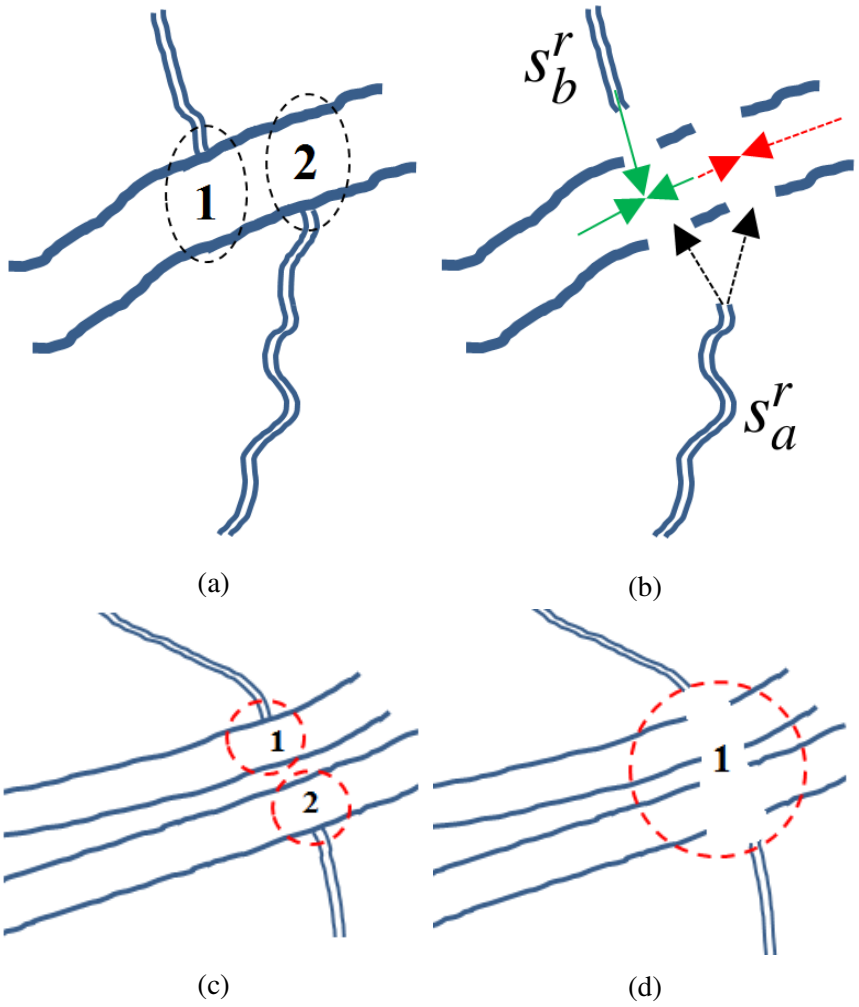

Fig. 4.9 (a): An illustration of two consecutive bifurcations at junction 1 and 2. (b): When disconnected, the segment s_a^r has equal chance to be associated to the junction 1 forming a wrong junction. (c): An illustration of two bifurcations at junctions 1 and 2 on very close vessels. (d): When disconnected, any system might form one big junction.

junction or identifying multiple close junctions as single junction. The illustration of these complexities is shown in Figure 4.9.

The geometrical features at the end profiles of a segment provide a good estimate of the direction of the missing part of the segment—this helps to approximate the location of the junction where the segment joins. Viewing a junction as a meeting point of endings of multiple segments, a junction is identified by considering the mutual associations of two or more segments having their ends in close proximity to each other. In this context, the conventional methods of identifying junction point, such as Tsai et al. (2004) and Al-Diri et al. (2010), work by growing the central line of a segment, in the direction obtained from ending profiles of segment, followed by detecting the intersection point with the direction vectors of other segments, see Figure 4.10. This approach works well with fairly simple cases, however, the accuracy in complex cases is not guaranteed.

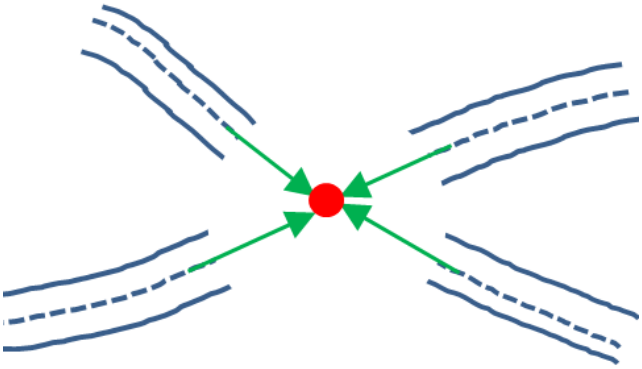

Fig. 4.10 The direction vectors of four segment ends find an intersection point, thus forming a junction of all four segment ends.

This thesis presents a probability based procedure to form junctions. The method works by specifying variable size regions at the ends of all segments in conjunction

to predefined conditions; followed by identifying junctions, each composed of all those segments that share their specified regions with each other to a reasonable extent. This procedure avoids forming abovementioned (non-true) types of junctions to a substantial extent. The complete procedure to form junctions is explained below.

4.4.1 Segment End Regions

A region is specified at each end of a segment, termed as 'segment end region' (*SER*) and is denoted by χ. The *SER* has four vertices—the coordinates of two of these vertices correspond to the two side points of the ending profile of the segment, whilst the other two are specified using a number of geometrical features at the ending profiles of a segment, see Figure 4.11.

At a particular end r of a segment s_a^r, let f_p and b_p denotes front and back points on the centreline at first and seventh profile respectively, whilst ps_1 and ps_2 denotes edge points of side 1 and side 2 of first profile of s_a^r. The coordinates of bp and fp are used to obtain the direction vector of s_a^r. The segment end region χ_a^r for segment s_a^r is defined as a region (set of image pixels), inside a convex polygon having four vertices, i.e. ps_1, ps_2, ps_3, and ps_4. The coordinates of ps_3 and ps_4 are specified using the length (denoted by Υ_a^r) between the point b_p and the point up to which the centreline is increased. A sample of segments with segment end regions is shown in Figure 4.11.

A shared-region $\Omega_{a,b}$ represents number of pixels shared by regions χ_a^r and χ_b^r of particular ends of two segments s_a^r and s_b^r, see Figure 4.12. The shared-region $\Omega_{a,b}$ provides an opportunity to the system to form a junction j_k that is composed of s_a^r

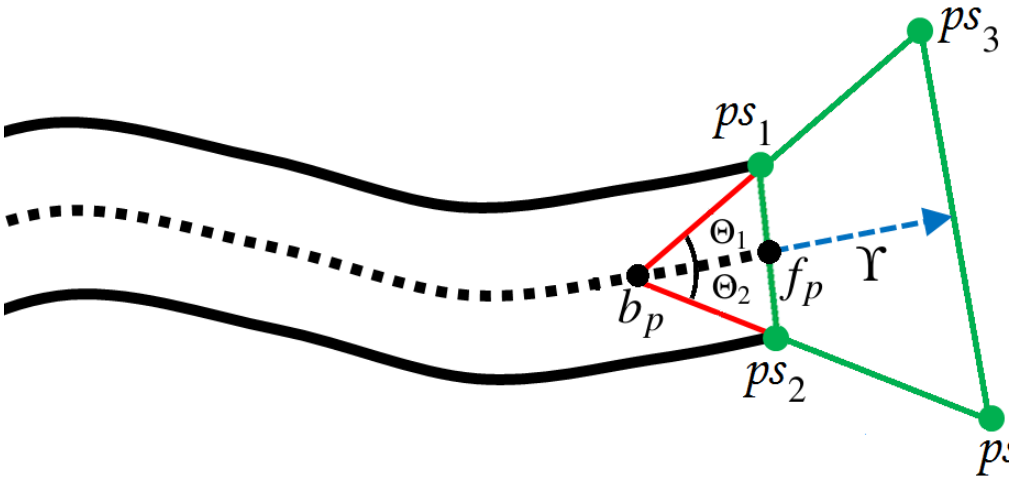

Fig. 4.11 An illustration of an *SER* at the end of a segment. The centreline at the end of the segment is increased as direction vector using b_p and f_p points. The green points are the four vertices of the polygon.

and s_b^r. In this context, a crucial step is to decide the value of Υ as it determines the size of χ for the segment end. A fixed size χ is not desirable: a large size produces inappropriate or excessive shared-regions, and the formation of excessively large or incorrect junctions. A small χ yields reduced numbers of shared-regions, and the failure to detect some true junctions. The approach adopted is to initially use a small size χ (using Υ_{MIN}) for all segment ends, followed by the size of χ for a subset of segment set that demonstrates either of the two conditions:

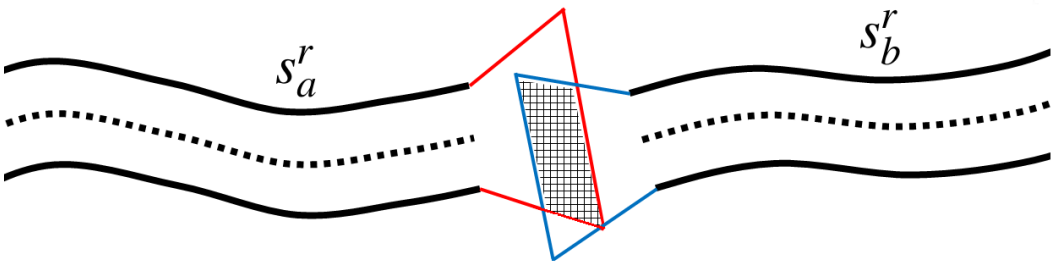

Fig. 4.12 An illustration of *SERs* of two segments with shared regions shown in shade.

Condition 1: When χ_a^r of a segment s_a^r doesn't have shared-region with χ_b^r of any other segment s_b^r, the length Υ_a^r is incrementally increased to update the size of χ_a^r, until χ_a^r becomes the part of any Ω, or Υ_a^r value reaches a maximum limit Υ_{MAX}. This step is demonstrated in Figure 4.13.

Condition 2: When χ_a^r of a segment s_a^r shares a region with both χ_b^r and $\chi_b^{'r}$ of segment s_b, the Υ_a^r is repeatedly decreased until χ_a^r shares region with χ_b^r only. This step is demonstrated in Figure 4.14.

During experiments, Υ_{MIN}=7 and Υ_{MAX} =10. The value of angles Θ_1 and Θ_2 is set 28.

In addition, the growing centreline (direction vector) at the segment end s_a^r may touch the boundary of another segment s_b. In this case, the segment s_b is split up into two segments at the points where the direction vector s_a^r collide with s_b. An pictorial description of this process is given in Figure 4.15.

4.4.2 Forming Junctions

In terms of *SERs*, a junction is defined as an association of segments that is determined by considering a shared region Ω between *SERs* of two or more of its associated segment ends. Any two segment ends associated with a junction must have shared-region between their *SERs*. Out of all segment ends forming a junction j_k, any two segment ends (s_a^r, s_b^r) must either have a shared-region $\Omega_{a,b}$ or associated via another segment end s_c^r of j_k, i.e. when there exists a relation as $\Omega_{a,c}$ and $\Omega_{b,c}$.

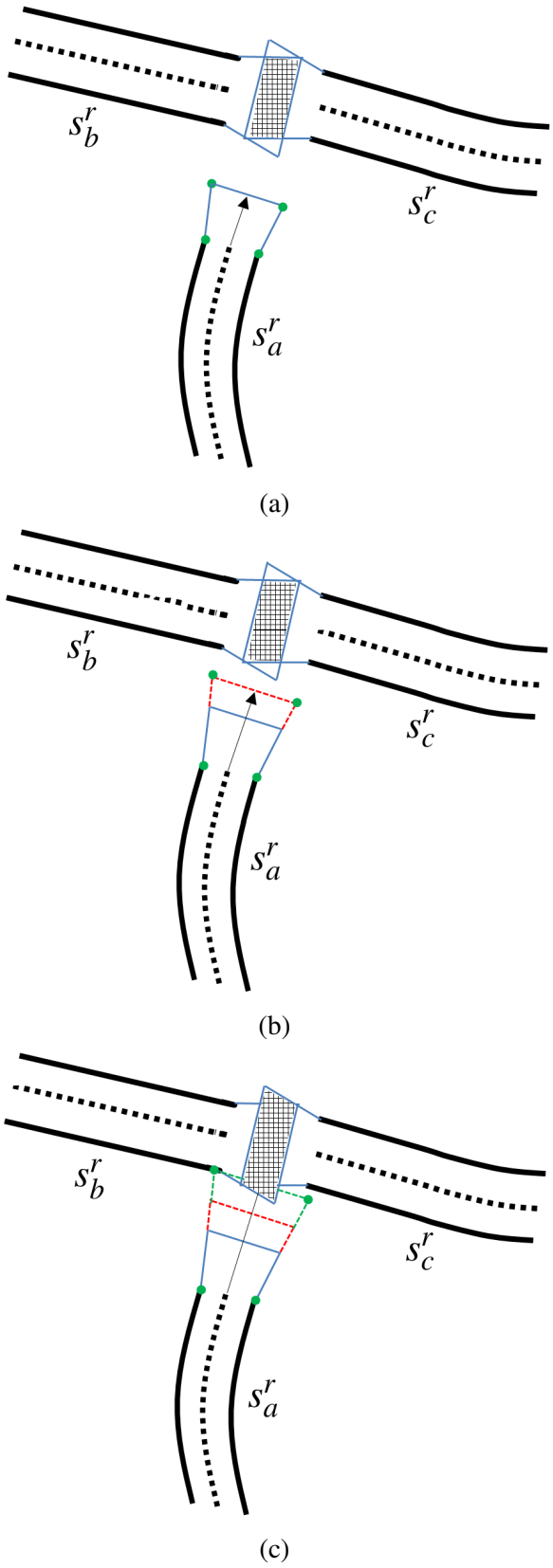

Fig. 4.13 (a)-(c): An Illustration demonstrating step by step increase in the size of *SER* of segment s_a^r until it found shared region with the *SER* of segment s_b^r or s_c^r.

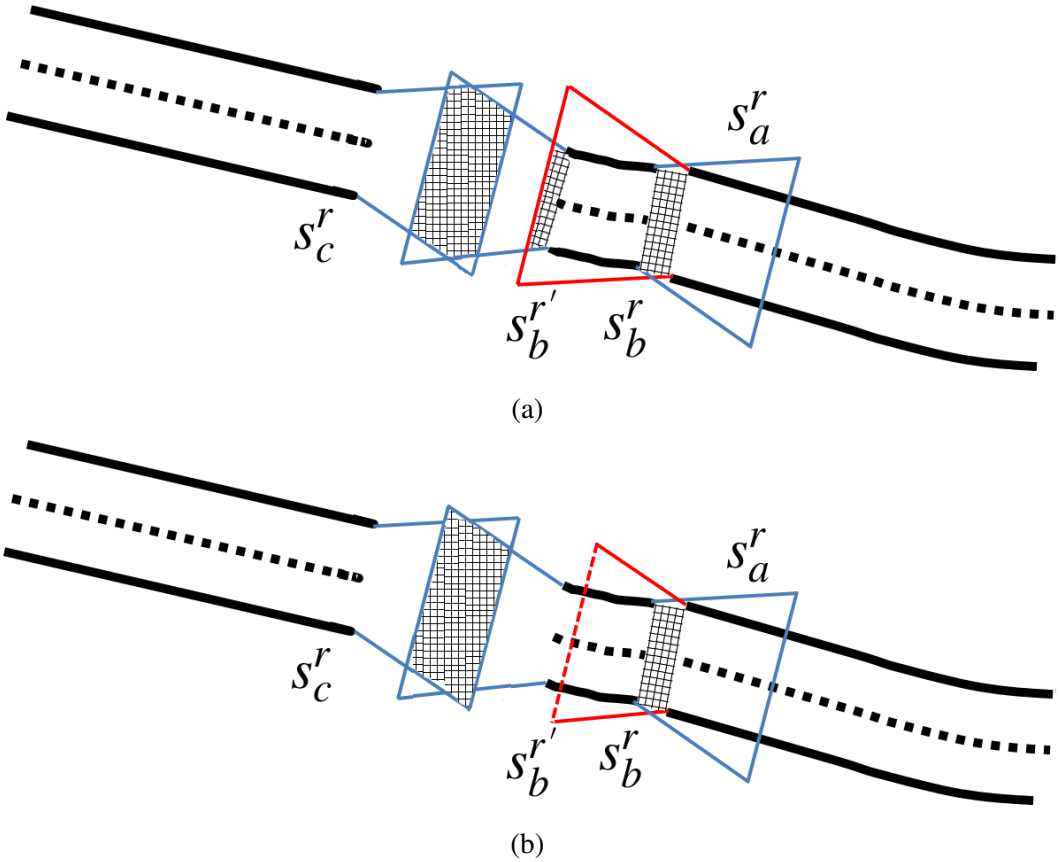

Fig. 4.14 (a) The system forms a single junction associating (s_a^r, s_b^r, $s_b^{r'}$, s_c^r) based on the implication of shaded regions. (b) The size of *SER* of s_a^r is recursively decreased until it shares region with only one *SER* of segment s_b which is closer to s_a^r, i.e. s_b^r.

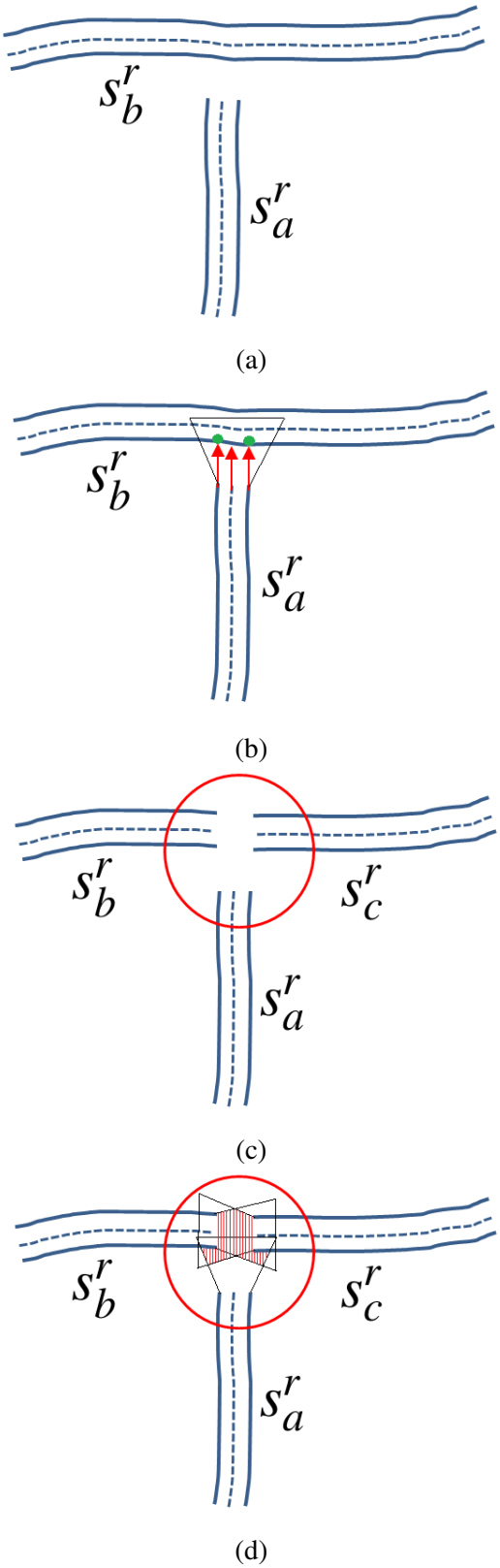

Fig. 4.15 (a) The segment s_a^r using its direction vector at the ending encounters the boundary of s_a^b; (b)-(c) the system splits s_a^b at the hit points; (d) and forms a junction with three segments s_a^r, s_b^r, and s_c^r.

Through a supervised training process, $\Omega_{a,b}$ for any two segment ends $s_a^r, and s_b^r$ associated to all true/false junctions were identified in training set of DSJS. The training process consists of interactively associating the endings of segments with their true connections as well as with false connections at the respective junctions. The following statistics are obtained during analysis:

- Mean of Ω obtained from all true junctions = μ_Ω=22 pixels.
- Standard deviation of Ω obtained from all true junctions = σ_Ω=7.5 pixels.
- Mean of Ω obtained from all false junctions = $\mu_\Omega^{'}$=5.2 pixels.
- Standard deviation of Ω obtained from all false junctions = $\sigma_\Omega^{'}$=3.3pixels.

The distributions of Ω in case of both true and false junctions is approximately normally distributed. Therefore, for any two segment ends s_a^r and s_b^r having shared-region $\Omega_{a,b}$, the probability that s_a^r and s_b^r belongs to an identical junction is given by:

$$p\big((s_a^r, s_b^r) \in j_k | \Omega_{a,b}\big) = \frac{p\big(\Omega_{a,b} | (s_a^r, s_b^r) \in j_k\big)}{p\big(\Omega_{a,b} | (s_a^r, s_b^r) \in j_k\big) + p\big(\Omega_{a,b}^{'} | (s_a^r, s_b^r) \in j_k\big)} \tag{4.1}$$

The posterior probabilities $p\big((s_a^r, s_b^r) \in j_k | \Omega_{a,b}\big)$ and $p\big((s_a^r, s_b^r) \in j_k | \Omega_{a,b}^{'}\big)$ were normalized to 1. For any two ends s_a^r, s_b^r having direct association, i.e. there exists $\Omega_{a,b}$, the value $p\big((s_a^r, s_b^r) \in j_k | \Omega_{a,b}\big)$ must be greater or equal to 0.5.

4.5 Probability Estimation for Local Configurations of Junctions

In Section 4.4, the system identifies independent junctions, composed of a small number of segment ends. To extract vascular trees from the segment network, the segment ends at each junction must be correctly connected with each other by means of joints including bifurcations, bridges, and terminals. A combination of joints accounting for all segment ends at a junction j_k is termed as 'configuration of the junction'. Depending on the number of segment ends in a junction, there are multiple possible configurations of each junction. In the following sections of this chapter (Section 4.5.1 to Section 4.5.5), a Bayesian probability based supervised procedure is introduced to estimate the posterior probabilities of all possible configurations at each junction.

4.5.1 Local Configuration Set

The configurations of a junction with a given number of segment ends fall into several configuration classes, based on the number and type of joints in the configuration. The configuration set is the set of all possible configurations (combinations) of segment ends in a particular junction. Each configuration may compose of one or multiple possible joints of segment ends depending on the number of segment ends associated to the junction.

Let junction j_k have N associated segment ends, then the configuration set $\mathbf{C}_k = \{C_k^q\}$ consists of all possible configurations C_q^k of joints, whereas subscript q denotes a unique configuration.

When N=2, $j_k = \{s_1^r, s_2^r\}$, there are two possible configurations $C_1^k = \big\{\{s_1^r\}, \{s_2^r\}\big\}$ and $C_2^k = \big\{\{s_1^r, s_2^r\}\big\}$. The configuration C_1^k consists of two terminals $\{s_1^r\}$ and $\{s_2^r\}$, whilst C_2^k composes of a bridge between s_1^r and s_2^r.

When number of associated segment N is three, i.e. $j_k = \{s_1^r, s_2^r, s_3^r\}$, then all possible configurations are given in Table 4.2. Out of seven total configurations in Table 4.2, note that three configurations C_5^k, C_6^k and C_7^k all represent a bifurcation joint with the same three segment ends. However, the identity of the parent segment end in a bifurcation is important, thus three different bifurcations are considered. For example, the bifurcation combinations $\{(s_1^r, \{s_2^r, s_3^r\})\}$ and $\{(s_2^r, \{s_1^r, s_3^r\})\}$ are not the same, whereas $\{(s_1^r, \{s_2^r, s_3^r\})\}$ and $\{(s_1^r, \{s_3^r, s_2^r\})\}$ are identical. In addition, the ordering of segments in case of a bridge is irrelevant, e.g. $\{s_1^r, s_2^r\}$ and $\{s_2^r, s_1^r\}$ are identical.

Similarly, when number of associated segments n is four, i.e. $j_k = \{s_1^r, s_2^r, s_3^r, s_4^r\}$, the 22 possible configurations are given as in Table 4.3. In addition, for any value of n, the total possible configurations at junction j_k can be enumerated using a similar procedure.

4.5.2 Bayesian Inference Modelling

A Naïve Bayesian inference model is developed to estimate the posterior probability for each configuration of a junction. The posterior probability $p(C_q^k|j_k)$ of q^{th} configuration C_q^k at junction j_k is estimated by Bayes theorem using the prior times the likelihood up to normalizing constant, and is given as:

Configuration Class	Configurations
Three Terminals	$C_1^k = \left\{\{s_1^r\},\{s_2^r\},\{s_3^r\}\right\}$
One Bridge + One Terminal	$C_2^k = \left\{\{s_1^r, s_2^r\},\{s_3^r\}\right\}$
One Bridge + One Terminal	$C_3^k = \left\{\{s_1^r, s_3^r\},\{s_2^r\}\right\}$
One Bridge + One Terminal	$C_4^k = \left\{\{s_2^r, s_3^r\},\{s_1^r\}\right\}$
One Bifurcation	$C_5^k = \left\{\{s_1^r, s_2^r, s_3^r\}\right\}$ $C_5^k = \left\{\{s_1^r, s_3^r, s_2^r\}\right\}$
One Bifurcation	$C_6^k = \left\{\{s_2^r, s_1^r, s_3^r\}\right\}$ $C_6^k = \left\{\{s_2^r, s_3^r, s_1^r\}\right\}$
One Bifurcation	$C_7^k = \left\{\{s_3^r, s_1^r, s_2^r\}\right\}$ $C_7^k = \left\{\{s_3^r, s_2^r, s_1^r\}\right\}$

Table 4.2 Possible Configurations drawn from three segments

$$p(C_q^k|j_k) \propto p(C_q^k)p(j_k|C_q^k) \tag{4.2}$$

The normalizing constant here is the sum of posterior probabilities of all possible configuration at junction j_k, i.e. $\sum_q p(C_q^k|j_k) = 1$.

The likelihood of the q^{th} configuration at junction j_k, i.e. $p(j_k|C_q^k)$, is the joint probability (statistical term 'Joint') of all the joints comprising the q^{th} configuration, thus Equation (4.2) can be rewritten as:

$$p(C_q^k|j_k) = p(C_q^k)\prod_u p(L_k^u|\mathbf{f}_k^u) \tag{4.3}$$

where $P(L_k^u|\mathbf{f}_k^u)$ is the posterior probability of the joint, given the observed features $\mathbf{f}_k^u = \{\bigcup \mathbf{f}_i^a | s_i^a \in L_k^u\}$, and u is the joint index.

Configuration Class	Configurations
Four Terminals	$C_1^k = \left\{\{s_1^r\},\{s_2^r\},\{s_3^r\},\{s_4^r\}\right\}$
One Bridge + Two Terminal	$C_2^k = \left\{\{s_1^r,s_2^r\},\{s_3^r\},\{s_4^r\}\right\}$
One Bridge + Two Terminal	$C_3^k = \left\{\{s_1^r,s_3^r\},\{s_2^r\},\{s_4^r\}\right\}$
One Bridge + Two Terminal	$C_4^k = \left\{\{s_1^r,s_4^r\},\{s_2^r\},\{s_3^r\}\right\}$
One Bridge + Two Terminal	$C_5^k = \left\{\{s_2^r,s_3^r\},\{s_1^r\},\{s_4^r\}\right\}$
One Bridge + Two Terminal	$C_6^k = \left\{\{s_2^r,s_4^r\},\{s_1^r\},\{s_3^r\}\right\}$
One Bridge + Two Terminal	$C_7^k = \left\{\{s_3^r,s_4^r\},\{s_1^r\},\{s_2^r\}\right\}$
Two Bridges	$C_8^k = \left\{\{s_1^r,s_2^r\},\{s_3^r,s_4^r\}\right\}$
Two Bridges	$C_9^k = \left\{\{s_1^r,s_3^r\},\{s_2^r,s_4^r\}\right\}$
Two Bridges	$C_{10}^k = \left\{\{s_2^r,s_3^r\},\{s_1^r,s_4^r\}\right\}$
One Bifurcation + One Terminal	$C_{11}^k = \left\{\{s_1^r,s_2^r,s_3^r\},\{s_4^r\}\right\}$ $C_{11}^k = \left\{\{s_1^r,s_3^r,s_2^r\},\{s_4^r\}\right\}$
One Bifurcation + One Terminal	$C_{12}^k = \left\{\{s_1^r,s_3^r,s_4^r\},\{s_2^r\}\right\}$ $C_{12}^k = \left\{\{s_1^r,s_4^r,s_3^r\},\{s_2^r\}\right\}$
One Bifurcation + One Terminal	$C_{13}^k = \left\{\{s_1^r,s_2^r,s_4^r\},\{s_3^r\}\right\}$ $C_{13}^k = \left\{\{s_1^r,s_4^r,s_2^r\},\{s_3^r\}\right\}$
One Bifurcation + One Terminal	$C_{14}^k = \left\{\{s_2^r,s_3^r,s_4^r\},\{s_1^r\}\right\}$ $C_{14}^k = \left\{\{s_2^r,s_4^r,s_3^r\},\{s_1^r\}\right\}$
One Bifurcation + One Terminal	$C_{15}^k = \left\{\{s_2^r,s_1^r,s_3^r\},\{s_4^r\}\right\}$ $C_{15}^k = \left\{\{s_2^r,s_3^r,s_1^r\},\{s_4^r\}\right\}$
One Bifurcation + One Terminal	$C_{16}^k = \left\{\{s_2^r,s_1^r,s_4^r\},\{s_3^r\}\right\}$ $C_{16}^k = \left\{\{s_2^r,s_4^r,s_1^r\},\{s_3^r\}\right\}$
One Bifurcation + One Terminal	$C_{17}^k = \left\{\{s_3^r,s_1^r,s_4^r\},\{s_2^r\}\right\}$ $C_{17}^k = \left\{\{s_3^r,s_4^r,s_1^r\},\{s_2^r\}\right\}$
One Bifurcation + One Terminal	$C_{18}^k = \left\{\{s_3^r,s_2^r,s_4^r\},\{s_1^r\}\right\}$ $C_{18}^k = \left\{\{s_3^r,s_4^r,s_2^r\},\{s_1^r\}\right\}$
One Bifurcation + One Terminal	$C_{19}^k = \left\{\{s_3^r,s_2^r,s_1^r\},\{s_4^r\}\right\}$ $C_{19}^k = \left\{\{s_3^r,s_1^r,s_2^r\},\{s_4^r\}\right\}$
One Bifurcation + One Terminal	$C_{20}^k = \left\{\{s_4^r,s_1^r,s_2^r\},\{s_3^r\}\right\}$ $C_{20}^k = \left\{\{s_4^r,s_2^r,s_1^r\},\{s_3^r\}\right\}$
One Bifurcation + One Terminal	$C_{21}^k = \left\{\{s_4^r,s_1^r,s_3^r\},\{s_2^r\}\right\}$ $C_{21}^k = \left\{\{s_4^r,s_3^r,s_3^r\},\{s_2^r\}\right\}$
One Bifurcation + One Terminal	$C_{22}^k = \left\{\{s_4^r,s_2^r,s_3^r\},\{s_1^r\}\right\}$ $C_{22}^k = \left\{\{s_4^r,s_3^r,s_2^r\},\{s_1^r\}\right\}$

Table 4.3 Possible Configurations drawn from four segments

In a second application of Bayes, the probability $p(L_k^u|\mathbf{f}_k^u)$ is calculated as

$$p(L_k^u|\mathbf{f}_k^u) = \frac{p(\mathbf{f}_k^u|L_k^u)p(L_k^u)}{p(\mathbf{f}_k^u|L_k^u)p(L_k^u) + p(\mathbf{f}_k^u|L_k^{u'})(p(L_k^{u'}))} \tag{4.4}$$

where $p(L_k^u)$ is the prior probability of the joint class, $p(\mathbf{f}_k^u|L_k^u)$ is the likelihood function for the observed features, given the (true) joint type, and $p(\mathbf{f}_k^u|L_k^{u'})$ is the likelihood function for the observed features given a "false joint" consisting of arbitrarily chosen segment ends within a junction that do not form a true joint.

Table 4.4 lists all the junction configuration classes with up to six segment ends, the frequencies within the training set, and the prior configuration probabilities, $P(C_q^k)$, estimated from these. Some theoretically possible larger configurations never occurred; thus these have been set to a minimal figure (0.001) to allow the system to respond if it does encounter such rare cases.

The likelihood function for a joint $p(\mathbf{f}_q^k|L_k^u)$, is modelled using the multivariate normal probability density function $\mathcal{N}(\mu_k^u, \Sigma_k^u)$, where μ_k^u and Σ_k^u are the centroid vector and covariance matrix of the joint feature vector for that class of joints; $p(\mathbf{f}_k^u|L_k^{u'})$ is similarly modelled. The prior probabilities of the joint classes, $p(L_k^u)$, estimated from the frequency distribution in the training set, are given in Table 4.5.

4.5.3 Feature Selection and Extraction

To estimate the probability of joints at junctions, a small number of features are extracted at the associated segment ends. These features bear rich information about joints. For example, terminals are typically small (low width); bridged segments have roughly equal widths, intensity profiles and directions; bifurcations have a

$\|j\|$	Configuration	Total	Frequency	$P(C_q)$
1	1T	2124	2034	0.951
2	2T		45	0.451
	1B	98	53	0.540
3	3T		15	0.011
	1B, 1T		18	0.013
	1Y	1370	1337	0.975
4	4T		5	0.007
	2B		632	0.888
	1B, 2T		19	0.026
	1Y, 1T	711	55	0.077
5	5T		0	0.001
	2B, 1T		2	0.039
	1B, 3T		0	0.001
	1Y, 1B		47	0.921
	1Y, 2T	51	2	0.039
6	6T		0	0.001
	3B		0	0.001
	2B, 2T		1	0.100
	1B, 4T		0	0.001
	2Y		7	0.700
	1Y, 3T		0	0.001
	1Y, 1B, 1T	10	2	0.200

Table 4.4 Prior probabilities estimates of all possible junction configurations. T = terminal, B = bridge, Y = bifurcation.

Number of segments at all junctions	4056
Number of terminals	2034
Prior Probability for terminals	0.501
Prior Probability for non-terminals	0.498
Groups of two segments in all junctions	2038
Number of bridges	670
Prior Probability for bridges	0.328
Prior Probability for non-bridges	0.672
Groups of three segments in all junctions	2081
Number of bifurcations	1381
Prior Probability for bifurcations	0.663
Prior Probability for non-bifurcations	0.336

Table 4.5 Frequency distributions and Prior probability estimates of joint classes.

consistent relationship between widths and angles. The features are extracted from an area along 7 centreline-profiles at the segment end; see Figure 4.16. The basic segment end features are discussed below.

4.5.3.1 Basic Features

- **Vessel Direction** The direction vector m represents the direction of the straight line between the first and last centreline points in the segment end f_p and b_p, towards the junction the segment end is associated with: see Figure 4.16. The procedure is fairly simple and it consists of measuring the vessels direction vector (m) by specifying the seed points along the vessel segment. Specifying seed-points is however slightly tricky, as it can drastically change the output. In this analysis, we measure the direction vector of a vessel at a particular end by taking front (f_p) and back (b_p) pixels (7 centreline pixels along segment) as the seed points.

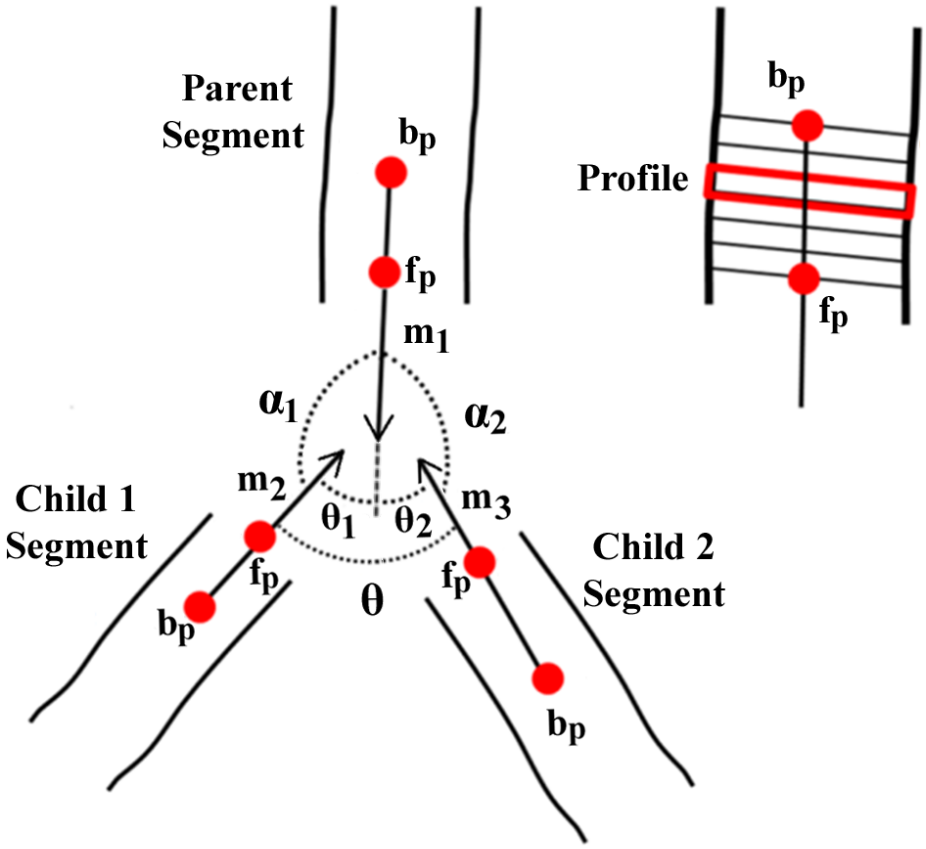

Fig. 4.16 End of vessel segment with front point f_p and back point b_p on seven profiles.

It is important to mention here, that when considering the number of segment ending profiles, the parameter 7 is found a reasonable number based on empirical observations. This value is sensitive when estimating the ending direction of a segment. It is observed in some cases that by using less or above than 7 ending profiles gave wrong direction of segment end. This is because sometimes a segment is locally tortuous, and thus by increasing or decreasing the number of ending profiles, there is a significant change in the direction of the segment.

- **Vessel Width** The Ribbon of Twins active contour model (Al-Diri et al., 2009) is used to extract the vessel width at the seven centreline pixels of the segment end. The final width w is the mean of widths calculated at each centreline pixel of seven profiles at segment's end.

- **Vessel Intensity** The vessel intensity v is described as the grey level distribution of intensity at each centreline profile of segment end. The grey level distribution of intensity at each profile is measured by considering the edge points of segment's profile followed by taking the linear interpolation of a 2-D grid. Let a segment end has edge points up to seven profile as $\big\{(x_{11},y_{11},x_{21},y_{21}),(x_{12},y_{12},x_{22},y_{22}),$ $(x_{13},y_{13},x_{23},y_{23}),(x_{14},y_{14},x_{24},y_{24}),(x_{15},y_{15},x_{25},y_{25}),(x_{16},y_{16},x_{26},y_{26}),$ $(x_{17},y_{17},x_{27},y_{27})\big\}$. The first subscript index with x and y represent the sides of segment (i.e. 1 for side1 and 2 for side2) whilst the second superscript index denotes the profile index (1-7).

  Let μ_{δ_j} and σ_{δ_j} represents the mean and standard deviation of intensity of j^{th} profile of segment s_a obtained using two edge points of the profile, then μ_v

and σ_v represents mean and standard deviation of intensity of the segment end respectively, and given as:

$$\mu_v = \frac{\sum_{j=1}^{7} \mu_{\delta_j}}{7} \tag{4.5}$$

$$\sigma_v = \frac{\sum_{j=1}^{7} \sigma_{\delta_j}}{7} \tag{4.6}$$

- **Vessel Orientation** The Orientation refers to the relative position of the particular end of a segment to the centre of the optic nerve head. All retinal vessels originate at the optic nerve head and bifurcate several times to spread out over the retina. A segment between any two consecutive bifurcations can be considered as a parent segment or a child segment depending on the bifurcating point one references to. The end of a segment originated as a result of a bifurcation, is closer to the ONH than the other end of the same segment where it bifurcates itself. This property provides a good indication for a true orientation of segment's origin.

  The orientation of a segment is measured by calculating the Euclidean distance from the centre of ONH to the front pixel f_p of each segment end.

4.5.3.2 Derived Features

The derived features are calculated from the basic feature obtained from two of more segment ends; there include the width ratio β, angle α, intensity difference γ, and orientation parity ϕ^2.

Let s_1^r and s_2^r be two segment ends with basic features $\{w_1, \mu_{v_1}, \sigma_{v_1}, m_1, r_1\}$ and $\{w_2, \mu_{v_2}, \sigma_{v_2}, m_2, r_2\}$ respectively, then the deflection angle α and width ratio β are defined as:

$$\alpha = \cos^{-1}\left(\frac{m_1.m_2}{|m_1|.|m_2|}\right) \tag{4.7}$$

$$\beta = \frac{\min(w_1, w_2)}{\max(w_1, w_2)} \tag{4.8}$$

Since the intensity distribution is represented by its mean and standard deviation, the difference between the distributions of two segment ends can be characterized using Bhattacharya distance between distributions as:

$$\gamma = \frac{1}{4}\ln\left(\frac{1}{4}\left(\frac{\sigma_{v_1}^2}{\sigma_{v_2}^2} + \frac{\sigma_{v_2}^2}{\sigma_{v_1}^2} + 2\right)\right) + \frac{1}{4}\left(\frac{(\mu_{v_1} - \mu_{v_2})^2}{\sigma_{v_1}^2 + \sigma_{v_2}^2}\right) \tag{4.9}$$

Similarly, the parity between the end types in a pair, ϕ^2, is defined as $\phi^2 = r_1 \oplus r_2$, where $\oplus$ denotes the exclusive-OR operator.

The extracted features are then normalized to the range $[0, 1]$, using:

$$f_i^n = \frac{f_i - f_{min}}{f_{max} - f_{min}} \tag{4.10}$$

4.5.4 Parameter Estimation through Supervised Learning

The likelihood function $p(\mathbf{f}_k^u | L_k^u)$ in Equation 4.4 is the probability density function which is the estimate of the likelihood of a particular joint L_k^u given a set of features $\mathbf{f}_k^u$. The densities are estimated through a supervised training process by identifying frequency distributions of features of true joints including terminals, bridges, and

bifurcations. The following sections (4.5.4.1, 4.5.4.3, 4.5.4.2) provide details of procedure for identifying representative parameters of frequency distributions of distinct feature sets for three joint classes.

4.5.4.1 Terminals

During the training process, around 1923 true terminals were identified in the training set of DRIVE. The training process consists of interactively identifying the terminal segments in training sets of both $DSJS_1$ and $DSJS_2$ image sets. The basic features extracted from true terminals includes width (w), intensity (v) and orientation (r). The direction feature (m) for a terminal doesn't represent or affect its characteristics, and therefore is not included in the feature set $f_{ter} = \{w, v, r\}$. The frequency distribution of the each feature of f_{ter} is tested against normality using shapiro wilk test and are found normally distributed with following parameters: $\mu_w = 0.09, \mu_v = 0.48, \sigma_w = 0.04$ and $\sigma_v = 0.12$.

The orientation r is a discrete variable and is examined at 1923 true terminals, out of which 1422 terminals are found tail (t). The probability mass function based on Bernoulli distribution is established for orientation feature. Let $\mathscr{G}_{ter}$ be the probability mass function of the distribution a, then:

$$\mathscr{G}_{ter} = \begin{cases} 0.73 & r = t \\ 0.27 & r = h \end{cases} \tag{4.11}$$

where $0.73 = 1422/1923$, there being 1422 tail segment ends among 1923 terminals. The likelihood can then be estimated using the generalized probability density function as:

$$P(\mathbf{f}|L) = \mathscr{N}(\mu_w, \sigma_w)\mathscr{N}(\mu_v, \sigma_v)\mathscr{G}_{ter}. \tag{4.12}$$

4.5.4.2 Bridges

During the training process, 564 true bridges were identified in DRIVE training image set. Through interactive system, the true bridges were identified while using the Gold standard binary image set for reference. The basic features extracted from segment ends forming true bridges includes $\{w, v, a, m\}$, using which derived features $\{\alpha, \beta, \gamma, \phi^2\}$ were calculated. The parameters of their frequency distributions are identified as: $\mu_\alpha = 0.49, \sigma_\alpha = 0.056, \mu_\beta = 0.85, \sigma_\beta = 0.11, \mu_\gamma = 0.27, \sigma_\gamma = 0.15$. The end class parity has value 1 (tail meets head) in 531=564 = 0.94 of the true bridges (the remaining 6% of cases occurring rarely where segments curve back towards the ONH), and defines the probability mass function $\mathscr{G}_{bri}$. Thus, the likelihood for a bridge can be calculated by:

$$P(\mathbf{f}|L) = \mathscr{N}(\mu_\alpha, \sigma_\alpha)\mathscr{N}(\mu_\beta, \sigma_\beta)\mathscr{N}(\mu_\gamma, \sigma_\gamma)\mathscr{G}_{bri}. \tag{4.13}$$

4.5.4.3 Bifurcations

The bifurcations were examined by performing a pairwise analysis of the width, intensity and direction disparities between the parent segment end and each of the child segments' ends in turn. In addition to derived features, two more features θ and ϕ^3 are estimated at bifurcations. The angle θ is the angle between the two children, and an end class feature ϕ^3 which is defined as 1 when the parent is a tail and both children are heads, 0 otherwise.

Let $f_{y,z}$ represents feature taken between segments y and z, where parent segment is represented as 1, whilst the two children as 2 and 3. The feature vector is given as $\mathbf{f} = (\alpha_{1,2}, \alpha_{1,3}, \theta_{2,3}, \beta_{1,2}, \beta_{1,3}, \beta_{2,3}, \gamma_{1,2}, \gamma_{1,3}, \gamma_{2,3}, \phi^3)$. An illustration of a typical bifurcation with its features is shown in Figure 4.16. The features were extracted at 1381 true bifurcations with the distribution parameters provided in Table 4.6. The feature ϕ^3 = 0.76 = 1050/1381, given that 1050 of the 1381 training bifurcations had the typical end orientation combination. The likelihood of a bifurcation is then calculated using the product of the estimated normal distribution functions for the continuous parameters and the Bernoulli mass function $\mathscr{G}_{bif}$ for the orientation as:

$$P(\mathbf{f}|L) = \mathscr{N}(\mu_{\alpha_1}, \sigma_{\alpha_1})\mathscr{N}(\mu_{\alpha_2}, \sigma_{\alpha_2})\mathscr{N}(\mu_{\theta}, \sigma_{\theta})\mathscr{N}(\mu_{\beta_1}, \sigma_{\beta_1})\mathscr{N}(\mu_{\beta_2}, \sigma_{\beta_2})\mathscr{N}(\mu_{\beta_3}, \sigma_{\beta_3})$$
$$\mathscr{N}(\mu_{\gamma_1}, \sigma_{\gamma_1})\mathscr{N}(\mu_{\gamma_2}, \sigma_{\gamma_2})\mathscr{N}(\mu_{\gamma_3}, \sigma_{\gamma_3})\mathscr{G}_{bif}. \tag{4.14}$$

The parameters for the false joint distributions were estimated using the same training set. All non-terminal segment ends from the training set were taken as false terminals. A false bridge set was constructed by matching each bridge segment end in a crossing junction with its non-partners. A false bifurcation set is constructed by taking the true bifurcations and swapping the parent segment end with a child segment end.

4.5.5 Overlap Removal

An overlap (or overlapping segment) is one where two vessels from opposite classes run parallel and overlap for short distance, and are segmented as a single segment. The geometrical structure of an overlap greatly resembles to two bifurcations—one

	angle	β	γ
s_1, s_2	$\mu_{\alpha_1} = 0.36$ $\sigma_{\alpha_1} = 0.07$	$\mu_{\beta_1} = 0.71$ $\sigma_{\beta_1} = 0.32$	$\mu_{\gamma_1} = 0.31$ $\sigma_{\gamma_1} = 0.25$
s_1, s_3	$\mu_{\alpha_2} = 0.41$ $\sigma_{\alpha_2} = 0.08$	$\mu_{\beta_2} = 0.68$ $\sigma_{\beta_2} = 0.27$	$\mu_{\gamma_2} = 0.32$ $\sigma_{\gamma_2} = 0.31$
s_2, s_3	$\mu_{\theta} = 0.23$ $\sigma_{\theta} = 0.10$	$\mu_{\beta_3} = 0.72$ $\sigma_{\beta_3} = 0.24$	$\mu_{\gamma_3} = 0.27$ $\sigma_{\gamma_3} = 0.36$

Table 4.6 Parameters of distributions of bifurcation features.

at each end of the overlapping segment which appears like the parent segment at both junctions due to its exaggerated width. This leads to a high probability of falsely identifying bifurcations at overlap ends. To resolve this, the system detects an overlap whenever both ends of a segment are identified as parents of bifurcations. The system then merges the two junctions at the ends of the overlapping segment, discarding that segment; when the configuration is resolved it should select two bridges, as shown in Figure 4.17.

Often, overlapping segments appear in consecutively. For instance, a true single overlap might be disconnected resulting in multiple overlapping segments appear one after another, as shown in Figure 4.18. In such a case, resolving overlaps requires considering the configurations of multiple junctions at the same time. This requires a global configuration step which will be discussed in the next chapter.

4.6 Conclusion

Discontinuity of the segmented retinal vasculature is an unavoidable obstacle for those interested in studying the geometrical properties of vascular trees. Under the

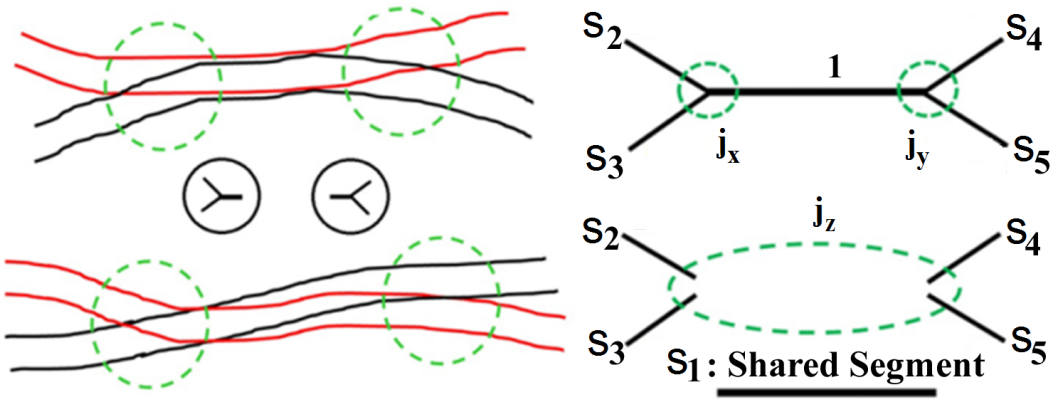

Fig. 4.17 Overlapping segments are falsely segmented as a single, wide 'overlap segment'. This is detected an eliminated, and the system detects the resulting pair of bridges.

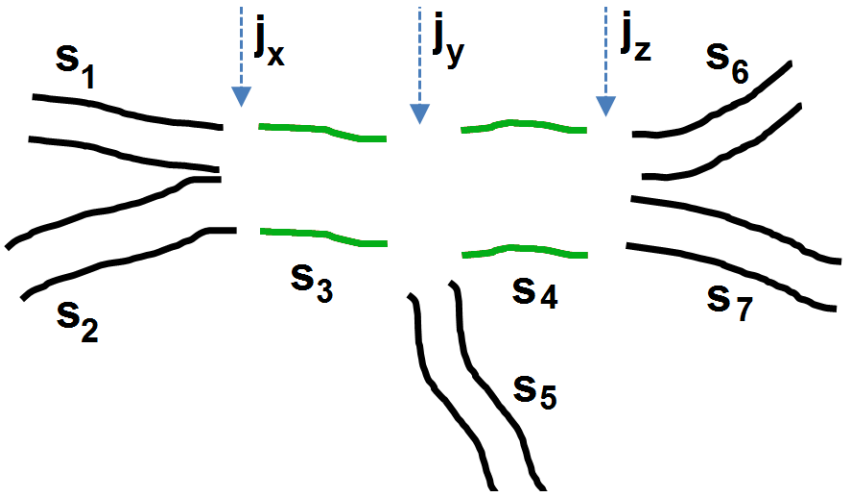

Fig. 4.18 The illustration shows multiple overlapping segments (in green colour) appeared consecutively. The dotted arrows indicate threes junction points.

framework of probability, two automated systems, one for forming junctions and the other for estimating the probabilities of junction configuration are presented.

An efficient region-based algorithm is presented for forming junctions (groups) of segment ends having the potential to be connected to each other. Using the direction vector and angles at each segment end, the algorithm dynamically specifies local regions at the segment end to explore its mutual association with endings of other segments in close proximity.

Using Bayes theorem, a comprehensive probabilistic model is presented and trained for estimating the most probable connectivity of broken segments locally at junctions. The system enumerates all possible configurations of segment ends at junction and estimates the posterior probability of each configuration using the configuration likelihood (conditioned on geometrical and colour features of segments) and prior probabilities obtained from a supervised training process

In addition, a new benchmark vessel-classified set is introduced for DRIVE image database. This dataset is designed to support the evaluation of the performance of proposed systems and is free for study and research purposes.

The experimental details of the systems developed for junction formation and probability estimation for local configurations are provided in evaluation Chapter 6.

Chapter 5

Arterial and Venous Trees Extraction

5.1 Introduction

This chapter presents a novel graph-based method for arterial and venous tree extraction from a network of disconnected and unlabelled vessel segments in fundus images. Through an efficient procedure, the problem of classifying and connecting vessel segments is translated into a general binary labelling problem expressed in a probability-based dependency graph. The translation represents the segment network as using a number of MRF graphical models. The formulated MRFs express joint probability distributions by treating segment class probabilities as conditional likelihoods (unary node potentials), and segment connectivity probabilities as priors (pairwise edge potentials). The conditional likelihood is obtained by training a Naïve Bayesian classifier. Unlike conventional labelling methods that utilise only the colour properties of vessels, the proposed classifier exploits both colour and spatial properties of the vasculature to efficiently classify vessels in situations when the images are unprocessed or have non-uniform contrast. In addition, a fairly simple approach is developed to identify number of disjoint networks out of

the entire network of segments, for each of which a unique MRF graph is established.

On each formulated MRF, the $\mathbb{ST}$-cut is obtained to infer the optimal global configuration. The $\mathbb{ST}$-cut is implemented using the well-known Ford-Fulkerson algorithm, followed by back-translation of configured MRFs to configured-disjoint-networks. In configured disjoint networks, the linking of extracted identical class sub-trees is performed in order to extract complete trees of arteries and veins. Linking of sub-trees resolves the problem of missing segments to a great extent.

This chapter is organized as following: Section 5.3 describes the method to detect disjoint networks in a single segment network. Section 5.4 explains a procedure to represent the identified disjoint networks in MRFs models. Section 5.6 and Section 5.5 describe the methods for calculating both unary and pairwise potentials. The underlying functions used in estimating the pairwise potentials are explained in Chapter 4. The method for extracting AV trees by obtaining the global configuration, back translation, then connected sub-trees is explained in Section 5.7.

5.2 The Vasculature as an MRF

Conventionally, the MRF graph used for labelling problems in the field of computer vision represents a 2-dimensional grid of image pixels as a network of nodes connected to each other via a 4 or 8-neighbourhood system, as explained in Chapter 3. Each node possesses a unary potential as the likelihood of belonging to certain class, determined by any cost or probability function. Any two neighbouring nodes possess a pairwise potential (weight of the edge between them) which usually expresses

smoothness or connectivity probability.

The translation of an image into an MRF is fairly straightforward. However, representing domain-specific objects or states and their associations into an MRF along with appropriate functions to obtain unary and pairwise potentials is more complex. To this end, the following sections explain the procedures for identifying disjoint networks, representing each identified disjoint network into MRF, and estimating pairwise and unary potentials for nodes; followed by applying inference technique to estimate optimal global labelling and connectivity configuration.

5.3 Disjoint Network Identification

According to **Definition 8** given in Section 4.3, a superset **F** is a set of one or more disjoint networks F_i, each consisting of single or multiple overlapping vascular trees. A typical retinal fundus image contains several disjoint networks of segments. In a completely and accurately segmented vasculature, all disjoint network F_i are strictly separated from each other. In such rigid conditions, identifying true disjoint networks of connected trees is straightforward. However, in case of network of disconnected segments, accurately identifying disjoint networks of discontinued segments is non-trivial as the accuracy is highly dependent on the outcome of junction formation process.

In this thesis, a simple propagation algorithm is used to identify all disjoint networks of disconnected segments present in a retinal image. The approach works by first randomly selecting a segment, exploring its associated junctions at both ends to find other associated segments to the same junctions, and iteratively tracking

each newly found segment until the search exhausts. All explored segments are then associated to a single disjoint network F_i. Using this approach, the set of segments is divided into several mutually separate disjoint networks which can be subsequently resolved. All segments in an image are explored once, and are associated to exactly one disjoint network F_i. Any two segments (s_a^r and s_b^r) of a disjoint network F_i must be directly associated to each other via a junction j_x or having association like ($s_a^r \in j_x$, $s_b^r \in j_y$, $s_c^r \in j_x$, $s_c^{r'} \in j_y$).

A descriptive algorithm (**Algorithm 1**) is given below that identifies disjoint networks in the network of disconnected segments.

A sample image with several identified disjoint networks is shown in Figure 5.1, each assigned with a unique colour. Note that a disjoint network may consist of a single segment only.

5.4 Disjoint Network Translation into MRF

An appropriate translation of a disjoint network of segments into MRF graph is performed by representing each singleton segment s_i of disjoint network F as a unique node in MRF. For any labelling problem expressed in MRF, the fundamental assumption is that every node in MRF is a random variable that can be assigned a label from a predefined set of labels-in this case from $\mathscr{L} = A, V$ (artery or vein).

In addition to this, an undirected edge between nodes of the MRF indicates an association or label dependency, i.e. any two nodes connected via an edge in MRF express conditional dependence between their labels. The segments in the vasculature are associated with each other through the junctions their ends belong to. Also, all segments associated with a junction are mutually dependent on each other

Algorithm 1: IdentifyForests

Input:
Queue $\mathbf{S} = \{s_1^h, s_1^t, s_2^h, s_2^t, s_3^h, s_3^t, ...s_n^h, s_n^t\}$ // set of ends of all segments
Queue $\mathbf{J} = \{j_1, j_2, j_3, ...j_m\}$ // set of all identified junctions
whereas: $j_k = \{s_a^r, s_b^r, s_c^r, ...|r \in \{h,t\} \wedge s_a^r, s_b^{r'} \Rightarrow a \neq b\}$
Disjointnetworks $\boldsymbol{F}$
Output:
$F_i = \big\{\{S_i\}, \{J_i\} \big| i = 1,2,3...\big\}$
begin
  $i \longleftarrow 1$ // GlobalVariable
  while $\boldsymbol{S} \neq \emptyset$ **do**
    $j \longleftarrow dequeue(\mathbf{J})$
    $SearchAssociatedSegmentEnds(j)$
    $i \longleftarrow i+1$

procedure $SearchAssociatedSegmentEnds(j)$
 enqueue $J_i(j)$
 Mark j as *explored*
for $\forall_{s_a^r}$ *in* $\boldsymbol{F}.IncidentSegment(j, s_a^r)$ **do**
  if s_a^r *is unexplored* **then**
    $temp \longleftarrow \boldsymbol{F}.Adjacent Junction(j,s)$ **if** *junction temp is unexplored* **then**
      enqueue $S_i(s_a^r)$
      dequeue $\boldsymbol{S}(s_a^r)$
      Mark s_a^r as *explored*
      dequeue $\boldsymbol{J}(temp)$
      Mark *temp* as *explored*
      $SearchAssociatedSegmentEnds(temp)$ // Recursive Call

when labeled. Thus the association between any two segments (s_a, s_b) via junction j_k, can be represented by means of a direct edge between nodes s_a and s_b in MRF. For instance, a junction with five associated segment ends is represented in MRF as a Maximal Clique in which all five nodes are adjacent with each other as shown in Figure 5.2. Another example of vasculature translation into MRF is given in Figure 5.3.

Formally, a disjoint network F consisting a set S of vessel segments s_a, such that segments of S are associated with each other by means of their respective junctions j_k of junction set J, is mapped into an MRF graph $\mathcal{G}(\mathcal{V}, \mathcal{E})$, such that the node set $\mathcal{V}$ is the bijection of set S with identical denotations and indices; whilst the edge set $\mathcal{E}$ is the set of edges between nodes of $\mathcal{V}$ such that each edge $e(s_a, s_b)$ must satisfy the condition, i.e. $e(s_a, s_b) = e(s_b, s_a) \Rightarrow (s_a^r, s_b^r \in j_k)$.

Note that if any two nodes are adjacent $(s_a \sim s_b)$ in $\mathcal{G}$, it doesn't necessarily mean that their corresponding segments belong to the same joint; rather it merely expresses an association between their specific ends via some junction j_k. Later, the edge between nodes s_a and s_b in $\mathcal{G}$ will be severed if the inference process finds the two nodes (segments) are not the part of the same joint at junction j_k.

It is important to mention that the representation of all segments as nodes does not include overlapping segments. The reason to represent only non-overlapping segments into the MRF is that the formulated MRF will consider the graph for binary labelling (i.e. artery and vein), whilst overlapping segments are unclassifiable segments.

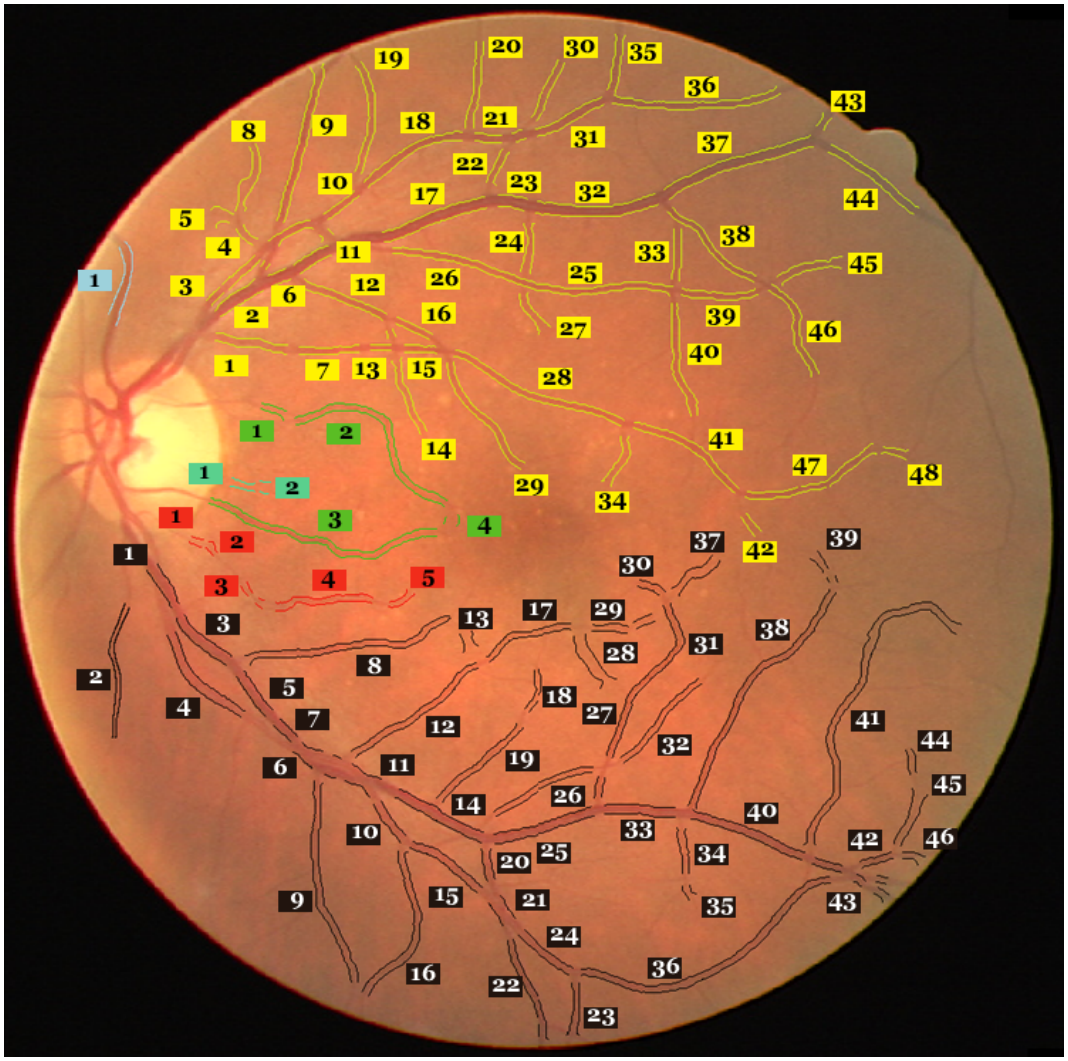

Fig. 5.1 A number of disjoint networks are shown. Each disjoint network consists of one to several numbers of associated segments. All segments associated to a disjoint network are shown with a colour unique to the one any other disjoint network segments have.

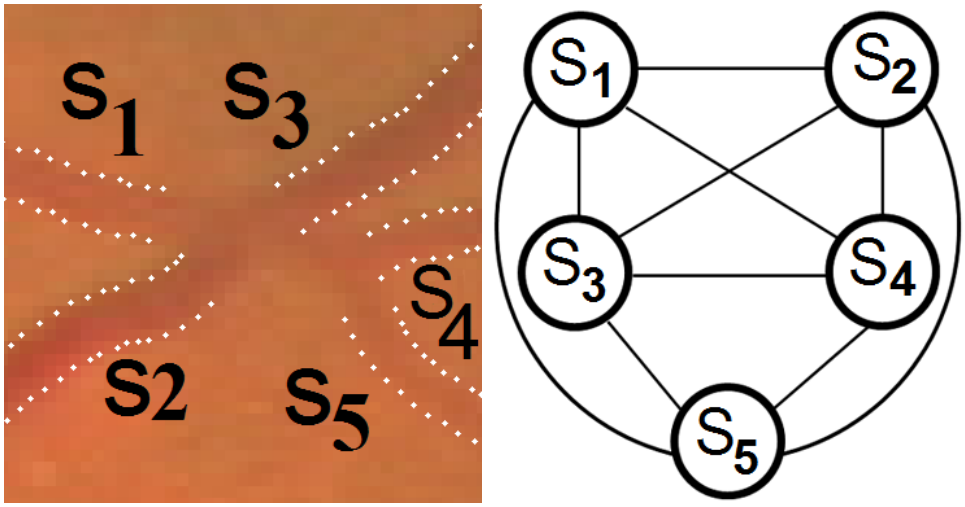

(a) (b)

Fig. 5.2 A junction with five associated segment ends with its representation in MRF as maximal clique. All nodes have direct edges among each other.

Referring to the example shown in Figure 4.17, the single overlapping segments are resolved by merging the two junctions (associated with overlapping segment) into one junction, thus the representation includes only j_z with four associated segments s_2, s_3, s_4 and s_5. A similar procedure also applies to multiple consecutive overlapping segments, the representation requires merging all the junctions, with which overlapping segments are associated, into a single junction. Referring to the example in Figure 4.18, the junctions j_x, j_y and j_z are merged into one junction j_k before representation by the MRF, as shown in Figure 5.4. However, merging more than two neighbouring junctions into single junction may raise configuration issues with the complexity of the configuration step. This issue is discussed and resolved in Section 5.5.

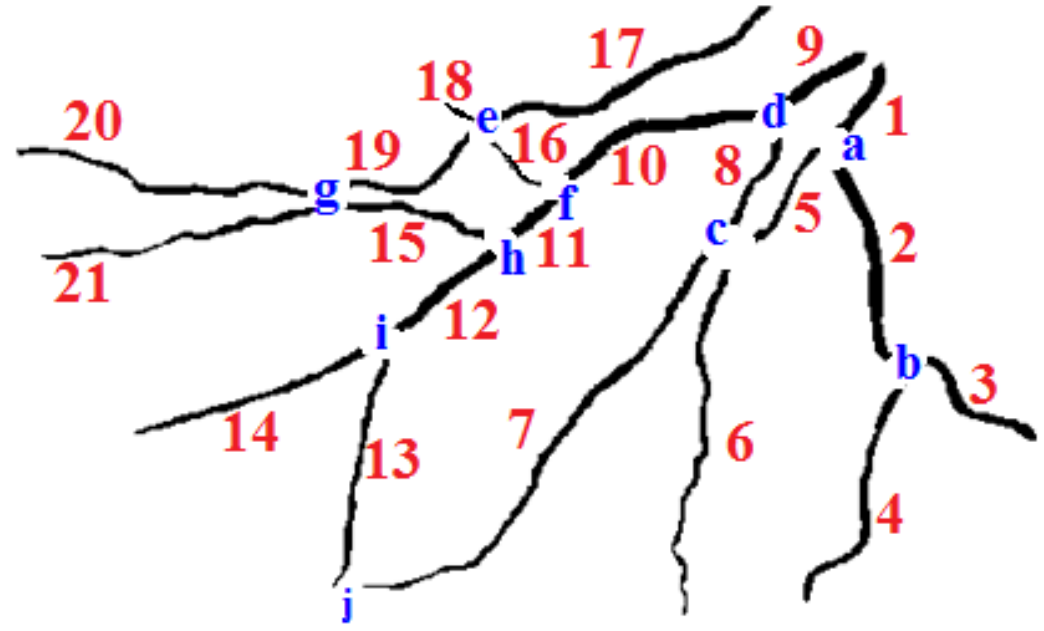

(a)

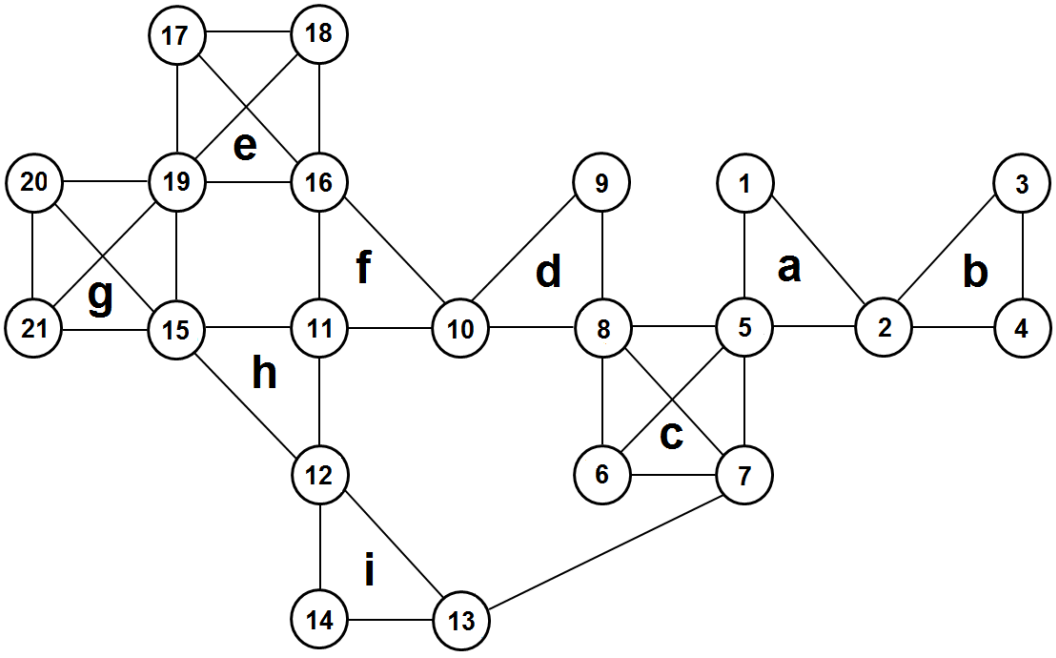

(b)

Fig. 5.3 (a) An example of a network of vessel segments; (b) and its corresponding representation as MRF. Segments of vasculature are represented as nodes and their associations at junctions are expressed by direct links in the MRF. All segments are represented by numeric indices and junctions by alphabetic indices.

5.5 Pairwise Potential of Nodes

The weight $w(s_a, s_b)$ is the pairwise potential of the edge $e(s_a, s_b)$ in $\mathcal{G}$. It represents the probability that corresponding segments (s_a, s_b) are part of the same joint and thus belong to identical class. This is very similar to MRF-based image segmentation, in which any two neighbouring pixels of an object tends to have strong bonds (smoothing, less variation, etc.) with each other, while there are weak bonds at object boundaries. In binary labelling problems, the pairwise potential is typically the cost of assigning opposite labels to adjacent nodes (Wang et al., 2013). Thus, using rule 10 (stated in Section 4.3), the pairwise potential (weight of an edge) between any adjacent nodes in $\mathcal{G}$ is the probability of connectivity of corresponding segment ends at their respective junction j_k, i.e. $w(s_a, s_b) = p(s_a \leftrightarrow s_b)$.

Using the addition law of probability, the connectivity probability of segments s_a and s_b at j_k, is the sum of the probabilities of all those configurations at j_k in which s_a and s_b are the part of same joints, i.e.

$$p(s_a \leftrightarrow s_b) = \sum_q p(C_q^k), where.(s_a, s_b) \in L_y^k \wedge L_y^k \in C_q^k \tag{5.1}$$

Where, C_q^k is q^{th} configuration at the k^{th} junction, and L_y^k is the y^{th} potential joint composed of ends of segments s_a and s_b at k^{th} junction. Similarly, the probability that segments s_a and s_b are disconnected at j_k, is equal to the sum of probabilities of all those configurations at j_k in which s_a and s_b are the part of different joints. In addition, the terms $p(s_a \leftrightarrow s_b)$ and $p(s_a \leftrightarrow s_b | f_k)$ refer to the same quantity and thus can be interchangeably used; where f_k is the set of measured features at the junction. In the context of energy minimization on MRF, the pairwise potential $p(s_a \leftrightarrow s_b)$ is the cost of assigning opposite labels to nodes s_a and s_b by disconnecting them. A

preliminary step is to normalize all configurations $p(C_q^k|j_k)$ at j_k to 1 before utilizing for estimating connectivity probability.

Example: Let a junction j_k has three associated segment ends $\{s_a, s_b, s_c\}$ as shown in Figure 5.5(a). There are seven configurations, i.e. three with one bifurcation $C_1^k = \big\{\{s_a, \{s_b, s_c\}\}, C_2^k = \big\{s_b, \{s_a, s_c\}\big\}$, and $C_3^k = \big\{s_c, \{s_a, s_b\}\}\big\}$, three with one bridge and one terminal $C_4^k = \big\{\big(\{s_b, s_c\}\big), \{s_a\}\big\}, C_5^k = \big\{\big(\{s_a, s_c\}\big), \{s_b\}\big\}, C_6^k = \big\{\big(\{s_a, s_b\}\big), \{s_c\}\big\}$, and one with three terminals $C_7^k = \big\{\big(\{s_a\}\big), \big(\{s_b\}\big), \big(\{s_c\}\big)\big\}$.

Notice that from a connectivity standpoint, C_1^k, C_2^k and C_3^k are identical as all three segment ends (s_a, s_b, s_c) at j_k in C_1^k through C_3^k must be connected to each other to compose a bifurcation joint. However, the probability of the configuration varies with the parent segment of the bifurcation.

To estimate $p(s_a \leftrightarrow s_b|j_k)$, the relevant configurations are C_1^k, C_2^k, C_3^k, and C_6^k. Thus, $p(s_a \leftrightarrow s_b|j_k) = p(C_1^k|j_k) + p(C_2^k|j_k) + p(C_3^k|j_k) + p(C_6^k|j_k)$. Similarly, $p(s_a \leftrightarrow s_c|j_k) = p(C_1^k|j_k) + p(C_2^k|j_k) + p(C_3^k|j_k) + p(C_5^k|j_k)$, and $p(s_b \leftrightarrow s_c|j_k) = \sum_{q=1}^{4} p(C_q^k|j_k)$.

A junction with two segment ends s_a and s_b has only two configurations, one with two terminals $C_1^k = \big\{\big(\{s_a\}\big), \big(\{s_b\}\big)\big\}$, and the other with one bridge $C_2^k = \big\{s_a, s_b\big\}$. The only relevant configuration to estimate the connectivity probability of s_a and s_b is C_2^k, thus $p(s_a \leftrightarrow s_b|j_k) = p(C_2^k|j_k)$.

The aforementioned examples consider junction cardinality $|j_k|$ = 3 and 2 respectively; a similar procedure Equation 5.1 is applicable to any large number, e.g. with $|j_k| = 4$ 22 are configurations.

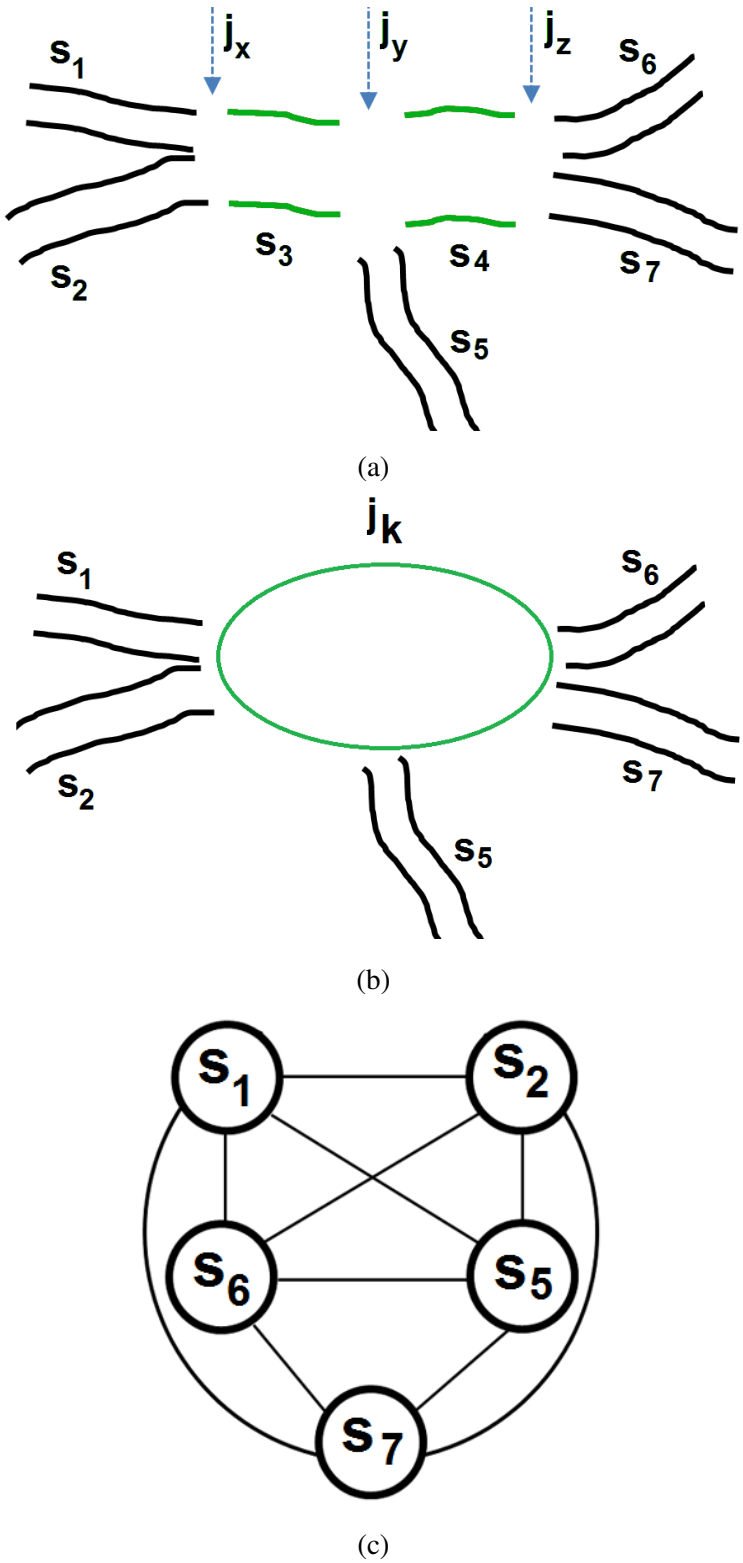

Fig. 5.4 (a) The consecutive overlapping segments s_3 and s_4 are shown in green. (b) The junctions j_x, j_y, and j_z are merged into single junction j_k by ignoring overlapping segments s_3 and s_4. (c) The equivalent MRF graph for junction j_k is shown.

The quantity $p(C_q^k|j_k)$ is estimated using Equation 4.3.

Referring to the example given in Figure 5.4, estimating the pairwise potential for nodes at junctions including overlaps is non-trivial. In the original vasculature, the segment s_5 is not directly associated to any of segments (s_1, s_2, s_6, s_7) at junction j_k, nor are segments s_1 and s_2 directly associated with s_6 and s_7, considering a joint that is composed of segment ends which truly belong to different junctions is misleading. Considering a true joint to include an overlap segment is also infeasible as the features extracted from an overlapping segment don't follow proper ratios with features extracted from non-overlapping segments.

To address this, the pairwise potential between any two nodes (segments) that appear on such junction, is set to 0.5, giving an equal probability for any two nodes to be connected or disconnected.

5.6 Classification of Segments (Unary Potential)

The vessels in the retina originate from the optic nerve head (ONH) and spread through the retinal perfusion area by means of bifurcations. The vessel segments near the ONH usually have prominent colour and geometrical features and thus are easily class distinguishable. However, moving farther away from ONH, at every bifurcation, each child has smaller width than of its parent segment; and thus after several successive bifurcations, the vessel segments become as thin that their colour and geometrical measurements become insufficient to distinguish their classes. These vessels can be termed so *thin* segments denoted by $\bar{s_c}$, whilst all other segments as *major* segments denoted by $\hat{s_a}$. In the following Section 5.6.1, the class probability

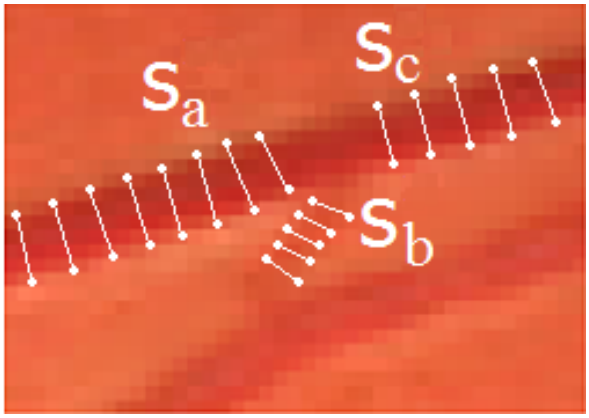

(a)

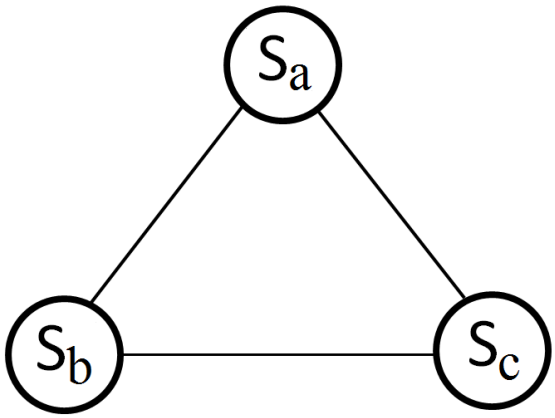

(b)

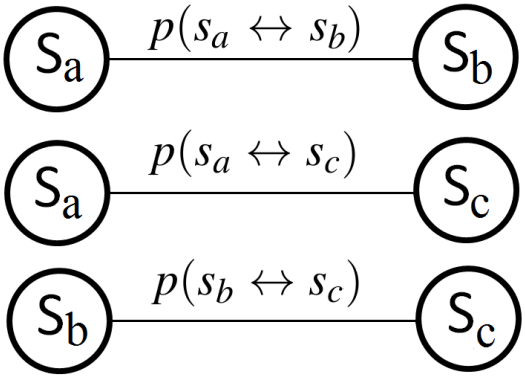

(c)

Fig. 5.5 The junction with three segments is translated into an MRF, where each link between any two neighbouring nodes expresses its connectivity probability as a pairwise potential.

(*unary potential*) is estimated for each node (referring to a unique *major* segment) of the MRF $\mathcal{G}$.

5.6.1 Classifying Major Vessel Segments

Through supervised learning, a Naïve Bayesian classifier is trained for estimating the class probabilities of *major* segments using colour and geometrical features of segments. Let $\hat{s_a}$ be a *major* segment with feature set $f_a = \{w_a, \eta_a, \psi_a, v_a\}$, then class probability $p(\hat{s_a} = l|f_a)$ can be estimated as:

$$p(\hat{s_a} = l|f_a) = \frac{p(f_a|\hat{s_a} = l)p(\hat{s_a} = l)}{\sum_{u=l}^{l'} p(f_a|\hat{s_a} = u)p(\hat{s_a} = u)} \tag{5.2}$$

$$p(f_a|\hat{s_a} = l) = \mathcal{N}(\mu_w, \sigma_w)\mathcal{N}(\mu_\eta, \sigma_\eta)\mathcal{N}(\mu_\psi, \sigma_\psi)\mathcal{N}(\mu_v, \sigma_v) \tag{5.3}$$

The $p(\hat{s_a} = l)$ is the prior probability, i.e. occurring frequency of segment with true label l in the training set as $p(\hat{s_a} = A) = 0.46$ and $p(\hat{s_a} = V) = 0.53$. The term $p(f_a|\hat{s_a} = l)$ is the probability density function for class label l. The features of segments s_a including w_a, η_a, ψ_a, and v_a denote average width, average hue, average saturation and average intensity respectively. It should be noted that these features are extracted by considering all profiles of the segment in contrast to the process of estimating configuration probabilities where features were extracted from the seven end profiles.

To optimize the classifier, the mean and standard deviation (μ, σ) for each feature were estimated. A training set of 300 arterial and 348 venous *major* segments (segments with average width $w_a >= 3.5$ pixels) in in DSJS training sets of 20 colour images. The frequency distributions of feature set were modelled as normally

	Width	Hue	Saturation	Intensity
Arteries (A)	μ_w^A=4.3 σ_w^A=0.8	μ_η^A=0.057 σ_η^A=0.002	μ_ψ^A=0.68 σ_ψ^A=0.03	μ_v^A=0.74 σ_v^A=0.02
Veins (V)	μ_w^V=4.8 σ_w^V=1.3	μ_η^V=0.044 σ_η^V=0.008	μ_ψ^V=0.74 σ_ψ^V=0.02	μ_v^V=0.61 σ_v^V=0.03

Table 5.1 Estimated parameters of feature distributions

distributed with parameters (μ, σ) given in Table 5.1. The class probabilities of all minor segments $\bar{s_c}$ are set to 0.5, i.e. $p(\bar{s_c} = l) = p(\bar{s_c} = l^{'}) = 0.5$.

5.6.1.1 Spatial Properties of Retinal Vessels

To determine the retinal vessel class, the intensity is the most useful colour feature. The arteries carry oxygenated blood and often have a light reflex visible in the centre, and thus usually have higher intensity than veins. However, the intensity is insufficient to distinguish arteries when the contrast in the perfusion area of an unprocessed fundus image is not uniform. A good number of arterial and venous segments in the training set were found with similar mean intensities and thus equal probability of being classified as arteries or veins. This can be seen in a fundus image in Figure 5.6.

Assuming the image contrast is relatively constant in local regions, the aforementioned issue can be resolved to a great extent by considering the distribution of colour properties of segments in close neighbourhoods. As the sample of regions provided in Figure 5.7 demonstrates, the intensity of major arteries is normally higher than the intensity of major veins in a close neighbourhood. Thus a significant difference in intensities between any two neighbouring major vessel segments is a good indication that they belong to opposite classes. To this end, the neighbourhood of a segment is defined below, followed by extending the Naïve Bayes classifier, given in Equation

5.2, by introducing a spatial feature intensity-ratio.

Analysing features of retinal vessels locally inside concentric zones while taking the ONH as the centre is a common practice adopted by many researchers, as in ((Grisan and Ruggeri, 2003), (Saez et al., 2012), (Relan et al., 2013)). In this thesis, a slightly different approach is used to define neighbourhood of a segment. Formally, the neighbourhood of segment $\hat{s_a}$ is defined as the circular zone z_a around $\hat{s_a}$ such that the coordinates of the centre point of z_a and middle pixel of the centreline of segment $\hat{s_a}$ are similar, as shown in Figure 5.8. The diameter of zone z_a is equal to double the average diameter size of the normal optic nerve head. For DRIVE images, the average diameter of healthy ONH is manually measured and is equal to 82 pixels. A neighbouring segment of $\hat{s_a}$ is any major segment $\hat{s_b}$ laying (partly or completely) in z_a. If multiple neighbouring candidates for $\hat{s_a}$ exist in z_a, the one with greatest length is treated as the neighbouring segment for $\hat{s_a}$.

Let $\hat{s_a}$ and $\hat{s_b}$ are the two neighbouring major segments with mean intensities as v_a and v_b respectively, then the intensity ratio $\zeta_{a,b}$ is given as:

$$\zeta_{a,b} = \frac{min(v_a, v_b)}{max(v_a, v_b)} \tag{5.4}$$

During the training process, the intensity ratio $\zeta_{a,b}$ is extracted from identical and opposite class neighbouring major segments. The frequency distribution of $\zeta_{a,b}$ for identical and opposite class neighbouring major segments is identified with parameters μ_{ζ}^{I}=, σ_{ζ}^{I} =, μ_{ζ}^{O} =, σ_{ζ}^{O} =. Whereas, I and O denote identical and opposite class segments respectively. The probability that the two neighbouring major segments $\hat{s_a}$ and $\hat{s_b}$ belong to opposite vessel classes is given as:

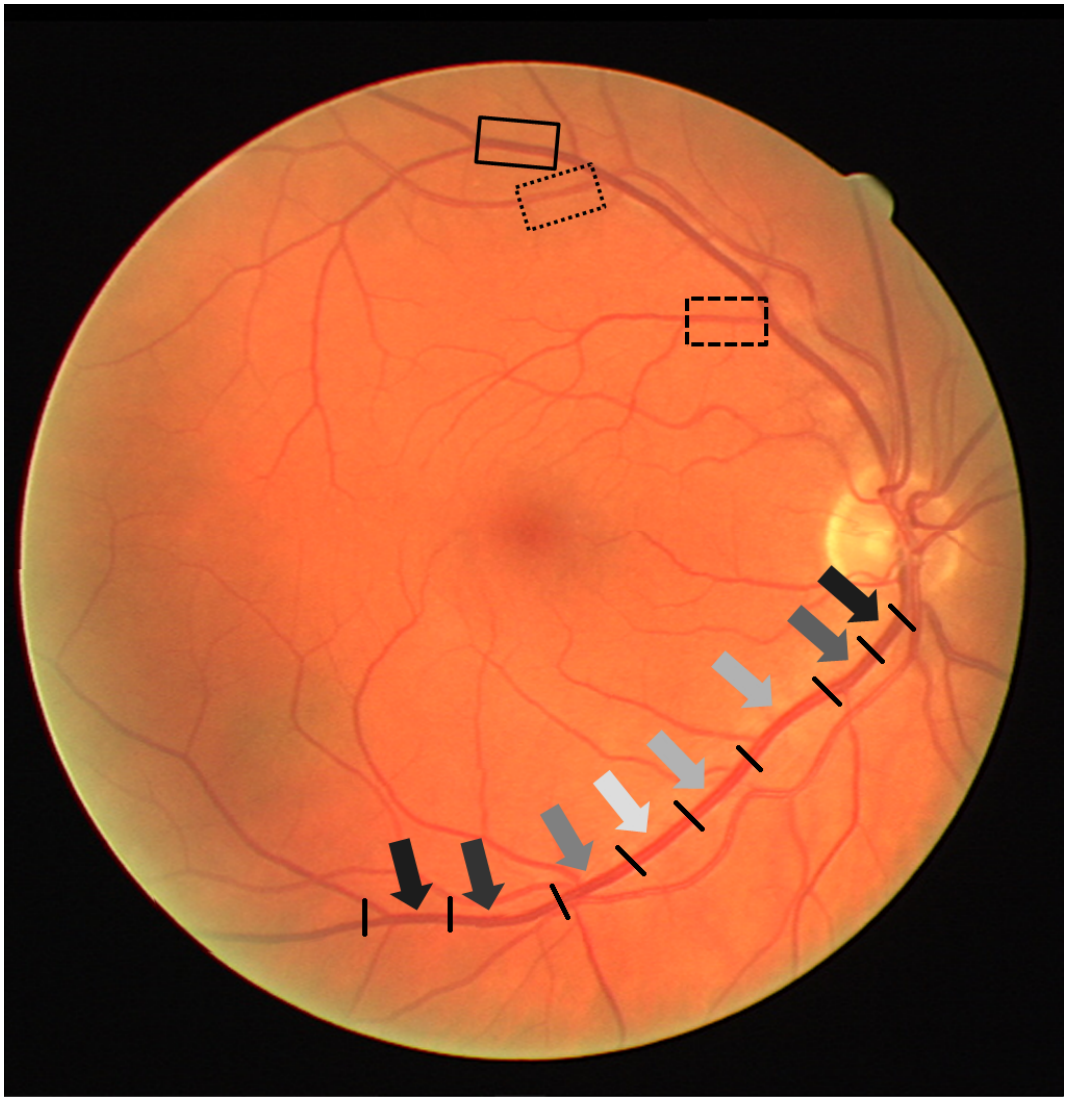

Fig. 5.6 The mean intensity of the major vein in the lower arc varies gradually. The downward-pointing arrows along the vein highlight the variation of mean intensity between partitions. The intensity of the arrow is exaggerated to illustrate the relative intensities of the segments. The chances of misclassification are high, if the intensity of segment in each partition is analysed independently. In addition, in the upper arc, the intensity of a vein segment (shown in dashed-block) appears higher than intensity of artery segment (shown in dotted-block). However, the same artery segment (shown in dotted-block) has higher intensity than its neighbouring vein segment (shown in solid-block).

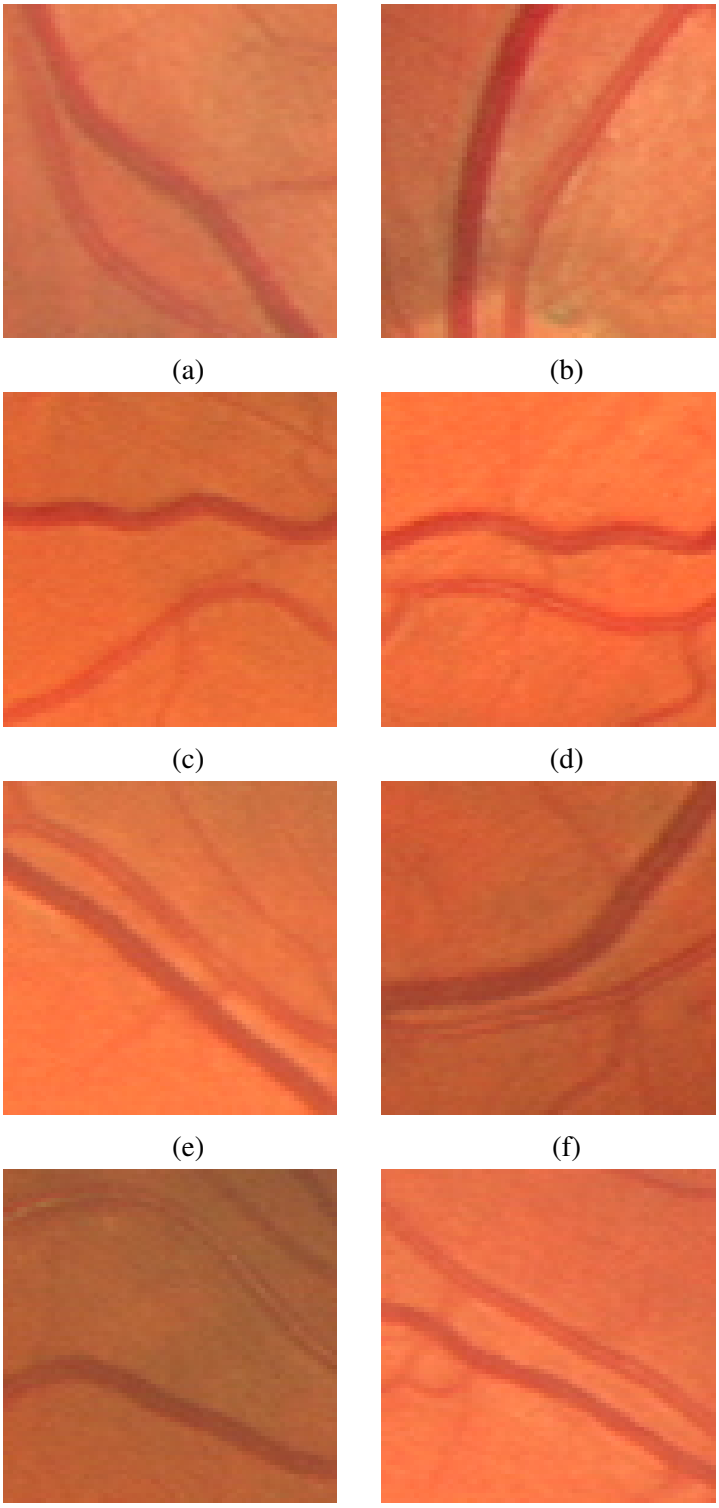

Fig. 5.7 (a)-(h), Major arteries and veins are present in small neighbourhoods. The arteries are lighter than veins.

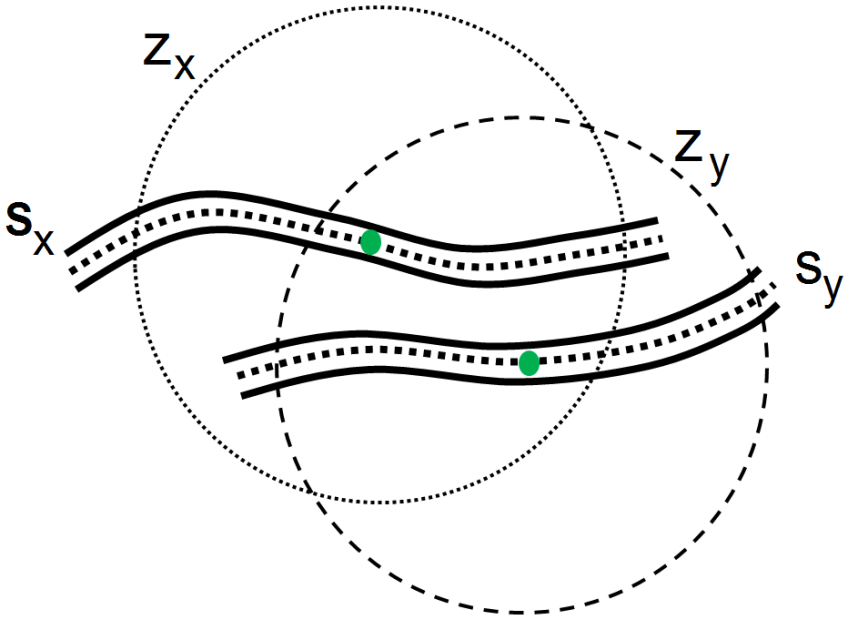

Fig. 5.8 Two spatially close segments s_x and s_y are shown, each with its neighbourhood zone. Each circular zone has diameter double the size of normal ONH.

$$p(\hat{s_a} = l, \hat{s_b} = l' | \zeta_{a,b}) = \frac{p(\zeta_{a,b} | \hat{s_a} = l, \hat{s_b} = l')}{p(\zeta_{a,b} | \hat{s_a} = l, \hat{s_b} = l) + p(\zeta_{a,b} | \hat{s_a} = l, \hat{s_b} = l')} \tag{5.5}$$

Whereas:

$$p(\zeta_{a,b} | \hat{s_a} = l, \hat{s_b} = l) = \mathcal{N}(\mu^I_{\zeta_{a,b}}, \sigma^I_{\zeta_{a,b}}) \tag{5.6}$$

and

$$p(\zeta_{a,b} | \hat{s_a} = l, \hat{s_b} = l') = \mathcal{N}(\mu^O_{\zeta_{a,b}}, \sigma^O_{\zeta_{a,b}}) \tag{5.7}$$

When $v_a > v_b$, and l corresponds to artery (A), the classifier is updated as:

$$p(\hat{s_a} = l|f_a) = \frac{p(f_a|\hat{s_a} = l)p(\hat{s_a} = l)}{\sum_{u=l}^{l'} p(f_a|\hat{s_a} = u).p(\hat{s_a} = u)} p(\hat{s_a} = l, \hat{s_b} = l'|\zeta_{a,b}) \tag{5.8}$$

and

$$p(\hat{s_a} = l'|f_a) = \frac{p(f_a|\hat{s_a} = l)p(\hat{s_a} = l)}{\sum_{u=l}^{l'} p(f_a|\hat{s_a} = u).p(\hat{s_a} = u)} \big(1 - p(\hat{s_a} = l, \hat{s_b} = l'|\zeta_{a,b})\big) \tag{5.9}$$

When $v_a \leq v_b$, and l corresponds to artery (A), the classifier is updated as:

$$p(\hat{s_a} = l|f_a) = \frac{p(f_a|\hat{s_a} = l)p(\hat{s_a} = l)}{\sum_{u=l}^{l'} p(f_a|\hat{s_a} = u).p(\hat{s_a} = u)} \big(1 - p(\hat{s_a} = l, \hat{s_b} = l'|\zeta_{a,b})\big) \tag{5.10}$$

and

$$p(\hat{s_a} = l'|f_a) = \frac{p(f_a|\hat{s_a} = l)p(\hat{s_a} = l)}{\sum_{u=l}^{l'} p(f_a|\hat{s_a} = u).p(\hat{s_a} = u)} p(\hat{s_a} = l, \hat{s_b} = l'|\zeta_{a,b}) \tag{5.11}$$

The quantity $p(\hat{s_a} = l, \hat{s_b} = l'|\zeta_{a,b})$ must be carefully used; a value less than 0.5 indicates the two segments $\hat{s_a}$ and $\hat{s_b}$ are more likely to belong to the same class. In such a case, updating Equation 5.2 in Equations (5.8-5.11) may mislead the classifier, and is thus omitted, i.e. the original Equation 5.2 is used.

In the rest of the algorithm, major and minor segments are treated identically, and $\bar{s_a}$ or $\hat{s_a}$ is written as s_a.

5.7 Artery Vein Trees Extraction

Having translated the segments network into an MRF graph, the segment connectivity and classification problem resolve to a general MRF based binary labelling problem, where any appropriate inference technique can be applied to derive global labelling and connectivity.

Some of the families of MRF inference techniques are Graph Cuts (Boykov et al., 2001), Linear Programming (Glocker et al., 2008), and Simulated Annealing (Geman and Geman, 1984). To obtain best achievable results, one could theoretically perform a global *MAP* estimation by considering the joint probabilities of unary and pairwise potentials of nodes. However, this requires an exhaustive search which may be computationally infeasible for complex cases. Out of the vast range of inference techniques, the $\mathbb{ST}$-graph cut has been extensively used in computer vision problems. The $\mathbb{ST}$-graph cut using the Ford-Fulkerson algorithm requires polynomial time to find a global optimal solution which usually corresponds to *MAP* estimation for a binary labelling problem. This has strong theoretical support from the maximum-flow minimum-cut theorem as described in Chapter 3.

For binary labelling problems, an $\mathbb{ST}$-graph is a directed MRF graph with two additional nodes $\mathbb{S}$ and $\mathbb{T}$ termed the *source* and *sink* such that the in-degree of *source* node $(d_{\Gamma}^{-}(\mathbb{S}))$ and out-degree of *sink* node $(d_{\Gamma}^{+}(\mathbb{T}))$ is zero. We transform the formulated graph $\mathcal{G}$ to $\mathbb{ST}$-graph $\vec{\mathcal{G}}_{\mathbb{ST}}$, such that in $\vec{\mathcal{G}}_{\mathbb{ST}}$ there exists directed edges (known as t-links) $e(\mathbb{S}, s_a)$ and $e(s_a, \mathbb{T})$ for each node (s_a); and directed edges in both directions (known as n-links) between s_a and s_b, i.e. $e(s_a, s_b)$ and $e(s_b, s_a)$ for all neighbouring nodes. The additional nodes $\mathbb{S}$ and $\mathbb{T}$ refers to two labels l and $l^{'}$. The

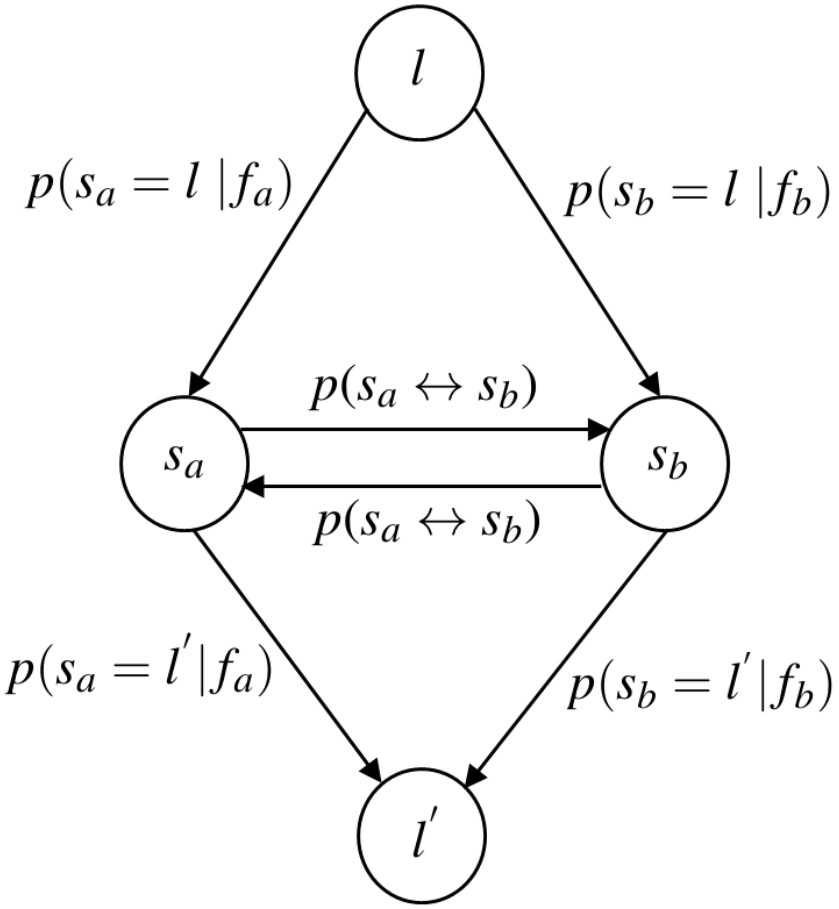

Fig. 5.9 A sample $\mathbb{ST}$-Graph with four nodes, i.e. $source(l)$ node, $sink(l')$ node, and two nodes denoting segments s_a and s_b. The pairwise potential of s_a and s_b is expressed as the weight of each edge between them. The pairwise potential demonstrates how probable s_a and s_b are from identical class and thus connected to each other. The unary potentials are shown with the edges, to and from, s_a and s_b. The unary potential is the probability a node belongs to certain class (l or l').

capacity of a t-link is the class likelihood (unary potential) of each node s_a towards a specific label l or $l^{'}$, i.e. the capacity $c(\mathbb{S}, s_a)$ of edge $e(\mathbb{S}, s_a)$ is equal to $p(s_a = l|f_a)$, and $c(s_a, \mathbb{T})$ of edge $e(s_a, \mathbb{T})$ is equal to $p(s_a = l|f_a)$. Similarly, the capacity of n-link (edge) between adjacent nodes is the pairwise potential (probability of connectivity between nodes), given as $c(s_a, s_b) = c(s_b, s_a) = p(s_a \leftrightarrow s_b)$. An example of two neighbouring nodes s_a s_b in $\mathbb{ST}$ graph is shown in Figure 5.9.

After formulating $\vec{\mathcal{G}_{\mathbb{ST}}}$, the objective is to find a global minimum cut that divides the graph into sub graphs such that there is no path left from $\mathbb{S}$ to $\mathbb{T}$. The max-flow min-cut theorem states that the maximum flow in an $\mathbb{ST}$-graph is equal to the minimum cut configuration on the $\mathbb{ST}$-graph. The minimum cut is inferred by finding the maximum flow on $\vec{\mathcal{G}_{\mathbb{ST}}}$ using Ford-Fulkerson algorithm discussed in Chapter 3. A minimum cut is demonstrated in Figure 5.10.

5.7.1 Back-Translation of Configured MRF to Labelled Trees

The AV trees extraction process involves back-translation of the final residual graph $\mathcal{G}^{'}_{\mathbb{ST}}$ to $\acute{F}$ (configured disjoint network) after obtaining the minimum cut on $\vec{\mathcal{G}_{\mathbb{ST}}}$. The segments corresponding to nodes which are connected to *source* node in $\mathcal{G}^{'}_{\mathbb{ST}}$ are labeled l in $\acute{F}$ provided *source* node was considered as l during formulating $\vec{\mathcal{G}_{\mathbb{ST}}}$. The opposite label $l^{'}$ is assigned to the segments in $\acute{F}$ corresponding to nodes which are connected to *sink* node in $\mathcal{G}^{'}_{\mathbb{ST}}$. Any two segment ends associated to a junction in F are connected to each other in $\acute{F}$ if their corresponding nodes are connected in $\mathcal{G}^{'}_{\mathbb{ST}}$ after separating *source* from *sink*; they remained unconnected otherwise. In

Figure 5.11 the back-translation of $\mathcal{G}'_{\mathbb{ST}}$ to $\acute{F}$ is illustrated.

Formally, a disjoint network F, consisting of segments of $S = \{s_1, s_2, s_3...\}$ which are associated with each other through their respective junctions of set $J = \{j_1, j_2, ...\}$, is translated to an MRF graph $\vec{\mathcal{G}}_{\mathbb{ST}}$ using the procedures explained in Section 5.4, Section 5.5, and Section 5.6. The Ford-Fulkerson algorithm runs on $\vec{\mathcal{G}}_{\mathbb{ST}}$ resulting in a final residual graph $\mathcal{G}'_{\mathbb{ST}}$. The following rules, assuming the *source* and *sink* node in $\mathcal{G}'_{\mathbb{ST}}$ represents label l and l' respectively, are then applied to translate $\mathcal{G}'_{\mathbb{ST}}$ to configured disjoint network $\acute{F}$:

1. A segment s_a in disjoint network $\acute{F}$ is labelled l, if in the $\mathcal{G}'_{\mathbb{ST}}$, the *source* node can still send some flow to the corresponding node of segment s_a either directly and/or via other node(s). See Figure 5.12.

2. A segment s_a in disjoint network $\acute{F}$ is labelled l', if in the $\mathcal{G}'_{\mathbb{ST}}$, some flow can be still sent from corresponding node of segment s_a to the *sink* node either directly and/or via other node(s). See Figure 5.13.

3. A segment s_a in disjoint network $\acute{F}$ is labelled opposite to the label assigned to its neighbouring node s_b, if in the $\mathcal{G}'_{\mathbb{ST}}$, neither *source* node can sent any flow to node s_a, nor any flow can be sent from node s_a to *sink* node and node s_b. See Figure 5.14.

4. If any two neighbouring nodes s_a and s_b in $\mathcal{G}'_{\mathbb{ST}}$ are assigned with identical label, their corresponding segments in $\acute{F}$ must be connected to each other at their respective junction.

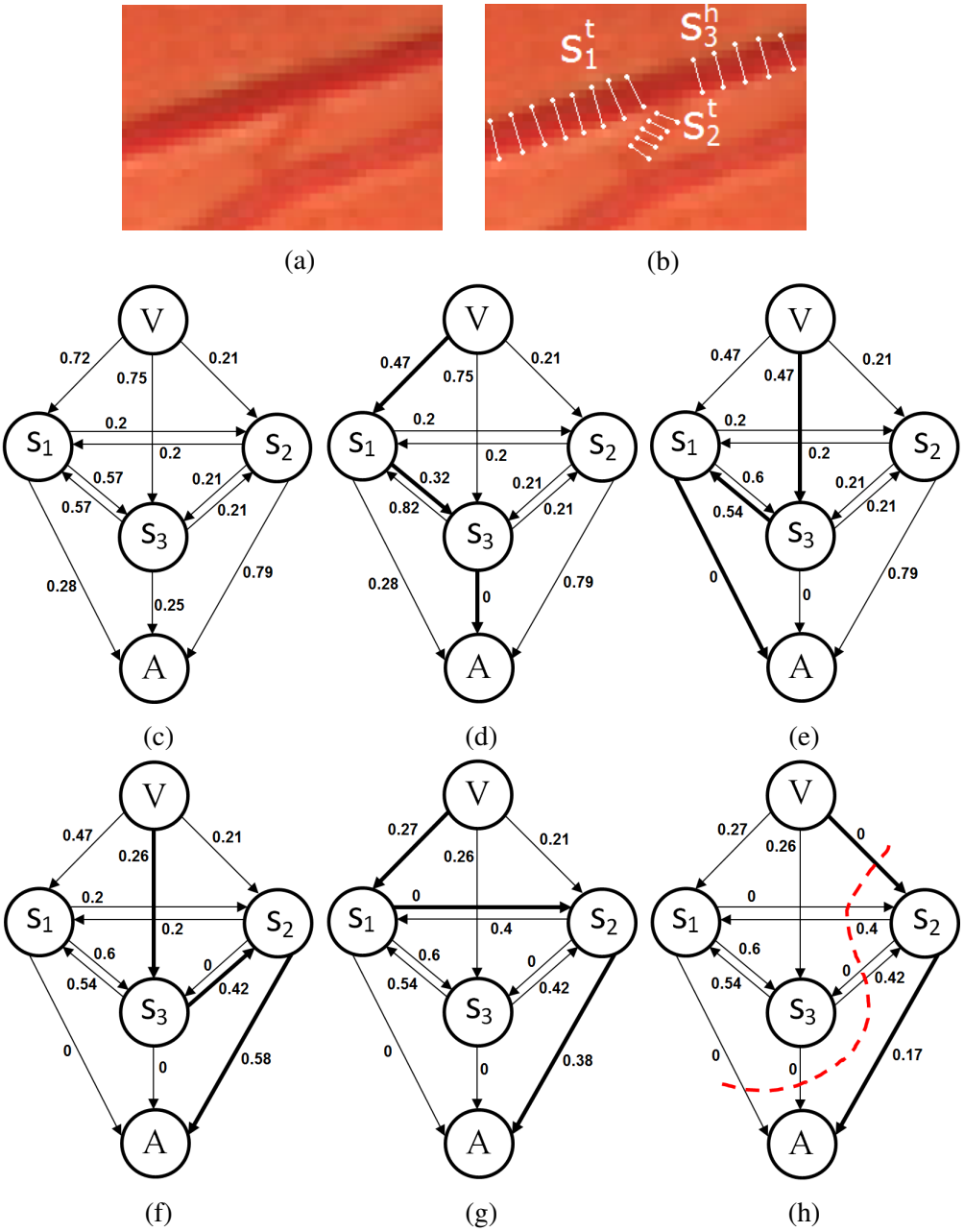

Fig. 5.10 The node V and A in $\mathbb{ST}$-graphs(c-h) denote vessel class vein and artery respectively. From (c)-(h), the step by step procedure of the Ford-Fulkerson algorithm is demonstrated. In (h), the minimum cut is found deducing that s_1 and s_3 are connected to each other and belong to vein class, whilst s_2 belongs to artery class and doesn't have connection with any of other segments.

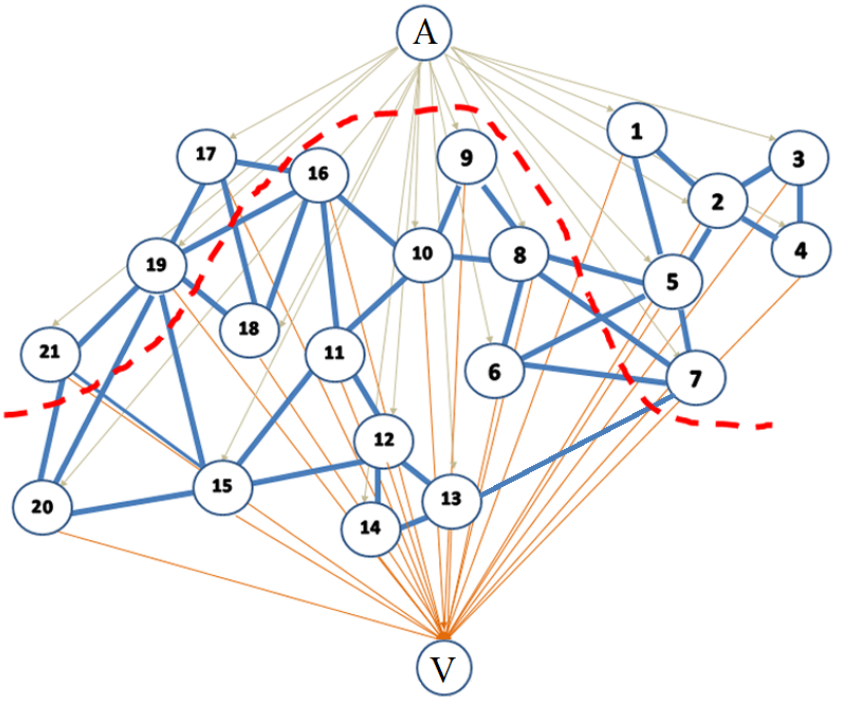

(a)

(b)

Fig. 5.11 (a) A global minimum cut is shown in the illustration. The *source* node A is denoting artery label whilst *sink* node V represent vein label. (b) According to the obtained cut in (a), the segments are labelled and connected. The red and blue colour is used to represent arteries and veins respectively.

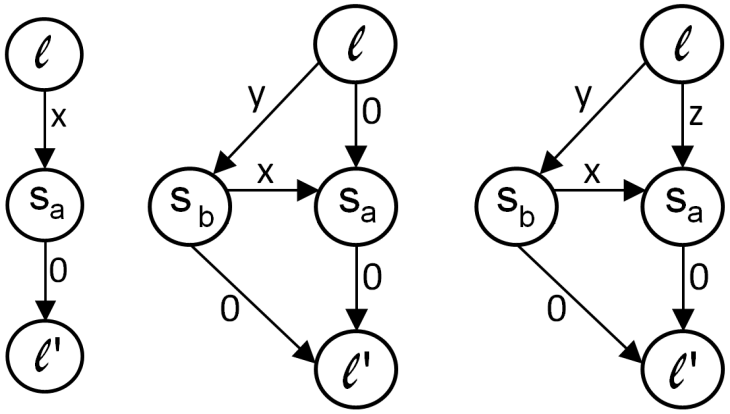

Fig. 5.12 In all cases (a)-(c), the *source* node l can send some flow to segment node s_a directly and/or indirectly via segment node s_b, and therefore s_a will be labelled as l.

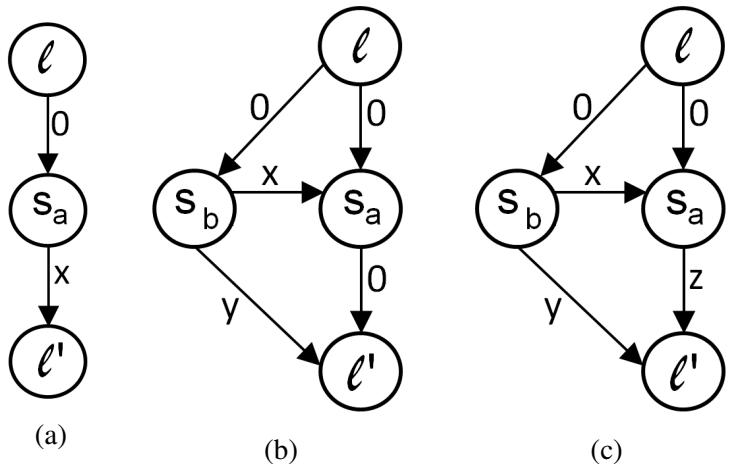

Fig. 5.13 In (a) and (c), the segment node s_a can send some flow to *sink* node $l^{'}$. Although in (b), s_a can't send any flow to $l^{'}$, however, segment node s_b can send flow to both $l^{'}$ and s_a. In all cases (a)-(c), segment node s_a will be labelled as $l^{'}$.

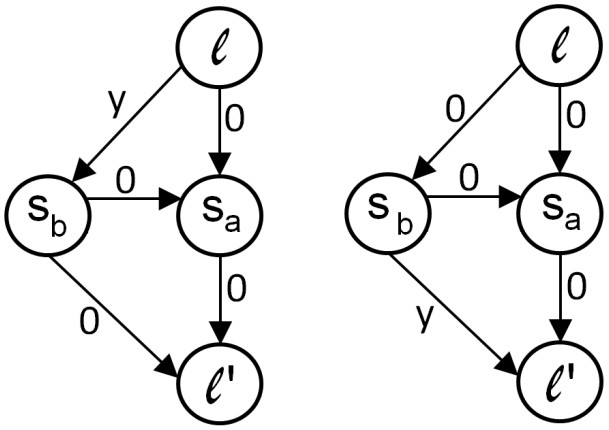

Fig. 5.14 In both cases (a) and (b), the segment node s_a can neither receive any flow from *source* node l (either directly or indirectly), nor can send any flow to *sink* node $l^{'}$. However in (a), the neighbouring node s_b can receive some flow from *source* node l but can't send any flow to segment node s_a, and therefore s_a will be labelled as $l^{'}$ and s_b will be labelled as l. Also in (b), the neighbouring node s_b can send some flow to *sink* node $l^{'}$ but can't send any flow to segment node s_a, and therefore s_a will be labelled as l and s_b will be labelled as $l^{'}$.

The result of applying the above rules is a configured disjoint network $\acute{F}$ consisting of one or multiple trees (T_i^l) each composed of connected segments having identical labels. Any segment, except overlapping segments, in configured disjoint network $\acute{F}$ can belong to only one tree at a time. Overlapping segments are treated as shared by opposite labelled trees and thus are not assigned by any label. It is important to note that any segment s_a associated to an overlapping segment s_b via a junction in F will be remain connected to s_b in $\acute{F}$; although, the system has specified the class and the tree the segment s_a belongs to. Referring to the example given in Figure 5.4, suppose the minimum cut on the graph classifies s_1, s_5 and s_7 as arteries of tree T_1^A , whilst s_2 and s_6 as veins of tree T_2^V , then segments s_1, s_2, s_3 are connected to each other at j_x, segments s_3, s_4, s_5 are connected to each other at j_y, whilst segments s_4, s_6, s_7 are connected to each other at j_z.

5.7.2 Connecting Extracted Trees

As aforementioned, a fundus image contains multiple disjoint networks, each consisting of one or more overlapping trees. The configuration of a disjoint network F_i is independent of the configuration of the rest of the disjoint networks. Therefore, for each MRF graph that corresponds to a unique disjoint network, a separate $\mathbb{ST}$-cut is obtained. A cut obtained on a disjoint network may result in a single tree T_x^l or multiple trees as $T_x^l, T_{x+1}^{l'}$, and so on. All segments belonging to a tree must belong to the same vessel class and are connected at respective junctions.

A post-processing step to obtain a global configuration to explore the opportunity to connect the identical class trees (such as T_x^l, T_y^l), extracted in a configured disjoint network, with each other. The possibility of connecting trees arises when a significantly long vessel segment is missing between spatially-close or adjacent junctions, and which results in multiple sub-trees of an identical class. Illustrations of missing segments that resulted in multiple extracted trees are given in Figure 5.15 (a)-(b). A disjoint network, configured in three or more than three trees, may support connection(s) between trees of identical class. The procedure for connecting identical class sub-trees in a configured disjoint network $\acute{F}$ requires correct identification of 1) the root segments of sub-trees T_x^l and T_y^l, and 2) the terminal junction of a specific sub-tree to which the root segment of another sub-tree can be connected to form a bridge, or the bridge junction of a specific sub-tree to which the root segment another sub-tree will be connected to form a bifurcation . The two tasks are explained below.

5.7.2.1 Tree Root Detection

A root segment s_a is one whose head end s_a^h is not connected to the end of any other segment, whilst the tail end s_a^t is either the parent of a bifurcation and is connected to the heads of two child segments, or is a terminal end and is not connected to any other segment. Thus, an extracted tree T_x^l in $\acute{F}$ has several unconnected ends–out of which, one is the head of the root segment, whereas all other ends are terminals.

Due to missing segment(s), a single true tree may be extracted as multiple sub-trees in $\acute{F}$, each having a unique root segment, as shown in Figure 5.15 (a)-(c). To construct a complete single tree in such case, the head end of the root segment s_a^h of one of the extracted sub-tree T_x^l of a certain class l is connected to the terminal end s_b^t of an appropriate segment of another tree T_y^l of the same class. As the roots of all trees emerge out of the ONH, the head end s_a^h of the root segment of a completely extracted tree is always closer to the ONH as compared to terminal end(s) s_a^t of the same tree. Using this condition, detecting root segments in extracted trees is straightforward. In addition to this, the width of a segment is a good indicator to identify the root segment of an extracted tree as the root segment is usually wider than the terminal segments.

To accurately identify the root segment out of a number of segments with their one end unconnected, the system utilises two features that include the Euclidian distance between the centre of the ONH and the unconnected ends of segments, and the widths of the segments with one end unconnected. Formally, given an extracted tree T_x^l consisting of segment set $S = \{s_1, s_2, s_3, \dots\}$, then $S^{'}$ is the set of segment ends belonging to those segments of S having at least one unconnected end, i.e.

$S^{'} = \{s_a^r | s_a \in S \wedge s_a^r isunconnected\}$. Let w_a is the mean width of segment s_a and $\ddot{d}_a^r$ is the Euclidian distance between the centre of ONH and r^{th} end of segment s_a. Then the probability that an unconnected end s_a^r of set $S^{'}$ is the head end of root segment, given all other unconnected end(s) s_b^r of set $S^{'}$, is as:

$$p(s_a^r \rightarrow root | S^{'}_{\setminus s_a^r}) = \frac{p(S^{'}_{\setminus s_a^r} | s_a^r \rightarrow root)}{p(S^{'}_{\setminus s_a^r} | s_a^r \rightarrow root) + p(S^{'}_{\setminus s_a^r} | s_a^r \rightarrow terminal)} \tag{5.12}$$

Whereas,

$$p(S^{'}_{\setminus s_a^r} | s_a^r \rightarrow root) = G_{w_a}.G_{\ddot{d}_a} \tag{5.13}$$

$$G_{w_a} = \begin{cases} 0.97 & \forall_b, w_a > w_b \\ 0.03 & \exists_b, w_a < w_b \end{cases} \tag{5.14}$$

and

$$G_{\ddot{d}_a} = \begin{cases} 0.95 & \forall_b, \ddot{d}_a < \ddot{d}_b \\ 0.05 & \exists_b, \ddot{d}_a > \ddot{d}_b \end{cases} \tag{5.15}$$

The parameters for both functions G_{w_a} and $G_{\ddot{d}_a}$ are obtained through the training process.

5.7.2.2 Connecting Trees

After identifying root and terminal(s) for each identical class tree T_x^l and T_y^l extracted in a configured disjoint network, the system connects the two trees (under certain conditions) to form a single tree T_z^l by means of joining the head end of the root segment of specific tree out of two trees (T_x^l, T_y^l) with the tail end of a specific terminal

of the tree opposite to the one whose root segment is to be connected.

Out of the two head ends s_a^r and s_i^r of root segments s_a and s_i belonging to two trees T_x^l and T_y^l respectively, the one which is farther from the centre of ONH is connected to a terminal of the other tree which is selected from a closed-neighbourhood of the root segment to which the terminal is to be connected. Assume the root head s_a^r of tree T_x^l is found farther from the centre of the ONH, then choosing the correct terminal s_k^r of tree T_y^l in the closed-neighbourhood of s_a^r, to which s_a^r is possibly be connected, the procedure analyses the angle $\vartheta_{a,k}$ between the root segment s_a of tree T_x^l and each of the terminal segment s_k of tree T_y^l. The $\vartheta_{a,k}$ is the angle, calculated by considering the two direction vectors-one for s_a and the other for s_k. The direction vector of a segment s_a or s_k can be calculated by considering the central points of its connected and unconnected ends, as shown in Figure 5.15 (b). A maximal angle indicates high chances of missing segment between the two trees. Thus, s_a of tree T_x^l is connected to any terminal s_k of tree T_y^l, if $\vartheta_{a,k}$ is larger than 160 degree. The value 160 is obtained during the training process. In this process, several completely extracted trees were selected; in each of these, a segment is randomly chosen and removed which resulted in broken trees. The $\vartheta_{a,k}$ is then calculated for true connections between the sub-trees. In the training examples, the minimum and maximum value for $\vartheta_{a,k}^{x,y}$ is found 145 and 173 degree respectively.

In case the dis-connected trees are the result of absence of a significantly long part of the child segment of a parent at a bifurcation, as shown in Figure 5.15 (c), then the head end s_a^r of tree T_x^l is connected to the segment end s_k which is the part of a bridge occurred at an adjacent or spatially-closed junction of s_a^r.

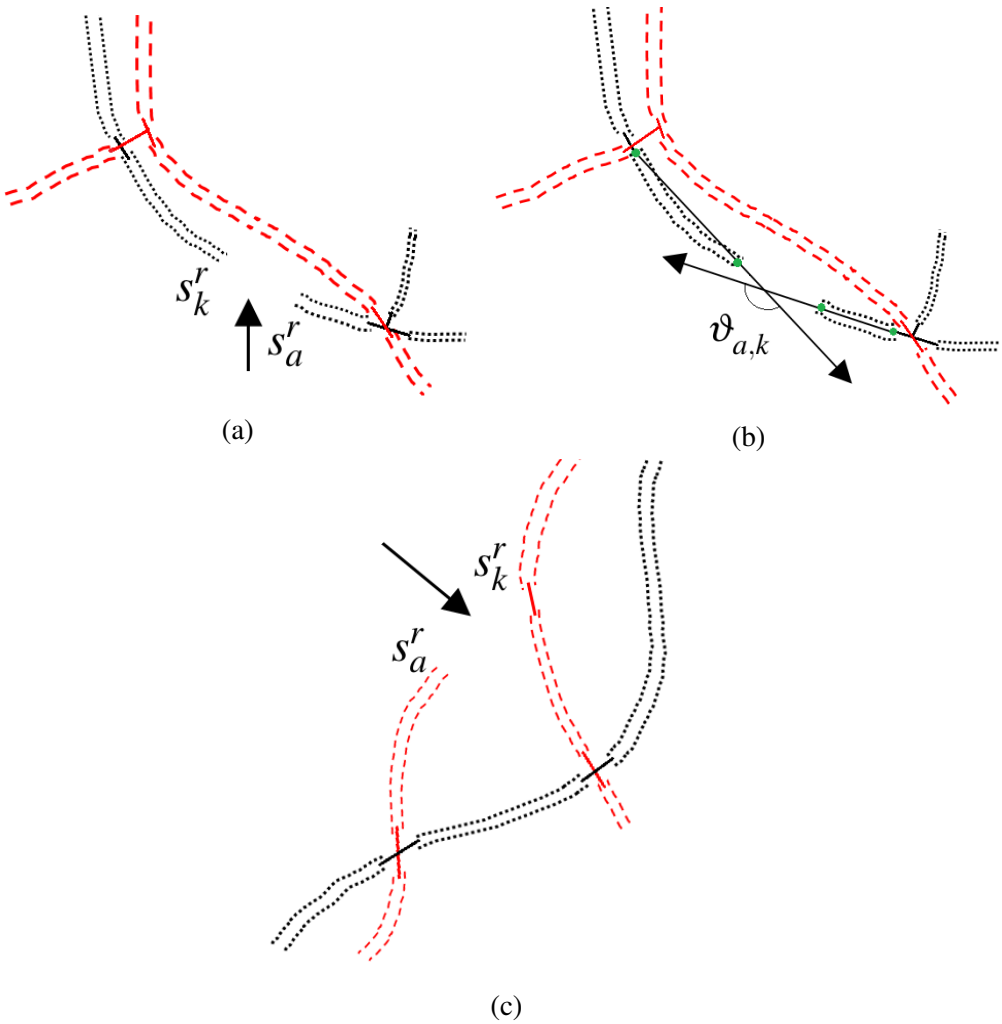

Fig. 5.15 a) A dotted-style vessel segment is missing as indicated by the arrow. b) The direction vectors of two segments are forming angle. c) A dashed-style vessel segment is missing at a bifurcation as indicated by the arrow.

5.8 Conclusion

This chapter introduces a novel procedure for efficiently extracting arterial and venous trees from disconnected and unlabelled vessel segments in fundus images. The procedure is carried out in a pipeline of several essential tasks. The key contribution of this chapter is the transformation of networks of disconnected segments into probability-based Markov Random Field dependency graphs. The transformation consists of representing the association of segments and junctions into 2-D graphs, and estimating unary and pairwise potentials as weights for graph edges. The transformation supports the application of any appropriate inference method for binary labelling by interpreting the graph as a flow network for energy minimization. A minimum $\mathbb{ST}$-cut is obtained over the formulated graphs, implemented by running the Ford-Fulkerson algorithm. After obtaining the global minimum cut, and performing back-translation of global configuration to labelled/connected trees, the extracted trees of identical class are joined with each other in order to extract complete trees of arteries and veins.

In addition, prior to transforming segments network into graphs, an efficient method is used to identify unique disjoint networks.

Chapter 6

Experiments, Evaluation and Discussion

6.1 Introduction

This chapter provides performance details of the key stages of the proposed system. The evaluation is performed using two segment sets $DSJS_1$ and $DSJS_2$ obtained using segmentation techniques by (Al-Diri et al., 2009) and (Bankhead et al., 2012) respectively for the DRIVE test images.

Section 6.3 provides the specification and the expected outcome of each major task. This section also defines criteria for assessing the performance of the system, followed by an experimental evaluation of each model including junction identification, local configuration, and global configuration for AV tree extraction. In addition, complications and causes of failure in each task are discussed.

Section 6.4 provides a detailed discussion of the net performance of the system in terms of a robustness analysis, obtained results, and novel improvements compared to the state of the art solutions. A critical analysis of several elements,

including the sensitivity of represented parameters, and system limitations with possible suggestions for improvement, is also presented. Section 6.5 concludes the chapter.

6.2 Pre-processing

The RGB versions of all images, used for training and testing purposes, were first enhanced to improve colour contrast. The Multi-scale Retinex technique (Jobson et al., 1997) is used for image enhancement; see Figure **??**.

In the original $DSJS_1$ set the boundary points of a few segments overlapped, where there are overlapping vessels. In such a case, a segment is randomly selected out of the two overlapping segments, and removed as the system doesn't expect pre-identified overlaps.

In the original $DSJS_2$ set all segments are isolated and disconnected at junctions. In a few cases the end points of two or more segments at a junction were very close; in such an extreme case, the system reduces the length of these segments by removing the boundary pixels of up to three end profiles.

6.3 Evaluation

6.3.1 Scope of the Local and Global Configuration

For an unambiguous assessment, it is of high importance to understand the difference between the local and global configuration with regard to their expected outcome. These differences are elaborated in the form of given points.

(a)

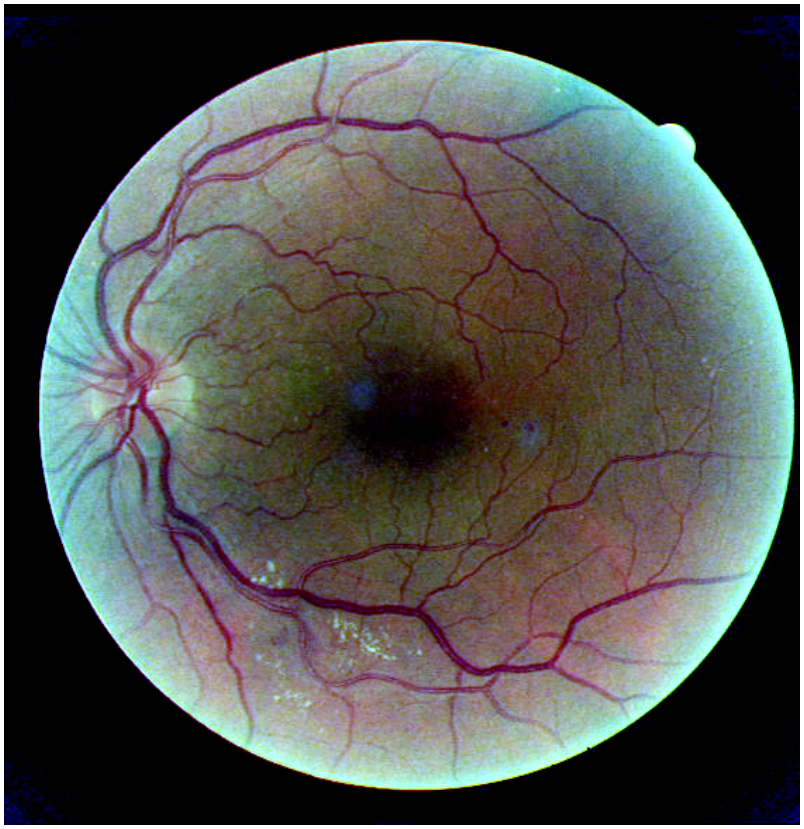

(b)

Fig. 6.1 (a) An unprocessed RGB image taken from test images of DRIVE. (b) An equivalent enhanced image.

1. The local configuration of a junction refers to connecting the segment ends by searching through the possible configurations locally at that junction while ignoring the configurations at the rest of the junctions; for instance finding MAP configuration at each junction. The global configuration, on the other hand, considers configurations of all junctions of a disjoint network simultaneously.

2. The global configuration of a disjoint network may or may not correspond to the global MAP solution, but guarantees a globally-optimal configuration.

3. Using the MAP configuration at each junction locally doesn't guarantee building trees, as the local MAP configurations of junctions might have conflicts with each other (i.e. graph cycles), whereas global configuration reduces the chances of cycles to a great extent. A possible example of such conflict is when ends of any two different segments are connected at a junction j_k, implying that they belong to an identical trees; while the other ends of same segments cross each other at an adjacent junction j_{k+1}, contradict the configuration at j_k.

4. Local configuration resolves only those overlaps which appear as a single segment. Global configuration is able to resolve overlaps where the vessels are broken into multiple consecutive segments which require processing configurations of several junctions simultaneously.

6.3.2 Evaluation criteria

The success rate of each major task is calculated based on the following criteria.

- *Junction Identification* The junction identification model is assessed by analysing the associations of segments with each other according to following rules:

1. A success is counted when an end of a true segment is correctly associated with its junction.
2. A failure is counted when an end of a true segment is not associated with any junction. This excludes terminal and root ends.
3. A failure is counted when an end of a true segment is associated with a junction other than the junction it truly belongs to in the ground truth.
4. A failure is counted when both ends of a segment are associated to the same junction.
5. The association of a false segment to a specific junction, containing the end of at least one true segment, is neither counted as success nor failure, as later, the extracted trees may yield a configuration that does not include the false segment at that junction.
6. Two mistakes are counted whenever the system unifies two spatially-close junctions into a single junction.

- *Local Configuration*

1. The system counts one success per correctly configured joint (for instance, three segment ends forming a true bifurcation; or two segment ends forming a true bridge). This also includes cases when a segment is missing from the dataset at a joint. For instance, if a true bifurcation is configured as a bridge, when the third segment is missing in the dataset, is also counted a success.
2. A partially configured joint is counted as one failure. For instance, if a true bifurcation is configured as a bridge and a terminal.

3. A junction may consists of multiple joints, and thus may result in multiple successes and/or multiple failures.

4. Local configuration is responsible for resolving overlaps, each of which appears as a single segment. Global configuration resolves overlaps that consist of segments broken into multiple consecutive segments requiring configuration of several junctions simultaneously.

5. The configuration of a joint is counted as a failure if the joint consists of one or multiple false segment end(s).

- *Segment Classification* The system counts one success per correctly classified segment; one failure for incorrect classification. When the corresponding segment in the ground truth set is unclassified, it is ignored.

- *Global Configuration* The system counts one failure whenever an extracted tree has a configuration at a junction that conflicts with the configuration of other junctions.

- *Ground Truth Data* The outcome of each task is compared with the established ground truth dataset (CVD) mentioned in Chapter 4. The test images of the CVD set are provided in Appendix A of the thesis.

6.3.3 Junction Identification Model

The junction identification model is evaluated on test sets of $DSJS_1$ and $DSJS_2$. The system proved highly efficient, correctly identifying junctions in a highly discontinuous and complex vascular network. Using the criteria above, the system correctly identified 98.5% and 98.1% junctions in the $DSJS_1$ and $DSJS_2$ test sets respectively.

The full statistics are given in Table 6.1.

The system initially used Υ_{MIN} =7, which resulted in a number of Condition 1 and Condition 2 cases. As explained in Chapter 4, Υ is the length of the vector using which the segment end region (SER) is defined; Condition 1 refers to situation when a segment end is not associated to any junction; and Condition 2 arises when both ends of a segment becomes the part of the same junction. The system efficiently resolved these cases by dynamically updating the Υ value, resolving cases such as segment ends with no association to any junction, over-large junctions, and junctions with incorrect associations. Setting $\Upsilon_{MIN} < 7$ has little effect on the system outcome other than a small increase in the computational cost. However, the Υ_{MAX} value is fairly sensitive; a very high value may result in huge numbers of segment ends assigned to junction. The primary cause of failure the excessive distance of segment ends from the true junction locations, resulting in failure to assign the segment end to the junction. However, the tree-joining step typically resolves this discontinuity later.

The percentage-wise mean cardinalities of identified junctions in the $DSJS_1$ test images are: 42.9% with cardinality one, 26.6% with cardinality two, 22.9% with cardinality three, 6.1% with cardinality four, and 1.3% with cardinality five. For $DSJS_2$, the statistics are: 56.1% with cardinality one, 12% with cardinality two, 25.7% with cardinality three, 5.6% with cardinality four, and 0.4% with cardinality five. The image-wise identified junctions with their cardinalities are given in Table 6.2. As shown in the table, the cardinality of any identified junction never exceeded 5; which was also the highest cardinality of the junctions in the ground truth data. It may be worth noting that in principle higher cardinalities are possible (e.g. two

$DSJS_1$	
Total number of segment ends to be associated	7610
Total number of segment ends correctly associated to junctions	7501
Total number of segment ends remained un-associated	97
Total number of segment ends wrongly associated to junctions	12
Success Rate	98.5 %
$DSJS_2$	
Total number of segment ends to be associated	4264
Total number of segment ends correctly associated to junctions	4185
Total number of segment ends remained un-associated	69
Total number of segment ends wrongly associated to junctions	10
Success Rate	98.1%

Table 6.1 Performance of the Junction Identification Model

coincident bifurcations), although this did not occur in $DSJS_1$ or $DSJS_2$, so is closely none.

A junction with significantly higher cardinality is caused by either associating both ends of a segment to the same junction and/or by merging multiple spatially-close junctions into a single junction. Typically, the available connectivity techniques are not trained to address the former case (if it arises) by disassociating one of the ends of the segment from the junction. The latter case presents two problems. First, due to the exponential increase in the number of possible configurations, finding the MAP configuration becomes computationally expensive. For instance, if two spatially-close junctions, each with cardinality four, are merged into a single junction with cardinality 8, then would be of 4364 configurations. Secondly, the performance of any local configuration system decreases with increasing cardinality, as geometry of possible joints becomes finer grained and therefore the chances of mistakes is high.

Image Number	Segment Set	Cardinality of Junctions					
		1	2	3	4	5	Total
1	$DSJS_1$	102	65	53	16	1	237
2	$DSJS_1$	69	60	62	10	3	204
3	$DSJS_1$	90	68	47	15	5	225
4	$DSJS_1$	59	32	26	6	1	124
5	$DSJS_1$	96	48	42	10	4	200
6	$DSJS_1$	76	33	31	12	1	153
7	$DSJS_1$	126	66	56	13	2	263
8	$DSJS_1$	100	37	28	6	2	173
9	$DSJS_1$	66	22	35	6	1	130
10	$DSJS_1$	82	63	30	10	4	189
11	$DSJS_1$	93	53	50	20	3	219
12	$DSJS_1$	96	58	57	9	3	223
13	$DSJS_1$	79	54	50	23	3	209
14	$DSJS_1$	97	60	62	9	5	233
15	$DSJS_1$	50	82	55	11	1	199
16	$DSJS_1$	104	53	55	15	3	230
17	$DSJS_1$	72	42	36	5	2	157
18	$DSJS_1$	86	52	40	13	0	191
19	$DSJS_1$	82	49	45	12	3	191
20	$DSJS_1$	73	49	36	13	3	174
1	$DSJS_2$	82	21	33	6	1	143
2	$DSJS_2$	64	13	32	9	0	118
3	$DSJS_2$	83	19	25	3	0	130
4	$DSJS_2$	56	8	24	7	0	95
5	$DSJS_2$	64	14	30	7	0	115
6	$DSJS_2$	51	8	22	10	1	92
7	$DSJS_2$	72	12	36	4	0	124
8	$DSJS_2$	24	19	32	11	0	86
9	$DSJS_2$	64	8	24	5	0	101
10	$DSJS_2$	70	15	22	6	0	113
11	$DSJS_2$	75	22	35	6	0	138
12	$DSJS_2$	68	19	41	5	1	134
13	$DSJS_2$	75	10	42	11	1	139
14	$DSJS_2$	61	8	32	7	1	109
15	$DSJS_2$	55	14	31	5	0	105
16	$DSJS_2$	54	21	33	6	1	115
17	$DSJS_2$	75	13	24	4	1	117
18	$DSJS_2$	73	15	29	5	2	124
19	$DSJS_2$	80	10	32	5	2	129
20	$DSJS_2$	66	12	22	11	0	111

Table 6.2 Junctions with their associated number of segment ends.

6.3.4 Local Configuration Model

For every possible configuration at each identified junction, the local configuration model estimates a probability value. An experiment is performed to analyse the efficiency of the local configuration model by choosing the MAP configuration at each junction.

The experiments are performed on test sets of $DSJS_1$ and $DSJS_2$. The model produced excellent results on both $DSJS_1$ and $DSJS_2$ sets, with the success rates 94.3% and 95.3% respectively. Detailed statistics are provided in Table 6.3. From the statistics given in this table, it is clear that the number of bridges in $DSJS_1$ is nearly three times the number of bridges found in $DSJS_2$. This shows that $DSJS_1$ has a higher disconnectivity rate than of $DSJS_2$. Also, the number of bifurcations in $DSJS_1$ is approximately 1.5 times higher than number of bifurcations found in $DSJS_2$. This is the evidence that quite a few segments for the ending parts of vessel trees are missing in $DSJS_2$.

The system was able to identify 31 and 22 overlapping segments out of total 33 and 23 in $DSJS_1$ and $DSJS_2$-obtaining overall 94.2% and 95.6% sensitivity; and 99.7% and 99.1% specificity respectively. In addition, 99.1% and 98.5% of true trifurcations were detected respectively in $DSJS_1$ and $DSJS_2$. The removal of segments inside the optic nerve head eliminated 0.7% of the joints. These results are compared with the result of technique introduced in (Al-Diri et al., 2010) as they have used $DSJS_1$ to test their system. The success rates they achieved are 76%, 71%, and 59% for bridges, bifurcations and terminals respectively. Whereas, as given in Table 6.3, the success rates we achieved are 94.07%, 93%, and 96.1% respectively for bridges, bifurcations and terminals respectively. An overall improvement of 22.3% is achieved by our system.

Joints	$DSJS_1$			$DSJS_2$		
	Total	Configured	Success	Total	Configured	Success
Bridges	1537	1446	94.07%	554	509	91.8 %
Bifurcations	899	836	93%	601	550	91.5 %
Terminals Roots	1653	1589	96.1%	1312	1293	98.5 %

Table 6.3 Summarized results of the local configuration model.

Segmentation errors and false segments are the main sources of failure cases. A third cause of failure in a few cases of local configuration inference is the unavailability of sufficient training data particularly for cases when the positions of segment ends are not regular. For such cases, the parameters for the prior probability $p(C_q^k)$ are obtained from a very limited number of examples. If a sufficiently large training data is available, the problem may be mitigated by updating prior for such cases.

By empirical observations, the features used to estimate the joint likelihood functions, suggest that the angle and orientation are the most important, followed by width, while the intensity has the least effect on the overall results. The configuration results are shown on a sample test images of DRIVE for $DSJS_1$ are in Appendix B of the thesis.

6.3.5 AV tree Extraction Model

We tested the global configuration system on test images of $DSJS_1$ and $DSJS_2$. The system successfully achieved global configurations by resolving conflicts in local configurations with improved results from 94.3% to 95.7% in $DSJS_1$ and from 95.6% to 96.2% in $DSJS_2$. In addition, in most of the cases, the obtained global configurations correspond to the MAP estimations. The system was able to accurately classify 94.7% and 93.4% of the total segments in test images of $DSJS_1$ and $DSJS_2$

respectively. The majority of failure cases in both sets results from segments which are isolated (i.e. not associated with the junctions of extracted trees), or where the corresponding vessels in manually labelled set are remained unclassified.

The trees are extracted on test images of $DSJS_1$ and $DSJS_2$. A sample of extracted trees in $DSJS_1$ is provided in Appendix C.

Before comparison, it is important to take the key aspects of the alternative techniques into account. For instance, the technique (Dashtbozorg et al., 2014) provides solution for classifying only the major vessel segments having average width above 3 pixels. Similarly, the work produced in (Lau et al., 2013) classifies only the major vessel segments in a predefined area. Thus, these techniques are not compatible with our AV tree extraction model.

The technique in (Lin et al., 2012) performs global configuration of vessel segments but does not classify them, and thus extracts binary trees only. The authors of (Lin et al., 2012) technique tested their system using test images DRIVE with the success rates obtained as follows: 76% bifurcations, 83% bridges, 88% terminals, and 83% overall success. We achieved improved performance by 19.2% for bifurcations, 11.7% for bridges, 8.1% for terminals, and 12.06 % overall.

We compared the result of AV tree extraction model with two previous techniques developed for extracting AV trees. The two techniques (Joshi et al., 2014) and (Hu et al., 2015) perform AV trees extraction by considering both major and minor segments. Both techniques consider segments of the whole image, however, in (Hu et al., 2015), the segments with average width below 1.5 pixels are ignored.

Techniques	A	B	C	D	E	F	G
(Al-Diri et al., 2010)	Yes	Yes	72.1%	No	No	NA	NA
(Lin et al., 2012)	Yes	Yes	88.7%	Yes	No	NA	NA
(Hu et al., 2015)	Yes	Yes	NA	Yes	Yes	No	86.1%
(Joshi et al., 2014)	No	Yes	NA	Yes	Yes	No	91.4%
Proposed Method	Yes	Yes	95%	Yes	Yes	Yes	95.7%

Table 6.4 Comparison of techniques: A) Performs local configuration of segments, B) Used DRIVE dataset, C) Result of local configuration, D) Performs global configuration of segments, E) Performs classification of segments, F) Performs classification and configuration as complimentary process, G) Result of AV tree extraction. N/A= Not Applicable.

The mean results produced by these techniques are 91.4% and 86.1% respectively. In terms of results, we have obtained better results than any of these techniques. A summary of the comparison of the results produced by the discussed techniques are given in Table 6.4.

Our system has two advantages over the alternative techniques. The first is that the proposed AV tree extraction model addresses two problems (classification and connectivity) by integrating them into a single binary labelling problem. The synergy of classification and configuration knowledge to improves performance. In contrast, all the above discussed techniques resolve the two tasks separately by firstly extracting the binary skeletons of vessel trees, followed by classifying them into one of the vessel classes. In addition, our classification model not only exploits the crossing of vessels as a potential classification feature, but also considers the spatially-close (parallel running) vessels as a classification indicator.

The second factor is that previous techniques mostly follow heuristic (greedy) approaches to get the optimal configuration. For instance, at a junction of three segment

ends, the technique in (Hu et al., 2015) considers only four potential configurations, whilst our local configuration model considers seven configurations in total. This raises an issue of over-fitting the model on the specific data. In contrast, our model never ignores any possible configuration at junctions. In particular, the inference models uses unary and pairwise potentials, and integrates the probabilities of the entire search space. This makes the model highly reliable for previously unseen data with unique vessel patterns.

In literature, the common approach to evaluate the proposed systems is to use the single partition of DRIVE dataset, i.e. by taking 20 images for training and 20 images for testing. However, we also performed a cross validation (rotation estimation) test to assess the proposed model as how the results of a statistical analysis will generalize to an independent data set.

In this experiment, the entire dataset (consisting of training and testing images) is considered as single dataset of 40 images. The k-fold cross validation technique is used by first randomly partitioning the original dataset into equal subsamples for both $DSJS_1$ and $DSJS_2$. The k value is taken 10, resulting in total 10 subsamples, each of size 4 images. Followed by training the $k-1$ subsamples, and testing system on the remaining subsample. The experiment is repeated 10 times by so each subsample is used for testing exactly once and 9 times for training.

The randomly generated subsamples with image numbers are provided in Table 6.5.

The training of the $k-1$ subsamples is conducted using exactly the same procedure utilised for training the single partition of original dataset. The results obtained

in all ten repetitions are shown in Figure 6.2.

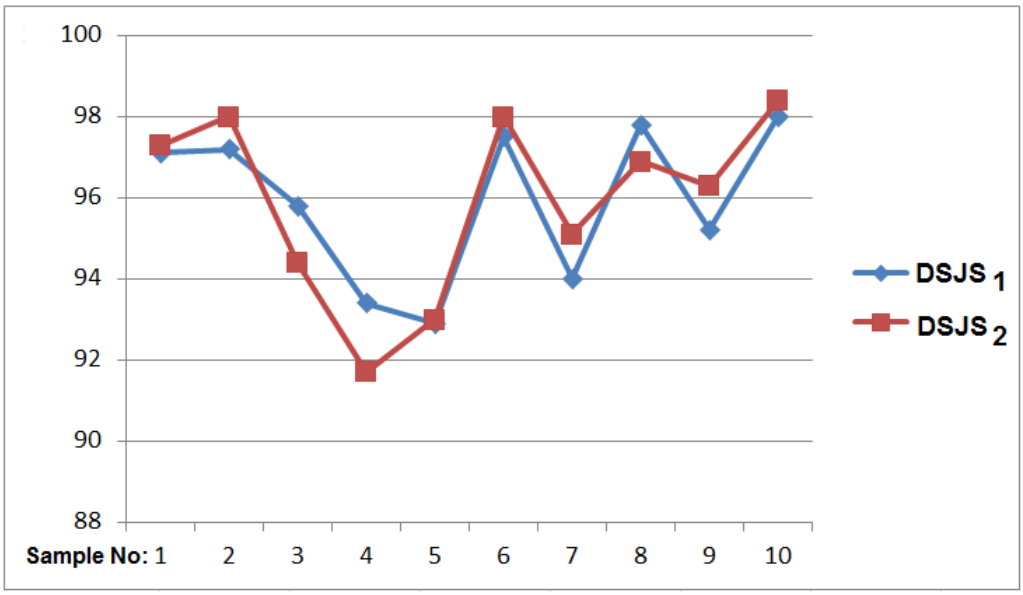

Fig. 6.2 The success rate on subsamples of $DSJS_1$ and $DSJS_2$.

The average results obtained from this experiment (95.89% for $DSJS_1$ and 95.91% for $DSJS_2$) are slightly higher than the result obtained by using single partition of dataset. This concludes that by increasing the training data, a better accuracy can be achieved. Though the representative parameters of feature distributions obtained from training data in each repetition during the experiment were slightly different from each other; however, when taken as an average, the difference was near to none.

Subsample Number	Image Numbers
Subsample 1	21, 13, 14, 29
Subsample 2	31, 12, 4, 15
Subsample 3	35, 32, 6, 10
Subsample 4	5, 9, 18, 25
Subsample 5	11, 26, 3, 38
Subsample 6	1, 7, 36, 39
Subsample 7	8, 34, 16, 22
Subsample 8	23, 24, 33, 2
Subsample 9	19, 20, 27, 28
Subsample 10	30, 17, 37, 40

Table 6.5 Random Distribution of 40 Images of DRIVE into Subsamples.

6.4 Discussion

6.4.1 System Performance

The global configuration model is able to extract highly probable AV trees by classifying segments and finding non-conflicting local configurations simultaneously. Integrating classification and connectivity probabilities into a graphical model produces the complementary strength of the proposed approach. The overall system remained stable throughout the implementation of each major stage. The algorithm for the AV trees extraction model is run using Matlab 2015b version on Intel Core i6; and which took less than one minute to process on average. The prebuilt functions of Matlab made the algorithm run significantly faster with minimum use of space. The number of segments per image is not usually high (i.e. 150 to 350 on average), the Ford-Fulkerson algorithm didn't take long to get the optimal graph cut. However, by increasing the segment ends at junctions might result in big search space and thus computational efficiency will be affected.

To the best of our knowledge, we are the first to develop an AV tree extraction model that integrates the connectivity and classification tasks into a single binary labelling problem and solves this with a single technique. Modelling the joint probability of connectivity and classification in the MRF graph, and inferring using the $\mathbb{ST}$-cut, is proves to be an appropriate solution for the current problem. The system typically converges to high performance global configurations that usually correspond to MAP solutions. Moreover, the minimum cut efficiently utilises the connectivity priors to classify minor segments whose unary potentials are equally likely for any class. Furthermore, the experiments show that by introducing the spatial feature ζ, the efficiency of the naïve Bayes classifier has significantly improved.

It is common practice for authors to train and evaluate their connectivity techniques by utilizing the segments that are obtained using their own segmentation methods. The performance of these techniques may be influenced by the complexity level or discontinuity characteristics of their segmentation algorithms, and/or the predefined assumptions. In addition, the unavailability of their segmentation techniques or their segments to the research community makes difficult to judge the overall progress in the state of the art. Moreover, using different segmentation techniques for the same image set produce different results and thus the complexity of discontinuity varies. This motivated us to evaluate our system, and produced results, using the segments obtained from two different techniques for the same dataset. In case of $DSJS_2$, in particular, not only the segments but also its technique is available online for free and has been used by a number of researchers.

The results of the experiments demonstrate that the system is able to efficiently extract AV trees from a range of patterns of incompletely-segmented vasculatures.

However, a significant increase in the number of false and/or missing segments can degrade the overall performance. Typically, the available connectivity techniques don't integrate the task of distinguishing true/false segments; rather separate techniques are utilised to remove false segments. For the future work, the proposed local configuration model can be trained for extended configurations that may be partially or composed of false segments. In such case, the formulated MRF can also be extended to multivariable labelling problem with three classes as arterial segment, venous segment, and false segment. For inference over such MRFs, there are various algorithms available that work by reducing the problem to a sequence of minimization sub-problems with binary variables, such as (Boykov et al., 2001) and (Veksler, 1999).

The only step in the proposed technique that requires user intervention is the manual identification of the centre of optic nerve head. This can be automatically achieved by using any sophisticated OD localization technique such as (Lowell et al., 2004a), (Mohammed et al., 2014), and (Qureshi et al., 2012).

6.5 Conclusion

We assessed the major stages of the proposed AV extraction model using precise evaluation criteria. The performance is analysed by testing the system on two different segmentations, each obtained for the DRIVE test images. The two sets $DSJS_1$ and $DSJS_2$ demonstrate unique and complex patterns of disconnected vasculatures. The elementary models including junction identification, local configuration, global configuration and trees joining, produced best results on both $DSJS_1$ and $DSJS_2$ sets.

The reference image set is used for comparison at all the stages. The performance is also compared with the results produced by published alternative techniques. The proposed system exceeds the documented performance of state of the art techniques. We also discussed the limitations of the system with possible suggestions to address these.

Chapter 7

Conclusion and Future Work

7.1 Introduction

The automated extraction of retinal arterial and venous trees from disjoint networks of vessel segments in fundus images is a prerequisite to examine the correlation of global features of retinal vasculature with a number of abnormalities that arise in the retina. In addition, it supports the analysis of physiology and hemodynamic of blood flow in retinal vessel trees.

Automated AV trees extraction in retinal images is relatively new area with very few published techniques. In this thesis, a novel probabilistic graph based methodology is presented which requires zero user-intervention and is able to extract AV trees from a segmented vasculature disconnected at some or all junctions. The system efficiently locates all junction points, locally connects the segment ends, classifies the vessel segments, and extract AV trees by finding a highly optimal global configuration of the segment network.

The project has developed a robust graph based extraction model that can resolve discontinuities occurring in the segmentation of images containing overlapping tree-like structures. The methodology is optimized to resolve discontinuity in retinal vascular trees; however, it could be adopted for a number of other trees and track like structures.

7.2 Novelty of Science

Based on a sequence of processing steps, an efficient extraction method is developed that is comprehensive and far more robust than the previously published techniques. A probabilistic graphical model is developed for the accurate extraction of arterial and venous trees from a network of disconnected retinal vessel segments in fundus images. The contributions are presented below.

7.2.1 Junction Identification Model

The identification of junction locations is a critical task as the outcome of the rest of following phases depends highly on the accuracy of identified junction points. A fully automated technique that works by dynamically growing segment ends regions (SERs), is developed for identifying junction points. The SERs created utilise direction vectors and angles at segment ends, and through a supervised probabilistic manner the overlaps of SERs of several segment ends are identified as junction points. The approach assures junction properties such as:

- Both ends of a segment can't be assigned to the same junction.
- A junction never exceeds a specific number of associated segment ends.

Unlike alternative models that result in significantly high number of associated segment ends, the proposed model obtains excellent results by identifying smaller junctions with restricted numbers of segment ends.

7.2.2 Probabilistic Model for Local Configuration

A new supervised Bayesian probability model is developed for correctly connecting the vessel segment ends at junctions. The probabilistic framework effectively utilises the priors and conditional likelihoods of local configurations in two passes of Bayesian inference and estimates configuration posteriors. The likelihood functions are equipped with the estimated parameters of Gaussian distributions of a number of segment joints features. This model is capable of estimating the MAP (Maximum A Posteriori) configuration on any number of associated segments provided the configuration priors are obtained through a sufficiently large dataset. In addition, an extension of this model is might be possible for junctions with a mixture of associated true and non-true segments using the similar approach of enumerating mutually exclusive and collectively exhaustive configurations and choosing the MAP estimation. The developed model is able to correctly identify segment joints including bifurcations (parent-children relationship), bridges, overlaps, and mixture of these joints. This model is evaluated independently of other parts of AV trees methodology with excellent results produced.

7.2.3 Vessels Classification

Due to an increase in research interest in examining the functional and structural behaviour of retinal arteries and veins at both local (i.e. at junctions or between consecutive junctions) and global level (i.e. trees level), a Naïve Bayes classifier is

trained for soft labelling of retinal vessel segments. This model estimates the posterior class probability of segments using geometrical, colour, and spatial properties. To the best of our knowledge, it is the first time spatial information of vessels is thus been used to improve the performance of vessel classification.

7.2.4 Arterial and Venous Trees Extraction

A novel approach is developed to translate the disjoint network of segments network into a dependency graph Markov Random Field (MRF). The formulated MRF expresses joint probability distribution of segments' classification and connectivity. The translation converts the AV tree extraction problem into an energy minimization problem for binary labelling.

An MRF is formulated and an $\mathbb{ST}$-graph cut is used to derive the global optimal labelling and connectivity simultaneously. The $\mathbb{ST}$-graph cut is obtained by implementing Ford-Fulkerson algorithm. The minimum cut yields sub-graphs each representing a connected tree of arteries or veins, through a process of back-translation of the graph into vessel trees. The extracted sub-trees of same class are considered for re-joining if separated because of missing segments. The system is highly efficient and produces excellent results.

7.2.5 Other Contributions

This project introduces a vessels classified image set for DRIVE images. The vessels were manually classified into arteries and veins by retinal imaging experts and an ophthalmologist. This publically available dataset provides an opportunity to the future researchers to evaluate alternative labelling algorithms.

This thesis also provides an insight into the structural behaviour of the retinal vasculature through statistical analysis of a number of retinal vascular features. The findings can be utilised to examine the correlation of vascular structures and abnormalities that arise in retina. In conjunction with physiological features, the obtained findings would be useful for studying global features of vessel trees.

7.3 Future Work

7.3.1 Global Features of Retinal Vasculature

The fractal properties of retinal vascular trees provide insight into global features of the retinal vasculature. A number of medical studies (Stošić and Stošić, 2006) reported direct correlation of vascular fractal features to several pathologies. As both choroid and retinal vessels originate from same ophthalmic artery, examining the global features of retinal arterial and venous trees may also provide understanding and changes to vascular system at outer retina. This may provide indirect relation of retinal vascular changes to complications at other retinal layers including Age-related Macular Degeneration (AMD) which is a leading cause to loss of central vision. In addition, extraction of AV trees provides global view of vascular system which is an opportunity to examine the physiology and hemodynamic of blood flow in retinal vessels.

Moreover, the AVR feature is being frequently used in clinical diagnosis, obtaining AVR (Artery-to-Vein Ratio) is an immediate application of AV trees extraction. This thesis will also help researchers to examine the vascular behaviour near the

optic nerve head and investigating possible impact on vascular trees of glaucomatous diseases.

7.3.2 Extended MRF

Detecting and removing false segments is out of the scope of this thesis, and thus all the nodes of formulated MRF are treated as corresponding to true segments. A potential research direction is to extend the formulated MRF from binary to multiclass labelling problem by taking false segments as additional class to arteries and veins.

7.3.3 Retinal Image Registration

Retinal image registration (Zana and Klein, 1999) demonstrates significant importance for clinical diagnostics and security systems. Features and locations of vascular landmarks including bifurcations, crossings, and overlaps are the common parameters examined during the identification process, as well as used in the registration process of retinal images, obtained in certain intervals, to investigate disease progression. The extracted AV trees are potentially useful for the above-mentioned applications in the context of inspecting vascular landmarks and trees structure.

7.3.4 Tree Topology Estimation

Tree like structures such as plant roots, tree branches, lightening, and other vasculature structures are often analysed in images, and thus requires efficient algorithms for extraction. The novel extraction system presented in this thesis with slight modification can be efficiently trained for such applications. In addition, the abovementioned structures project planar graphs after the cut is performed on the formulated MRF,

thus the graph based approach in this thesis may also be utilised for optimal extraction of planar graphs in general, such as in (Estrada et al., 2015).

7.3.5 Road Extraction

Automatic extraction of lanes and roads from high resolution satellite imagery is an important task in transportation applications (Gruen and Li, 1995). The availability of topographic databases of the Earth provides means for several applications such as traffic management, automated navigation, disaster prevention, military purposes, and critical decision making in emergency incidents. Image processing techniques implemented on aerial images for road extraction generally results in fragments, requiring efficient approaches to correctly connect these broken fragments. The fragmentation occurs generally due to shadows of objects including buildings, trees, roofs of houses, and the visual breakages caused by bridges. The local configuration model of this thesis can be employed to estimate highly likely connectivity of these fragments, yielding an improved performance of the road and lane extraction processes.

Bibliography

Donald A Adjeroh, Umasankar Kandaswamy, and J Vernon Odom. Texton-based segmentation of retinal vessels. *JOSA A*, 24(5):1384–1393, 2007. 42

Ravindra K Ahuja, Thomas L Magnanti, and James B Orlin. Network flows. Technical report, DTIC Document, 1988. 5

Bashir Al-Diri, Andrew Hunter, and David Steel. An active contour model for segmenting and measuring retinal vessels. *Medical Imaging, IEEE Transactions on*, 28(9):1488–1497, 2009. 2, 40, 49, 50, 53, 77, 123

Bashir Al-Diri, Andrew Hunter, David Steel, and Maged Habib. Automated analysis of retinal vascular network connectivity. *Computerized Medical Imaging and Graphics*, 34(6):462–470, 2010. 19, 61, 132, 135

George Azzopardi and Nicolai Petkov. Detection of retinal vascular bifurcations by trainable v4-like filters. In *Computer Analysis of Images and Patterns*, pages 451–459. Springer, 2011. 47

Peter Bankhead, C Norman Scholfield, J Graham McGeown, and Tim M Curtis. Fast retinal vessel detection and measurement using wavelets and edge location refinement. *PloS one*, 7(3):e32435, 2012. 40, 50, 53, 123

S Beatty and KG Au Eong. Acute occlusion of the retinal arteries: current concepts and recent advances in diagnosis and management. *Journal of accident & emergency medicine*, 17(5):324–329, 2000. 15

José M Bernardo and Adrian FM Smith. Bayesian theory, 2001. 26

Julian Besag. On the statistical analysis of dirty pictures. *Journal of the Royal Statistical Society. Series B (Methodological)*, pages 259–302, 1986. 31

G Bianco, Valeria De Antonellis, Silvana Castano, and Michele Melchiori. A markov random field approach for querying and reconciling heterogeneous databases. In *Database and Expert Systems Applications, 1999. Proceedings. Tenth International Workshop on*, pages 185–191. IEEE, 1999. 30

AC Bird, NM Bressler, SB Bressler, IH Chisholm, G Coscas, MD Davis, PTVM De Jong, CCW Klaver, BEKlein Klein, R Klein, et al. An international classification and grading system for age-related maculopathy and age-related macular degeneration. *Survey of ophthalmology*, 39(5):367–374, 1995. 9

Andrew Blake and Andrew Zisserman. *Visual reconstruction*, volume 2. MIT press Cambridge, 1987. 31

Yuri Boykov, Olga Veksler, and Ramin Zabih. Markov random fields with efficient approximations. In *Computer vision and pattern recognition, 1998. Proceedings. 1998 IEEE computer society conference on*, pages 648–655. IEEE, 1998. 31

Yuri Boykov, Olga Veksler, and Ramin Zabih. Fast approximate energy minimization via graph cuts. *Pattern Analysis and Machine Intelligence, IEEE Transactions on*, 23(11):1222–1239, 2001. 4, 31, 108, 140

Olaf Brinchmann-Hansen and Halvor Heier. Theoretical relations between light streak characteristics and optical properties of retinal vessels. *Acta Ophthalmologica*, 64(S179):33–37, 1986. 46

Olaf Brinchmann-Hansen, Halvor Heier, and Kjell Myhre. Fundus photography of width and intensity profiles of the blood column and the light reflex in retinal vessels. *Acta Ophthalmologica*, 64(S179):20–28, 1986. 46

Carol Yim-lui Cheung, Yingfeng Zheng, Wynne Hsu, Mong Li Lee, Qiangfeng Peter Lau, Paul Mitchell, Jie Jin Wang, Ronald Klein, and Tien Yin Wong. Retinal vascular tortuosity, blood pressure, and cardiovascular risk factors. *Ophthalmology*, 118(5):812–818, 2011. 1

Retina Society Terminology Committee et al. The classification of retinal detachment with proliferative vitreoretinopathy. *Ophthalmology*, 90(2):121–125, 1983. 9

Ronald P Danis and Matthew D Davis. Proliferative diabetic retinopathy. In *Diabetic Retinopathy*, pages 29–65. Springer, 2008. 9

Behdad Dashtbozorg, Ana Maria Mendonça, and Aurélio Campilho. An automatic graph-based approach for artery/vein classification in retinal images. *Image Processing, IEEE Transactions on*, 23(3):1073–1083, 2014. 23, 134

Persi Diaconis and David Freedman. On the consistency of bayes estimates. *The Annals of Statistics*, pages 1–26, 1986. 4

Koen Eppenhof, Erik Bekkers, Tos TJM Berendschot, Josien PW Pluim, and Bart M ter Haar Romeny. Retinal artery/vein classification via graph cut optimization. 2015. 24

Rolando Estrada, Carlo Tomasi, Scott C Schmidler, and Sina Farsiu. Tree topology estimation. *Pattern Analysis and Machine Intelligence, IEEE Transactions on*, 37 (8):1688–1701, 2015. 149

Marta Favali, Samaneh Abbasi-Sureshjani, Bart ter Haar Romeny, and Alessandro Sarti. Analysis of vessel connectivities in retinal images by cortically inspired spectral clustering. *arXiv preprint arXiv:1512.06559*, 2015. 19

Pedro F Felzenszwalb and Daniel P Huttenlocher. Efficient belief propagation for early vision. *International journal of computer vision*, 70(1):41–54, 2006. 31

Lester R Ford and Delbert R Fulkerson. Maximal flow through a network. *Canadian journal of Mathematics*, 8(3):399–404, 1956. 5, 33

William T Freeman, Egon C Pasztor, and Owen T Carmichael. Learning low-level vision. *International journal of computer vision*, 40(1):25–47, 2000. 31

Nir Friedman, Dan Geiger, and Moises Goldszmidt. Bayesian network classifiers. *Machine learning*, 29(2-3):131–163, 1997. 27

Stuart Geman and Donald Geman. Stochastic relaxation, gibbs distributions, and the bayesian restoration of images. *Pattern Analysis and Machine Intelligence, IEEE Transactions on*, (6):721–741, 1984. 31, 108

Stuart Geman and Christine Graffigne. Markov random field image models and their applications to computer vision. In *Proceedings of the International Congress of Mathematicians*, volume 1, page 2, 1986. 4

Ben Glocker, Nikos Komodakis, Georgios Tziritas, Nassir Navab, and Nikos Paragios. Dense image registration through mrfs and efficient linear programming. *Medical image analysis*, 12(6):731–741, 2008. 108

IKUO GOTO, KATSUHARU KIMOTO, SHIBANOSUKE KATSUKI, TAKAAKI MIMATSU, and IKUI HIROSHI. Pathological studies on the intracerebral and retinal arteries in cerebrovascular and noncerebrovascular diseases. *Stroke*, 6(3): 263–269, 1975. 14

DM Greig, BT Porteous, and Allan H Seheult. Exact maximum a posteriori estimation for binary images. *Journal of the Royal Statistical Society. Series B (Methodological)*, pages 271–279, 1989. 31

Enrico Grisan and Alfredop Ruggeri. A divide et impera strategy for automatic classification of retinal vessels into arteries and veins. In *Engineering in medicine and biology society, 2003. Proceedings of the 25th annual international conference of the IEEE*, volume 1, pages 890–893. IEEE, 2003. 22, 103

Armin Gruen and Haihong Li. Road extraction from aerial and satellite images by dynamic programming. *ISPRS Journal of Photogrammetry and Remote Sensing*, 50(4):11–20, 1995. 149

Sohan Singh Hayreh. Central retinal vein occlusion. In *Ocular Vascular Occlusive Disorders*, pages 621–743. Springer, 2015. 15

Sohan Singh Hayreh, Bridget Zimmerman, Mark J McCarthy, and Patricia Podhajsky. Systemic diseases associated with various types of retinal vein occlusion. *American journal of ophthalmology*, 131(1):61–77, 2001. 13

Fabrice Heitz and Patrick Bouthemy. Multimodal estimation of discontinuous optical flow using markov random fields. *Pattern Analysis and Machine Intelligence, IEEE Transactions on*, 15(12):1217–1232, 1993. 29

A Hoover. Stare database. *Available: Available: http://www. ces. clemson. edu/˜ ahoover/stare*, 1975. 42

William F Hoyt, Lars Frisen, and Nancy M Newman. Fundoscopy of nerve fiber layer defects in glaucoma. *Investigative ophthalmology & visual science*, 12(11): 814–829, 1973. 9

Qiao Hu, Michael D Abràmoff, and Mona K Garvin. Automated construction of arterial and venous trees in retinal images. *Journal of Medical Imaging*, 2(4): 044001–044001, 2015. 25, 134, 135, 136

Larry D Hubbard, Rosemary J Brothers, William N King, Limin X Clegg, Ronald Klein, Lawton S Cooper, A Richey Sharrett, Matthew D Davis, Jianwen Cai, Atherosclerosis Risk in Communities Study Group, et al. Methods for evaluation of retinal microvascular abnormalities associated with hypertension/sclerosis in the atherosclerosis risk in communities study. *Ophthalmology*, 106(12):2269–2280, 1999. 1

Andrew Hunter, James Lowell, Robert Ryder, Ansu Basu, David Steel, et al. Tramline filtering for retinal vessel segmentation. 2005. 48

Hiroshi Ishikawa and Davi Geiger. Segmentation by grouping junctions. In *Computer Vision and Pattern Recognition, 1998. Proceedings. 1998 IEEE Computer Society Conference on*, pages 125–131. IEEE, 1998. 31

Herbert F Jelinek, Michael J Cree, Jorge JG Leandro, João VB Soares, Roberto M Cesar, and A Luckie. Automated segmentation of retinal blood vessels and identification of proliferative diabetic retinopathy. *JOSA A*, 24(5):1448–1456, 2007. 42

Daniel J Jobson, Zia-ur Rahman, and Glenn A Woodell. A multiscale retinex for bridging the gap between color images and the human observation of scenes. *Image Processing, IEEE Transactions on*, 6(7):965–976, 1997. 124

Vinayak S Joshi, Joseph M Reinhardt, Mona K Garvin, and Michael D Abramoff. Automated method for identification and artery-venous classification of vessel trees in retinal vessel networks. *PloS one*, 9(2):e88061, 2014. 25, 134, 135

Zoltan Kato and Ting-Chuen Pong. A markov random field image segmentation model for color textured images. *Image and Vision Computing*, 24(10):1103–1114, 2006. 29

Tomi Kauppi, Valentina Kalesnykiene, Joni-Kristian Kamarainen, Lasse Lensu, Iiris Sorri, Hannu Uusitalo, Heikki Kälviäinen, and Juhani Pietilä. Diaretdb0: Evaluation database and methodology for diabetic retinopathy algorithms. *Machine*

Vision and Pattern Recognition Research Group, Lappeenranta University of Technology, Finland, 2006. 42

Ross Kindermann, James Laurie Snell, et al. *Markov random fields and their applications*, volume 1. American Mathematical Society Providence, RI, 1980. 4, 27

LA King, AV Stanton, PS Sever, SA Thom, and AD Hughes. Arteriolar length-diameter (l: D) ratio: a geometric parameter of the retinal vasculature diagnostic of hypertension. *Journal of human hypertension*, 10(6):417–418, 1996. 15

Alfred G Knudson. Mutation and cancer: statistical study of retinoblastoma. *Proceedings of the National Academy of Sciences*, 68(4):820–823, 1971. 9

Claudia Kondermann, Daniel Kondermann, and Michelle Yan. Blood vessel classification into arteries and veins in retinal images. In *Medical Imaging*, pages 651247–651247. International Society for Optics and Photonics, 2007. 15, 22, 46

Susan Koreen, Rony Gelman, M Elena Martinez-Perez, Lei Jiang, Audina M Berrocal, Ditte J Hess, John T Flynn, and Michael F Chiang. Evaluation of a computer-based system for plus disease diagnosis in retinopathy of prematurity. *Ophthalmology*, 114(12):e59–e67, 2007. 1

Michael Larsen, Lotte Berdiin Colmorn, Marie Bønnelycke, Risto Kaaja, Ilkka Immonen, Birgit Sander, and Sirpa Loukovaara. Retinal artery and vein diameters during pregnancy in diabetic women. *Investigative ophthalmology & visual science*, 46(2):709–713, 2005. 46

Qiangfeng Peter Lau, Mong Li Lee, Wei-Chou Hsu, and Tien Yin Wong. Simultaneously identifying all true vessels from segmented retinal images. *Biomedical Engineering, IEEE Transactions on*, 60(7):1851–1858, 2013. 21, 134

SR Lesage, TH Mosley, TY Wong, M Szklo, D Knopman, Diane J Catellier, SR Cole, R Klein, J Coresh, LH Coker, et al. Retinal microvascular abnormalities and cognitive decline the aric 14-year follow-up study. *Neurology*, 73(11):862–868, 2009. 1

Huiqi Li, Wynne Hsu, Mong Li Lee, and Hongyiu Wang. A piecewise gaussian model for profiling and differentiating retinal vessels. In *Image Processing, 2003.*

ICIP 2003. Proceedings. 2003 International Conference on, volume 1, pages I–1069. IEEE, 2003. 22

Qiaoliang Li, Bowei Feng, LinPei Xie, Ping Liang, Huisheng Zhang, and Tianfu Wang. A cross-modality learning approach for vessel segmentation in retinal images. 2015. 49

Stan Z Li. *Markov random field modeling in image analysis*. Springer Science & Business Media, 2009. 28

Gerald Liew, A Richey Sharrett, Richard Kronmal, Ronald Klein, Tien Yin Wong, Paul Mitchell, Annette Kifley, and Jie Jin Wang. Measurement of retinal vascular caliber: issues and alternatives to using the arteriole to venule ratio. *Investigative ophthalmology & visual science*, 48(1):52–57, 2007. 46

Kai-Shun Lin, Chia-Ling Tsai, Chih-Hsiangng Tsai, Michal Sofka, Shih-Jen Chen, and Wei-Yang Lin. Retinal vascular tree reconstruction with anatomical realism. *Biomedical Engineering, IEEE Transactions on*, 59(12):3337–3347, 2012. 20, 134, 135

James Lowell, Andrew Hunter, David Steel, Ansu Basu, Robert Ryder, Eric Fletcher, and Lee Kennedy. Optic nerve head segmentation. *Medical Imaging, IEEE Transactions on*, 23(2):256–264, 2004a. 140

James Lowell, Andrew Hunter, David Steel, Ansu Basu, Robert Ryder, and R Lee Kennedy. Measurement of retinal vessel widths from fundus images based on 2-d modeling. *Medical Imaging, IEEE Transactions on*, 23(10):1196–1204, 2004b. 46

Carmen Alina Lupaşcu, Domenico Tegolo, and Emanuele Trucco. Fabc: retinal vessel segmentation using adaboost. *Information Technology in Biomedicine, IEEE Transactions on*, 14(5):1267–1274, 2010. 49

William M Lyle. The clinical handbook of ophthalmology. *Optometry & Vision Science*, 72(1):45, 1995. 11

Diego Marín, Arturo Aquino, Manuel Emilio Gegúndez-Arias, and José Manuel Bravo. A new supervised method for blood vessel segmentation in retinal images by using gray-level and moment invariants-based features. *Medical Imaging, IEEE Transactions on*, 30(1):146–158, 2011. 48

M Elena Martinez-Perez, Alun D Hughes, Simon A Thom, Anil A Bharath, and Kim H Parker. Segmentation of blood vessels from red-free and fluorescein retinal images. *Medical image analysis*, 11(1):47–61, 2007. 42

Barry R Masters. Fractal analysis of the vascular tree in the human retina. *Annu. Rev. Biomed. Eng.*, 6:427–452, 2004. 15

Ana Maria Mendonca and Aurelio Campilho. Segmentation of retinal blood vessels by combining the detection of centerlines and morphological reconstruction. *Medical Imaging, IEEE Transactions on*, 25(9):1200–1213, 2006. 48

S Mohammed, T Morris, and N Thacker. Optic disk segmentation using texture. 2014. 140

Cecil D Murray. The physiological principle of minimum work applied to the angle of branching of arteries. *The Journal of general physiology*, 9(6):835–841, 1926. 15

Harihar Narasimha-Iyer, James M Beach, Bahram Khoobehi, and Badrinath Roysam. Automatic identification of retinal arteries and veins from dual-wavelength images using structural and functional features. *Biomedical Engineering, IEEE Transactions on*, 54(8):1427–1435, 2007. 23

Harihar Narasimha-Iyer, Vijay Mahadevan, James M Beach, and Badrinath Roysam. Improved detection of the central reflex in retinal vessels using a generalized dual-gaussian model and robust hypothesis testing. *Information Technology in Biomedicine, IEEE Transactions on*, 12(3):406–410, 2008. 46

Jan Odstrcilik, Radim Kolar, Attila Budai, Joachim Hornegger, Jiri Jan, Jiri Gazarek, Tomas Kubena, Pavel Cernosek, Ondrej Svoboda, and Elli Angelopoulou. Retinal vessel segmentation by improved matched filtering: evaluation on a new high-resolution fundus image database. *Image Processing, IET*, 7(4):373–383, 2013. 49

Wendeson S Oliveira, Joyce Vitor Teixeira, Tsang Ing Ren, George DC Cavalcanti, and Jan Sijbers. Unsupervised retinal vessel segmentation using combined filters. *PloS one*, 11(2):e0149943, 2016.

Renzo Perfetti, Elisa Ricci, Daniele Casali, and Giovanni Costantini. Cellular neural networks with virtual template expansion for retinal vessel segmentation. *Circuits and Systems II: Express Briefs, IEEE Transactions on*, 54(2):141–145, 2007. 42

Touseef Qureshi, Andrew Hunter, and Bashir Al-Diri. A bayesian framework for the local configuration of retinal junctions. In *Proceedings of the IEEE Conference on Computer Vision and Pattern Recognition*, pages 3105–3110, 2014. 20, 40

Touseef Ahmad Qureshi, Hayder Amin, Mutawarra Hussain, Rashid Jalal Qureshi, and Bashir Al-Diri. Automatic localization of the optic disc in retinal fundus images using multiple features. In *Bioinformatics & Bioengineering (BIBE), 2012 IEEE 12th International Conference on*, pages 488–493. IEEE, 2012. 140

Touseef Ahmad Qureshi, Maged Habib, Andrew Hunter, and Bashir Al-Diri. A manually-labeled, artery/vein classified benchmark for the drive dataset. In *Computer-Based Medical Systems (CBMS), 2013 IEEE 26th International Symposium on*, pages 485–488. IEEE, 2013. 40

D Relan, T MacGillivray, L Ballerini, and Emanuele Trucco. Retinal vessel classification: sorting arteries and veins. In *Engineering in Medicine and Biology Society (EMBC), 2013 35th Annual International Conference of the IEEE*, pages 7396–7399. IEEE, 2013. 103

Elisa Ricci and Renzo Perfetti. Retinal blood vessel segmentation using line operators and support vector classification. *Medical Imaging, IEEE Transactions on*, 26(10): 1357–1365, 2007. 49

Kai Rothaus, Xiaoyi Jiang, and Paul Rhiem. Separation of the retinal vascular graph in arteries and veins based upon structural knowledge. *Image and Vision Computing*, 27(7):864–875, 2009. 23

Sébastien Roy and Ingemar J Cox. A maximum-flow formulation of the n-camera stereo correspondence problem. In *Computer Vision, 1998. Sixth International Conference on*, pages 492–499. IEEE, 1998. 31

Sohini Roychowdhury, Dara D Koozekanani, and Keshab K Parhi. Iterative vessel segmentation of fundus images. *Biomedical Engineering, IEEE Transactions on*, 62(7):1738–1749, 2015. 49

Marc Saez, Sonia González-Vázquez, Manuel González-Penedo, Maria Antònia Barceló, Marta Pena-Seijo, Gabriel Coll de Tuero, and Antonio Pose-Reino. Development of an automated system to classify retinal vessels into arteries and veins. *Computer methods and programs in biomedicine*, 108(1):367–376, 2012. 103

Eric Saund. Logic and mrf circuitry for labeling occluding and thinline visual contours. *Advances in Neural Information Processing Systems*, 18:1153, 2006. 30

Paolo S Silva, Jerry D Cavallerano, Jennifer K Sun, Jason Noble, Lloyd M Aiello, and Lloyd Paul Aiello. Nonmydriatic ultrawide field retinal imaging compared with dilated standard 7-field 35-mm photography and retinal specialist examination for evaluation of diabetic retinopathy. *American journal of ophthalmology*, 154(3): 549–559, 2012. 9

Anne H Schistad Solberg, Torfinn Taxt, and Anil K Jain. A markov random field model for classification of multisource satellite imagery. *Geoscience and Remote Sensing, IEEE Transactions on*, 34(1):100–113, 1996. 28

Joes Staal, Michael D Abràmoff, Meindert Niemeijer, Max A Viergever, and Bram Van Ginneken. Ridge-based vessel segmentation in color images of the retina. *Medical Imaging, IEEE Transactions on*, 23(4):501–509, 2004. 6

Tatijana Stošić and Borko D Stošić. Multifractal analysis of human retinal vessels. *Medical Imaging, IEEE Transactions on*, 25(8):1101–1107, 2006. 15, 147

Cong Sun, Jie Jin Wang, David A Mackey, and Tien Y Wong. Retinal vascular caliber: systemic, environmental, and genetic associations. *Survey of ophthalmology*, 54 (1):74–95, 2009. 1

Richard Szeliski, Ramin Zabih, Daniel Scharstein, Olga Veksler, Vladimir Kolmogorov, Aseem Agarwala, Marshall Tappen, and Carsten Rother. A comparative study of energy minimization methods for markov random fields. In *Computer Vision–ECCV 2006*, pages 16–29. Springer, 2006. 29

Lara Tramontan, Enrico Grisan, and Alfredo Ruggeri. An improved system for the automatic estimation of the arteriolar-to-venular diameter ratio (avr) in retinal images. In *Engineering in Medicine and Biology Society, 2008. EMBS 2008. 30th Annual International Conference of the IEEE*, pages 3550–3553. IEEE, 2008. 46

Chia-Ling Tsai, Charles V Stewart, Howard L Tanenbaum, and Badrinath Roysam. Model-based method for improving the accuracy and repeatability of estimating vascular bifurcations and crossovers from retinal fundus images. *Information Technology in Biomedicine, IEEE Transactions on*, 8(2):122–130, 2004. 20, 61

David Tsai, Matthew Flagg, Atsushi Nakazawa, and James M Rehg. Motion coherent tracking using multi-label mrf optimization. *International journal of computer vision*, 100(2):190–202, 2012. 29

Florence Tupin, Henri Maitre, Jean-Francois Mangin, Jean-Marie Nicolas, and Eugene Pechersky. Detection of linear features in sar images: application to road network extraction. *Geoscience and Remote Sensing, IEEE Transactions on*, 36 (2):434–453, 1998. 31

Olga Veksler. *Efficient graph-based energy minimization methods in computer vision*. PhD thesis, Cornell University, 1999. 140

Mary B Vickerman, Patricia A Keith, Terri L McKay, Dan J Gedeon, Michiko Watanabe, Monica Montano, Ganga Karunamuni, Peter K Kaiser, Jonathan E Sears, Quteba Ebrahem, et al. Vesgen 2d: Automated, user-interactive software for quantification and mapping of angiogenic and lymphangiogenic trees and networks. *The anatomical record*, 292(3):320–332, 2009. 2

Chaohui Wang, Nikos Komodakis, and Nikos Paragios. Markov random field modeling, inference & learning in computer vision & image understanding: A survey. *Computer Vision and Image Understanding*, 117(11):1610–1627, 2013. 28, 31, 96

Li Wang, Abhir Bhalerao, and Roland Wilson. Analysis of retinal vasculature using a multiresolution hermite model. *Medical Imaging, IEEE Transactions on*, 26(2): 137–152, 2007. 42

Yair Weiss and William T Freeman. On the optimality of solutions of the max-product belief-propagation algorithm in arbitrary graphs. *Information Theory, IEEE Transactions on*, 47(2):736–744, 2001. 31

Tien Yin Wong, Ronald Klein, Barbara EK Klein, James M Tielsch, Larry Hubbard, and F Javier Nieto. Retinal microvascular abnormalities and their relationship

with hypertension, cardiovascular disease, and mortality. *Survey of ophthalmology*, 46(1):59–80, 2001. 13

Tien Yin Wong, Anoop Shankar, Ronald Klein, Barbara EK Klein, and Larry D Hubbard. Prospective cohort study of retinal vessel diameters and risk of hypertension. *bmj*, 329(7457):79, 2004. 1

Chang-Hua Wu, Gady Agam, and Peter Stanchev. A general framework for vessel segmentation in retinal images. In *2007 International Symposium on Computational Intelligence in Robotics and Automation*, pages 37–42. IEEE, 2007.

Faguo Yang and Tianzi Jiang. Pixon-based image segmentation with markov random fields. *Image Processing, IEEE Transactions on*, 12(12):1552–1559, 2003. 29

M Zamir. Optimality principles in arterial branching. *Journal of Theoretical Biology*, 62(1):227–251, 1976. 46

M Zamir. Nonsymmetrical bifurcations in arterial branching. *The Journal of general physiology*, 72(6):837–845, 1978. 46

M Zamir and N Brown. Arterial branching in various parts of the cardiovascular system. *American Journal of Anatomy*, 163(4):295–307, 1982. 46

M Zamir and H Chee. Branching characteristics of human coronary arteries. *Canadian journal of physiology and pharmacology*, 64(6):661–668, 1986. 46

M Zamir, JA Medeiros, and TK Cunningham. Arterial bifurcations in the human retina. *The Journal of general physiology*, 74(4):537–548, 1979. 15

Andrea Zamperini, Andrea Giachetti, Emanuele Trucco, and Khai Sing Chin. Effective features for artery-vein classification in digital fundus images. In *Computer-Based Medical Systems (CBMS), 2012 25th International Symposium on*, pages 1–6. IEEE, 2012. 23

Frédéric Zana and Jean-Claude Klein. A multimodal registration algorithm of eye fundus images using vessels detection and hough transform. *Medical Imaging, IEEE Transactions on*, 18(5):419–428, 1999. 148

Jingdan Zhang, Yingjie Cui, Wuhan Jiang, and Le Wang. Blood vessel segmentation of retinal images based on neural network. In *International Conference on Image and Graphics*, pages 11–17. Springer, 2015. 49

Yitian Zhao, Yonghuai Liu, Xiangqian Wu, Simon P Harding, and Yalin Zheng. Retinal vessel segmentation: An efficient graph cut approach with retinex and local phase. *PloS one*, 10(4):e0122332, 2015. 50

Appendix A

Sample Images with Classified-Vessels for DRIVE

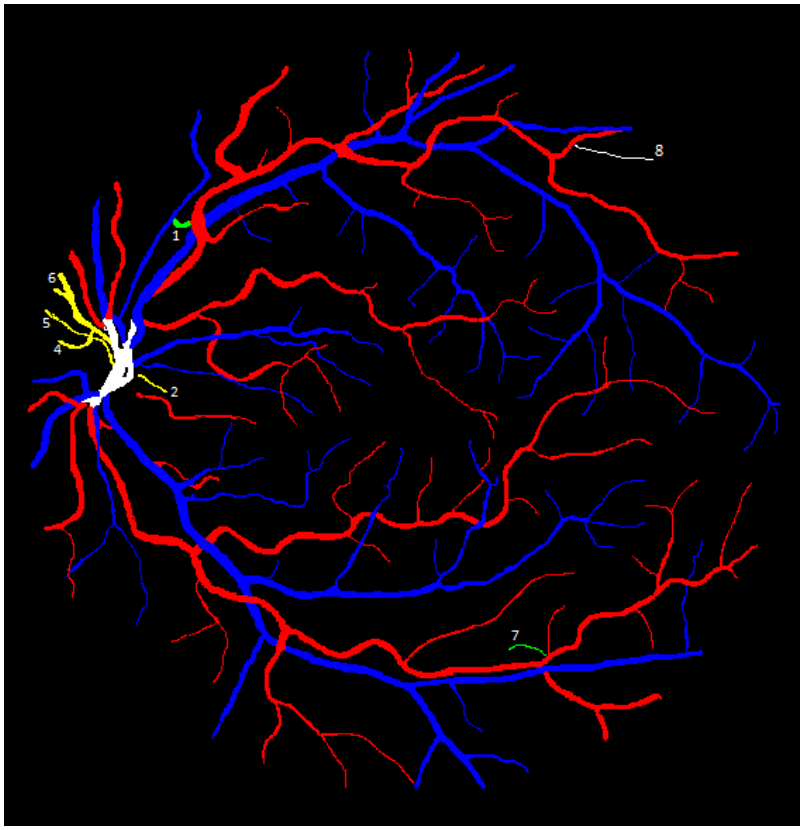

(a) Image 1

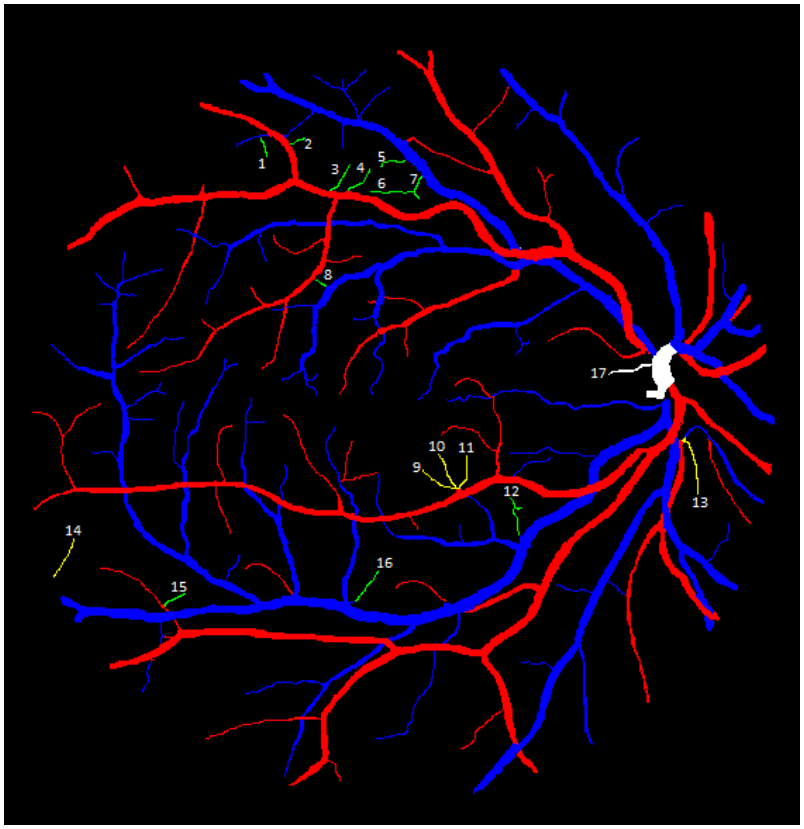

(b) Image 2

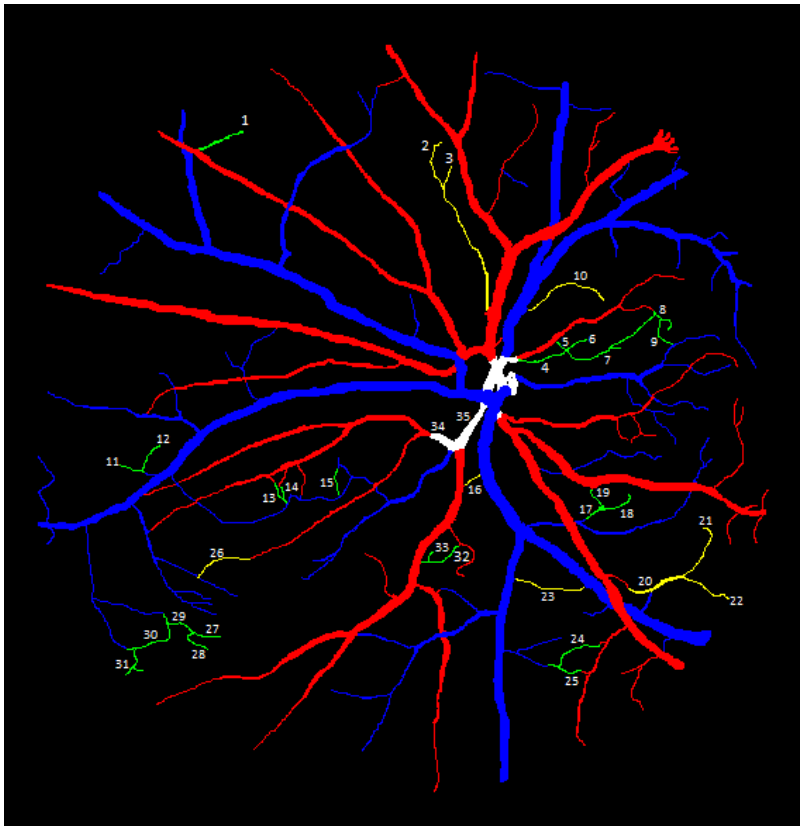

(a) Image 3

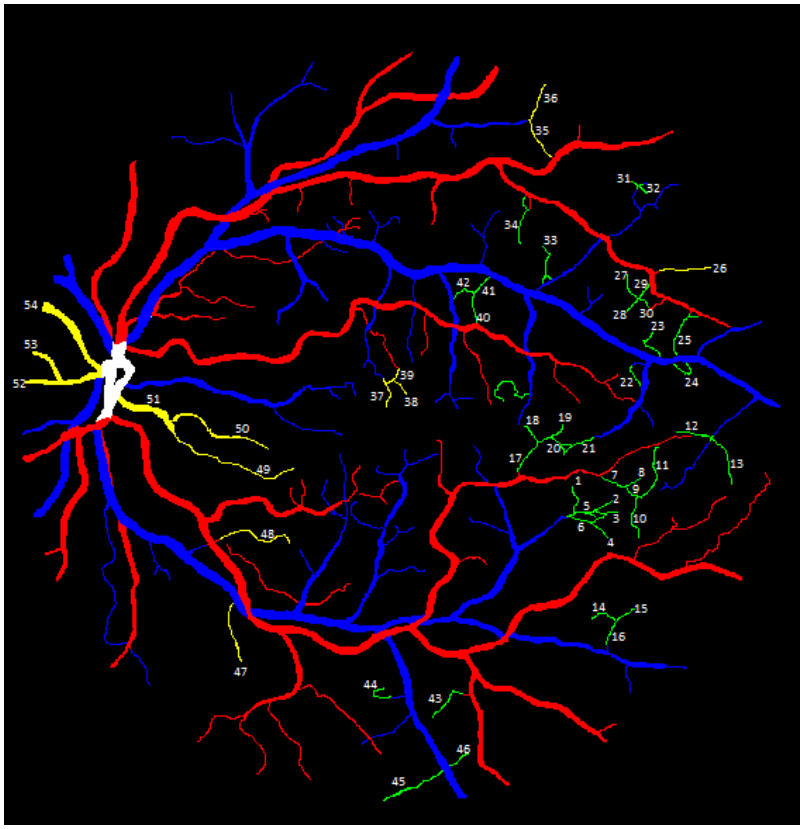

(b) Image 4

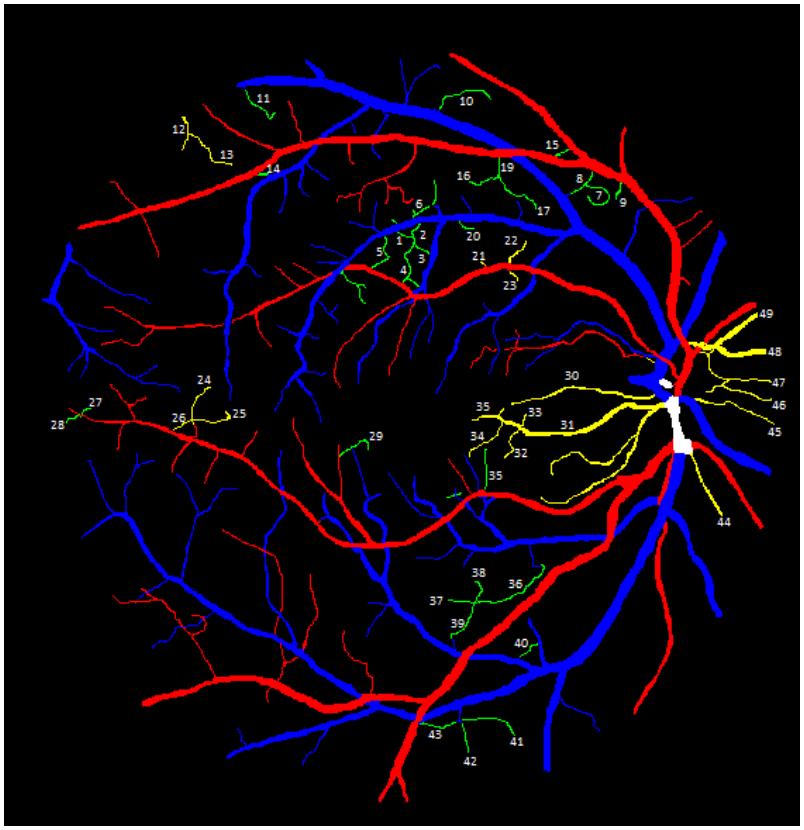

(a) Image 5

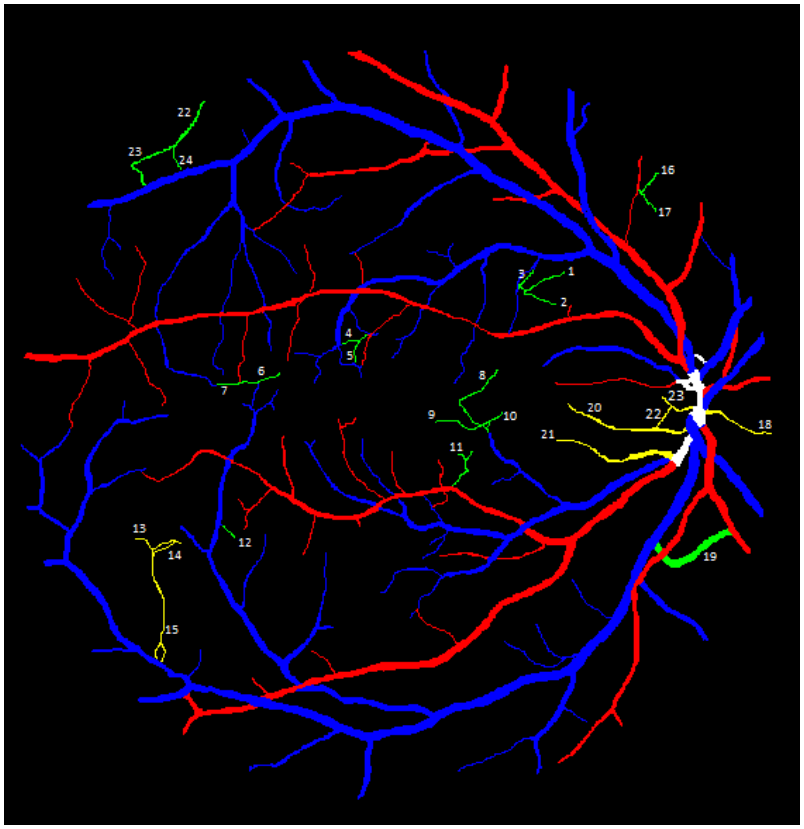

(b) Image 6

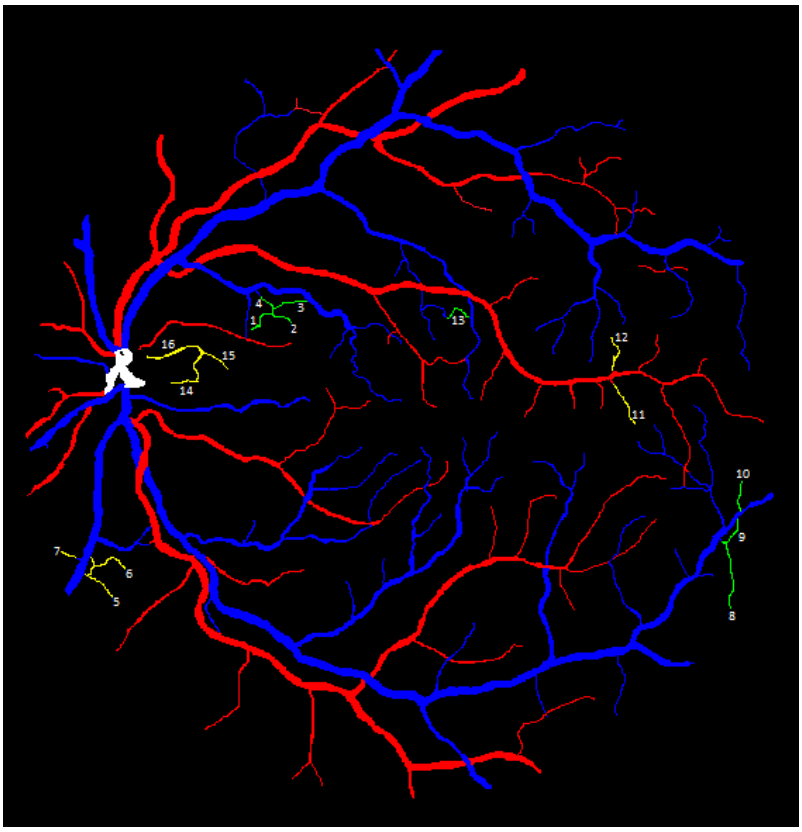

(a) Image 7

Appendix B

Sample Images with Local Configuration of Junctions

The red lines on each image are used to connect ends of two segments, blue lines for connecting ends of three segments and magenta lines are for connecting ends of four segments at a junction. The overlapping segments are shown in green colour edges.

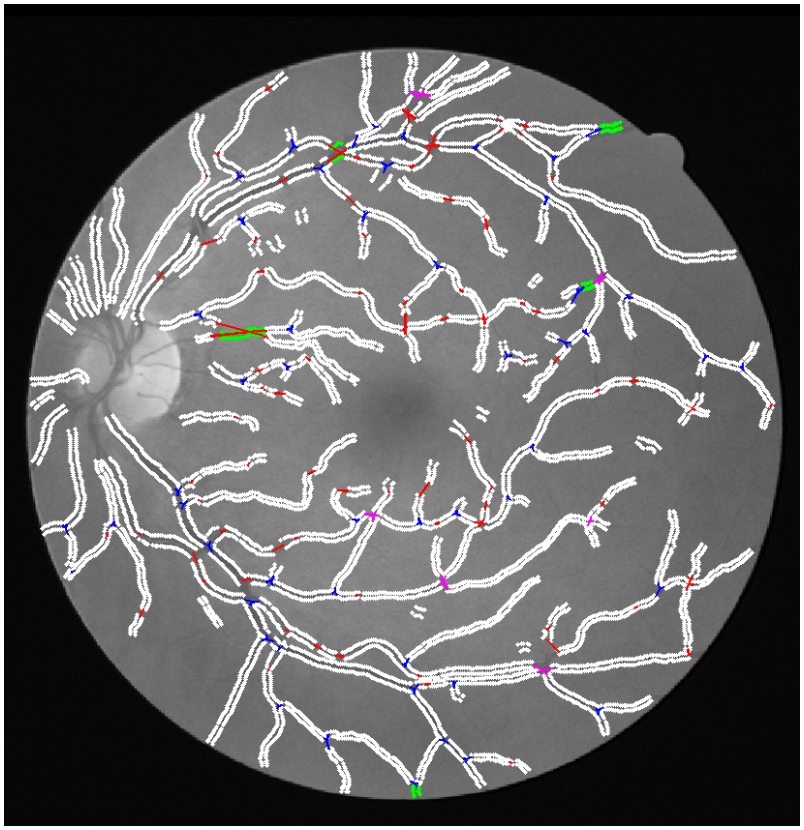

(a) Image 1-$DSJS_1$

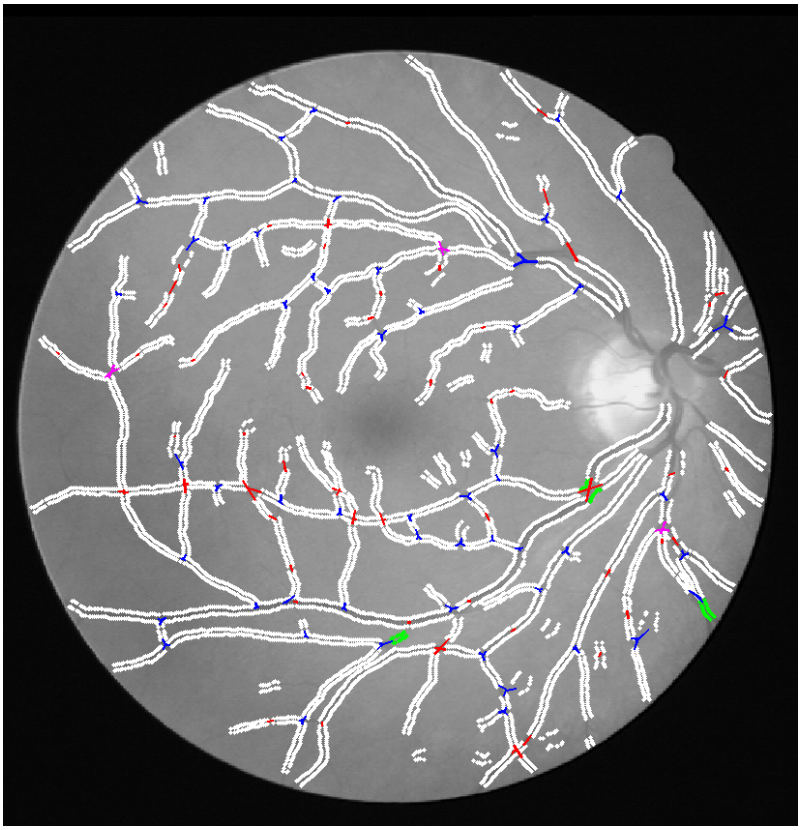

(b) Image 2-$DSJS_1$

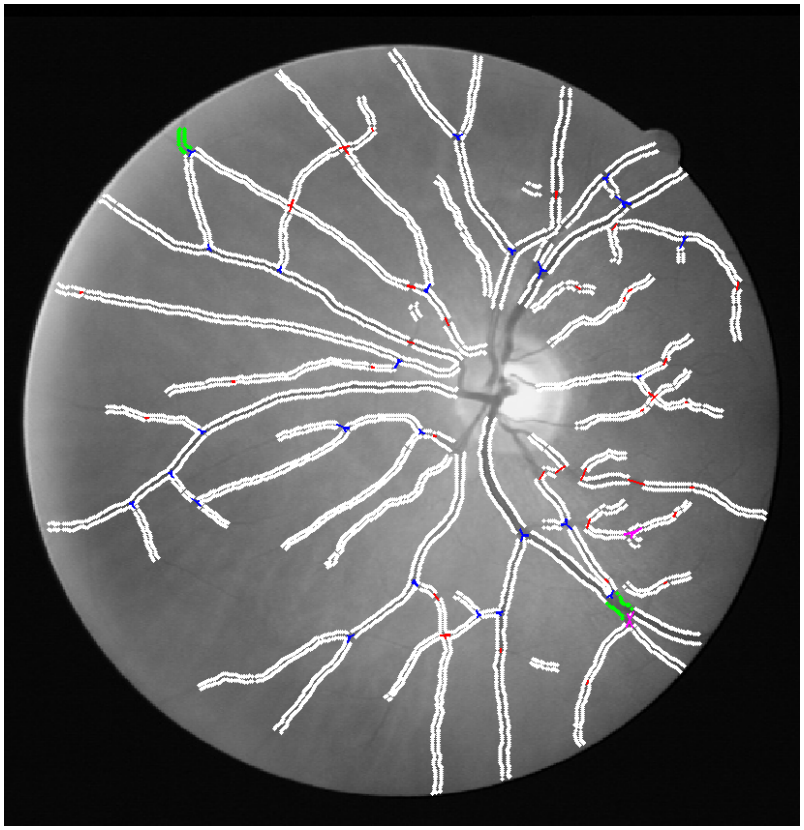

(a) Image 3-$DSJS_1$

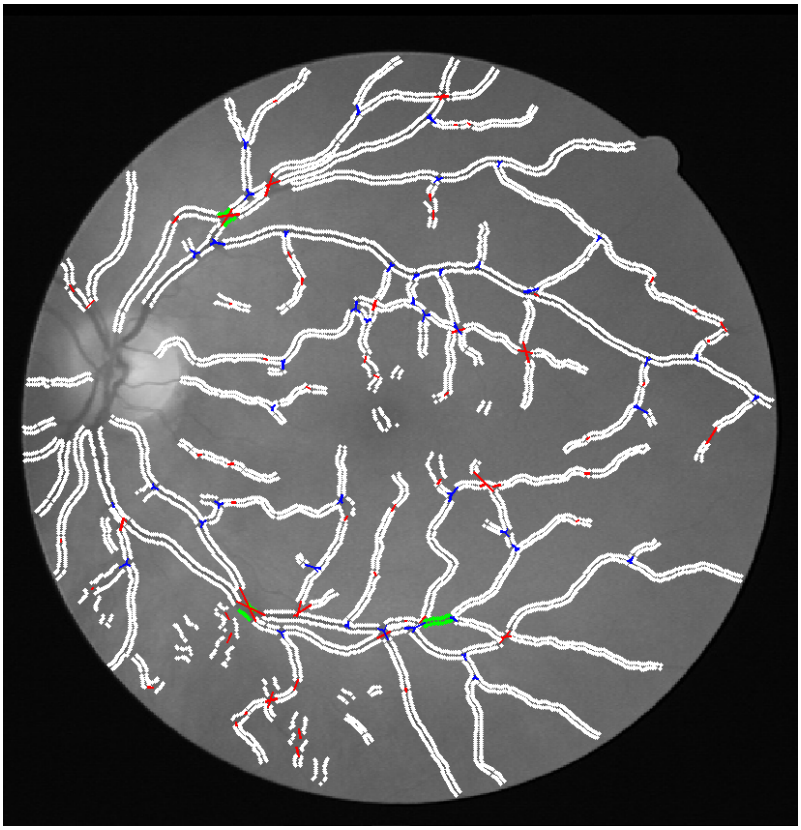

(b) Image 4-$DSJS_1$

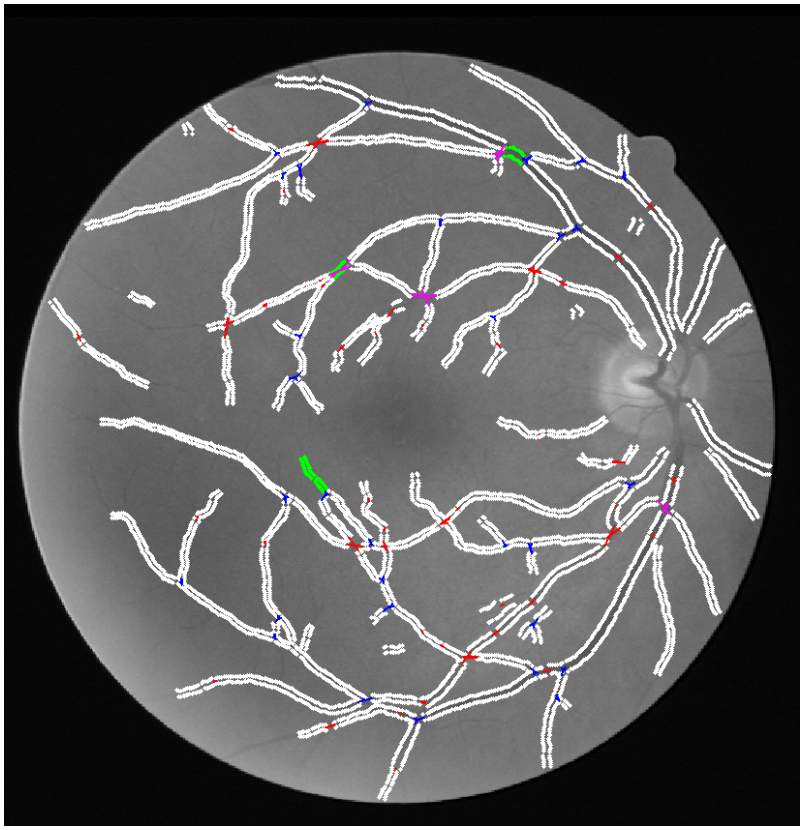

(a) Image 5-$DSJS_1$

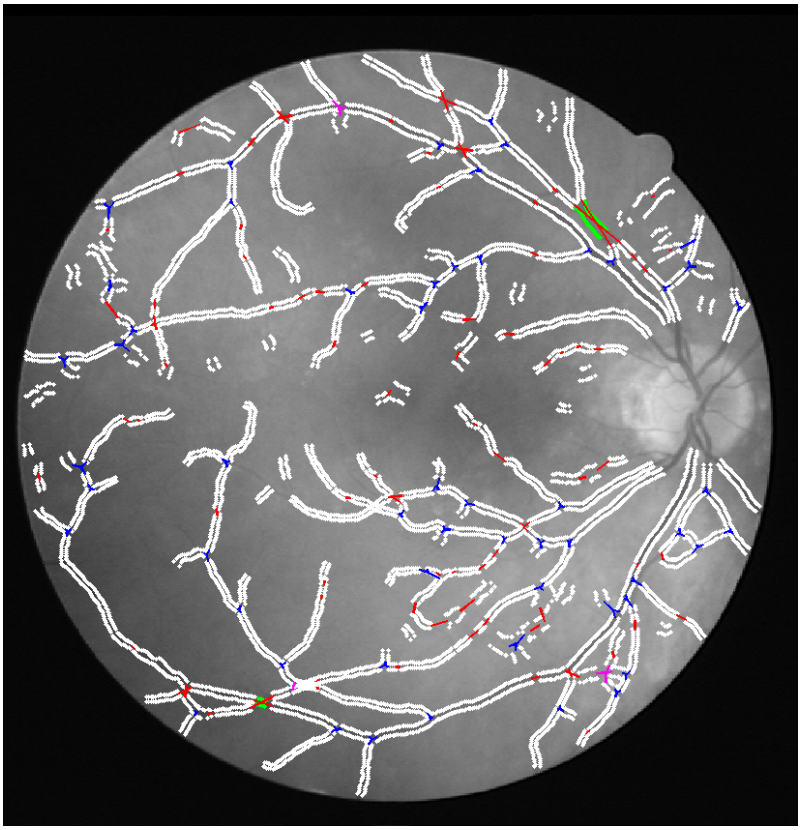

(b) Image 6-$DSJS_1$

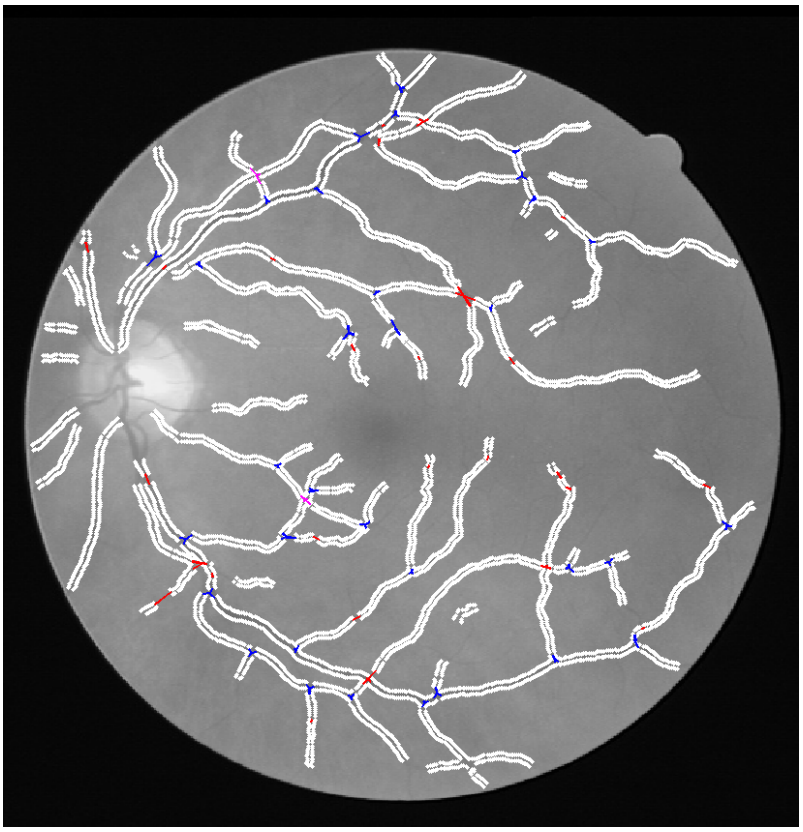

(a) Image 7-$DSJS_1$

Appendix C

Sample Images of Extracted Trees of Arteries and Veins

Segments with red colour edges are identified as arteries whilst segments with blue colour edges are identified as veins.

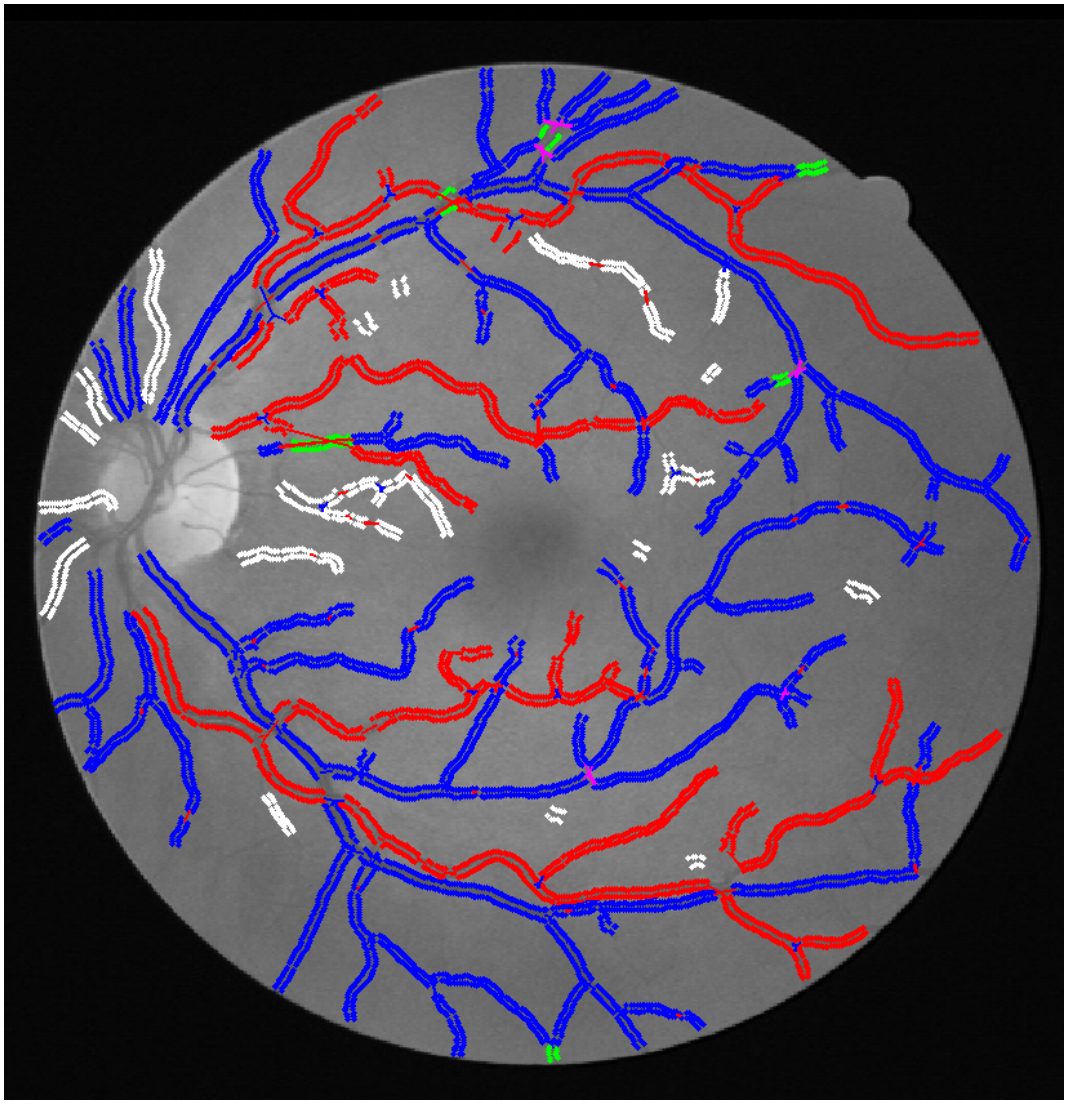

Fig. C.1 Image 1-$DSJS_1$

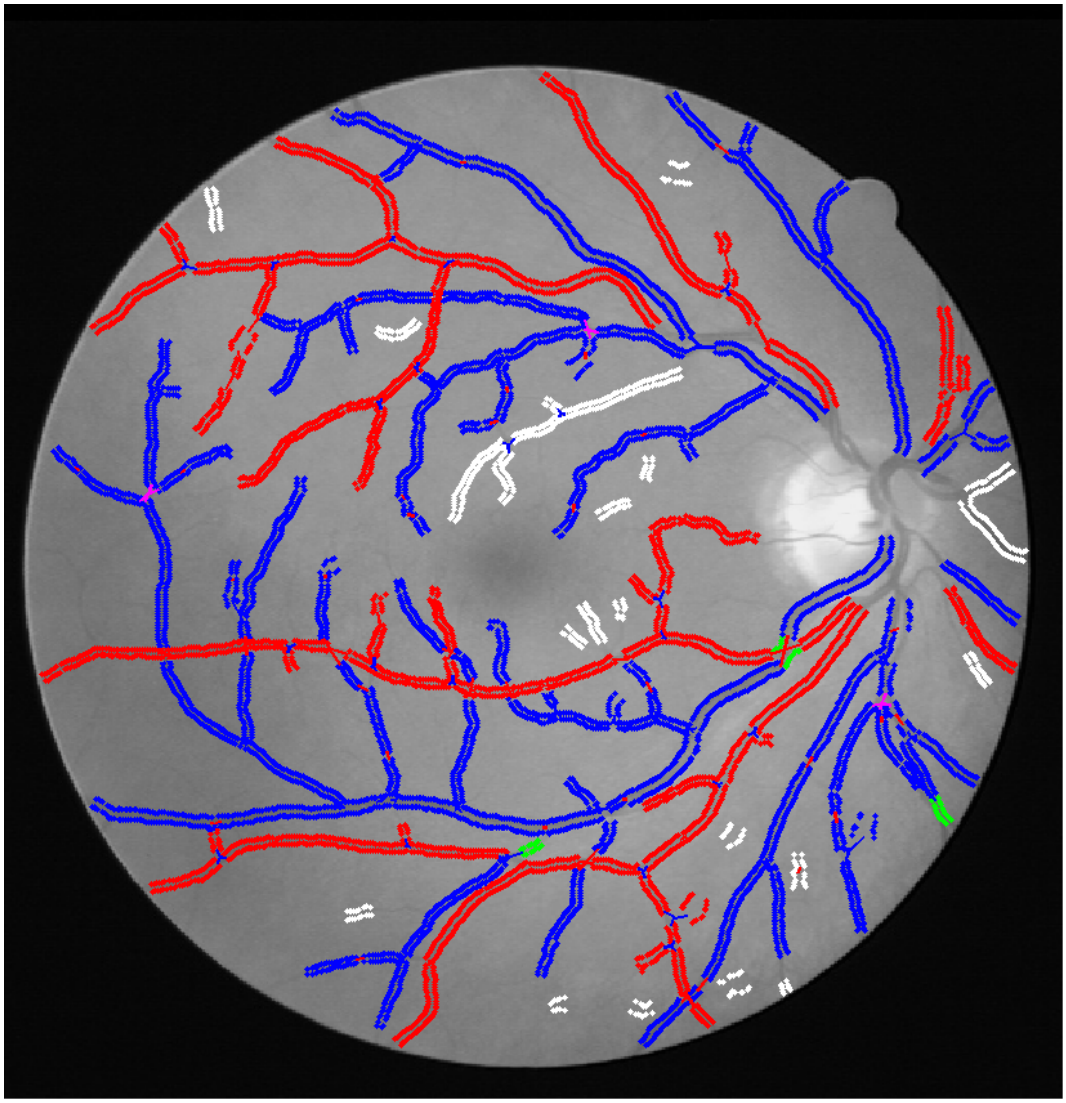

Fig. C.2 Image 2-$DSJS_1$

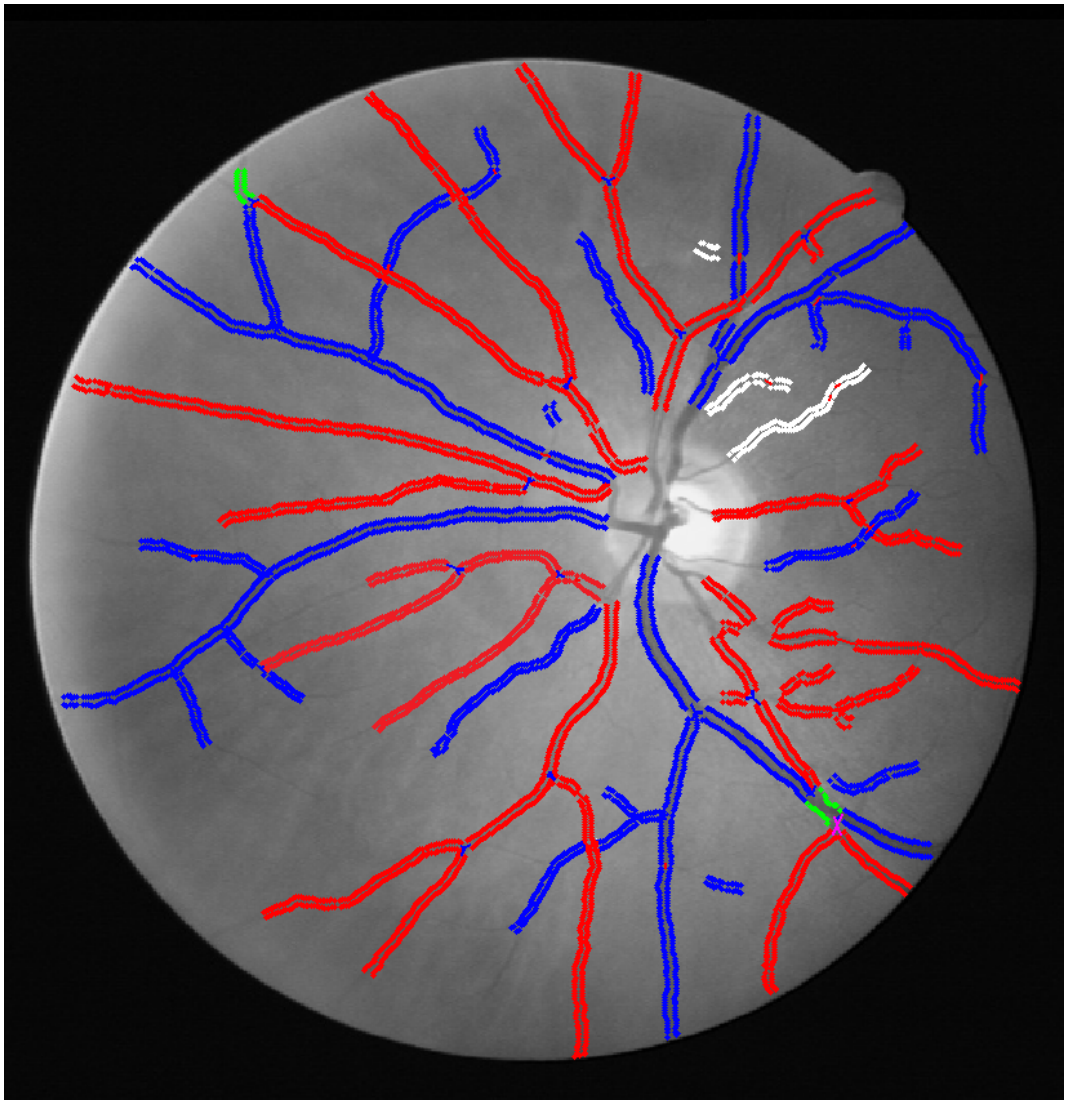

Fig. C.3 Image 3-$DSJS_1$

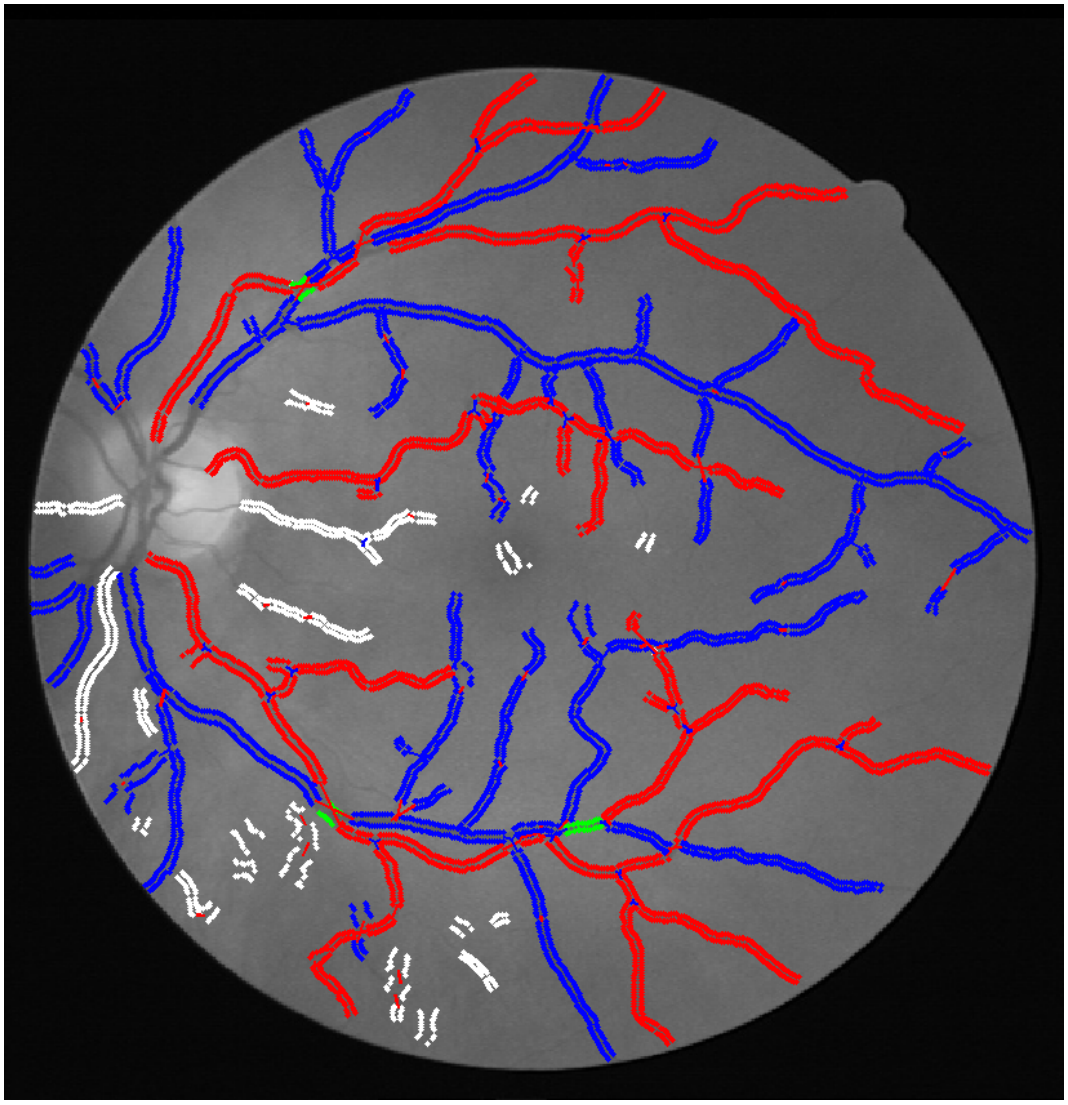

Fig. C.4 Image 4-$DSJS_1$

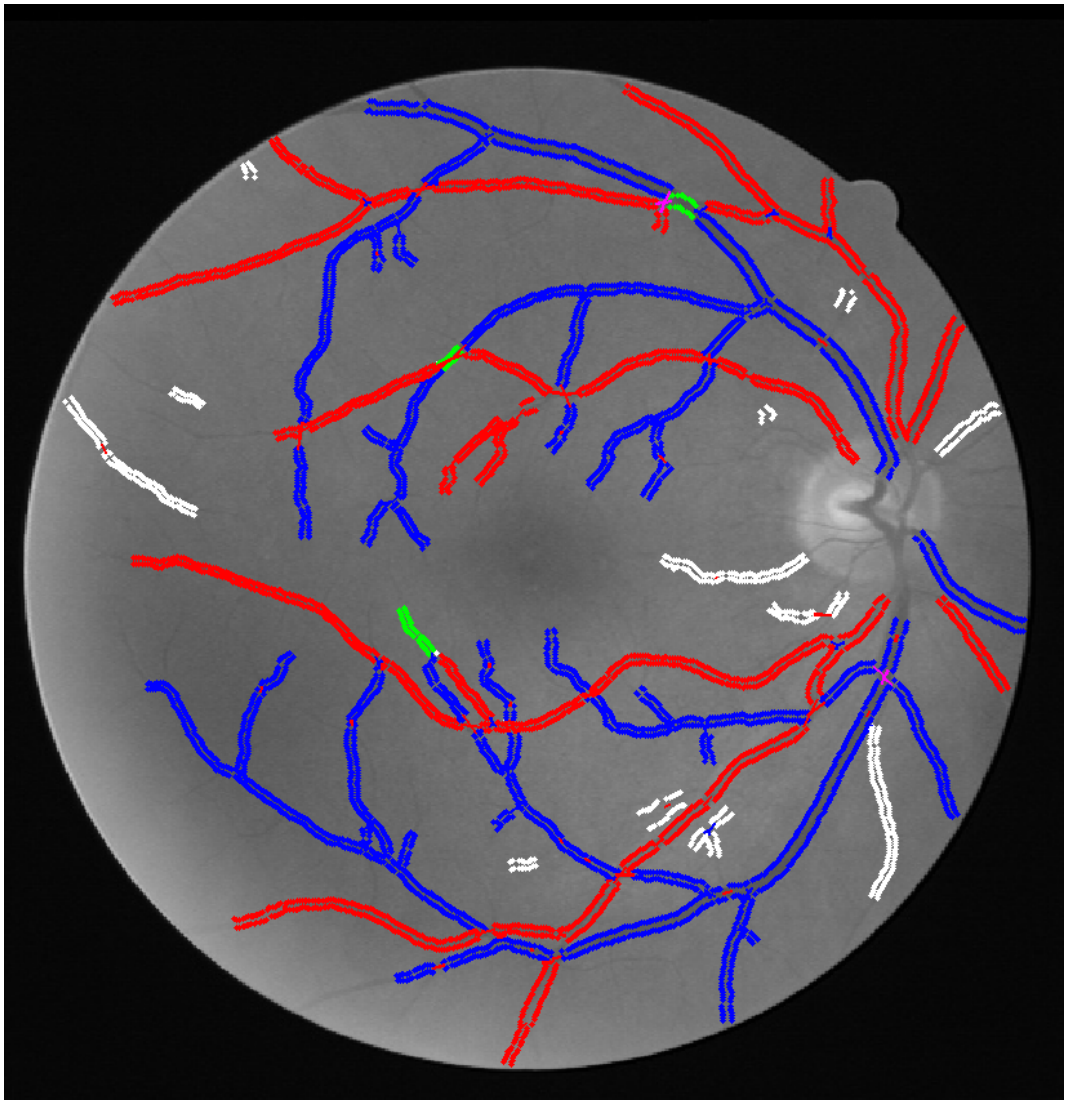

Fig. C.5 Image 5-$DSJS_1$

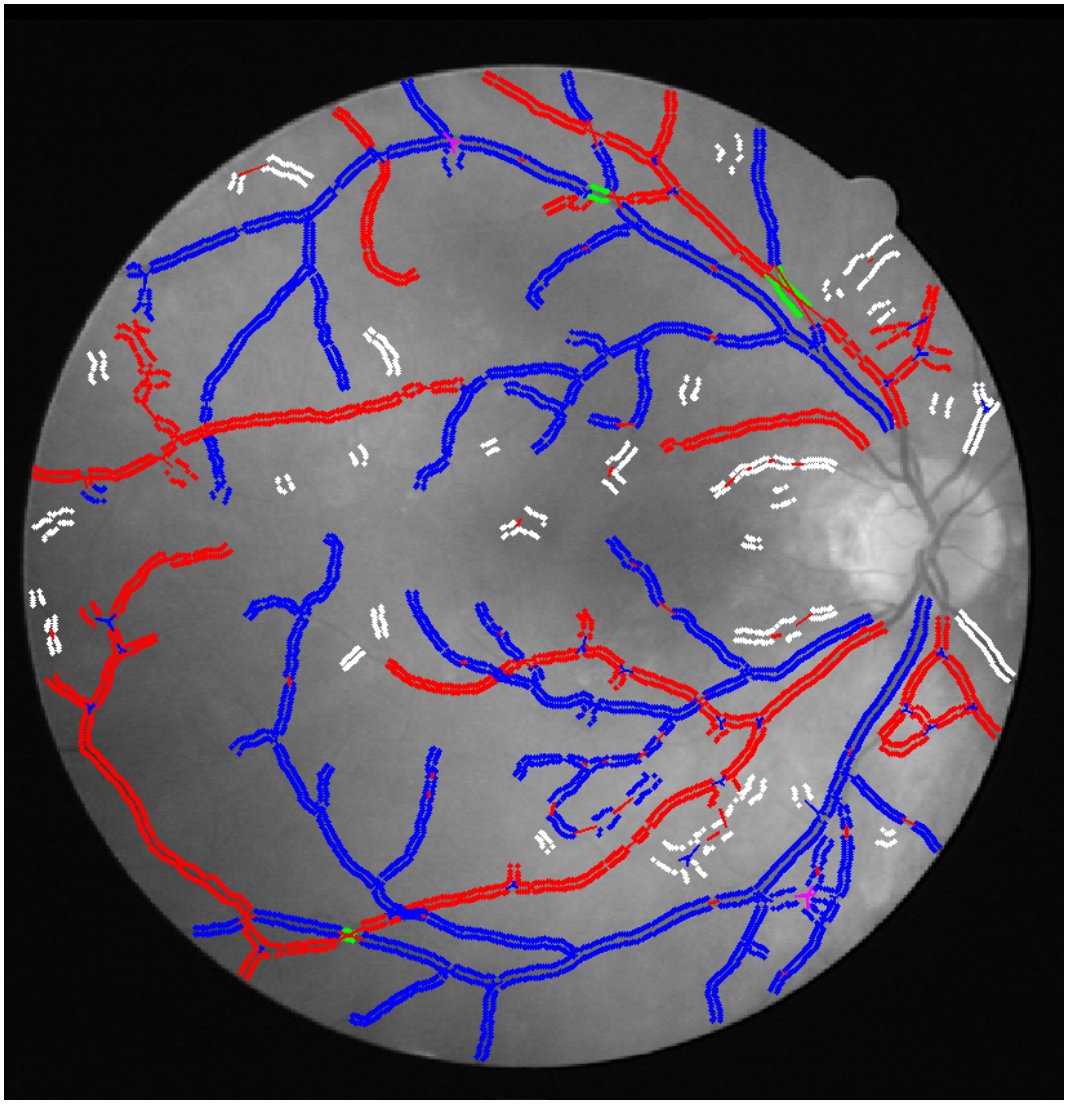

Fig. C.6 Image 6-$DSJS_1$

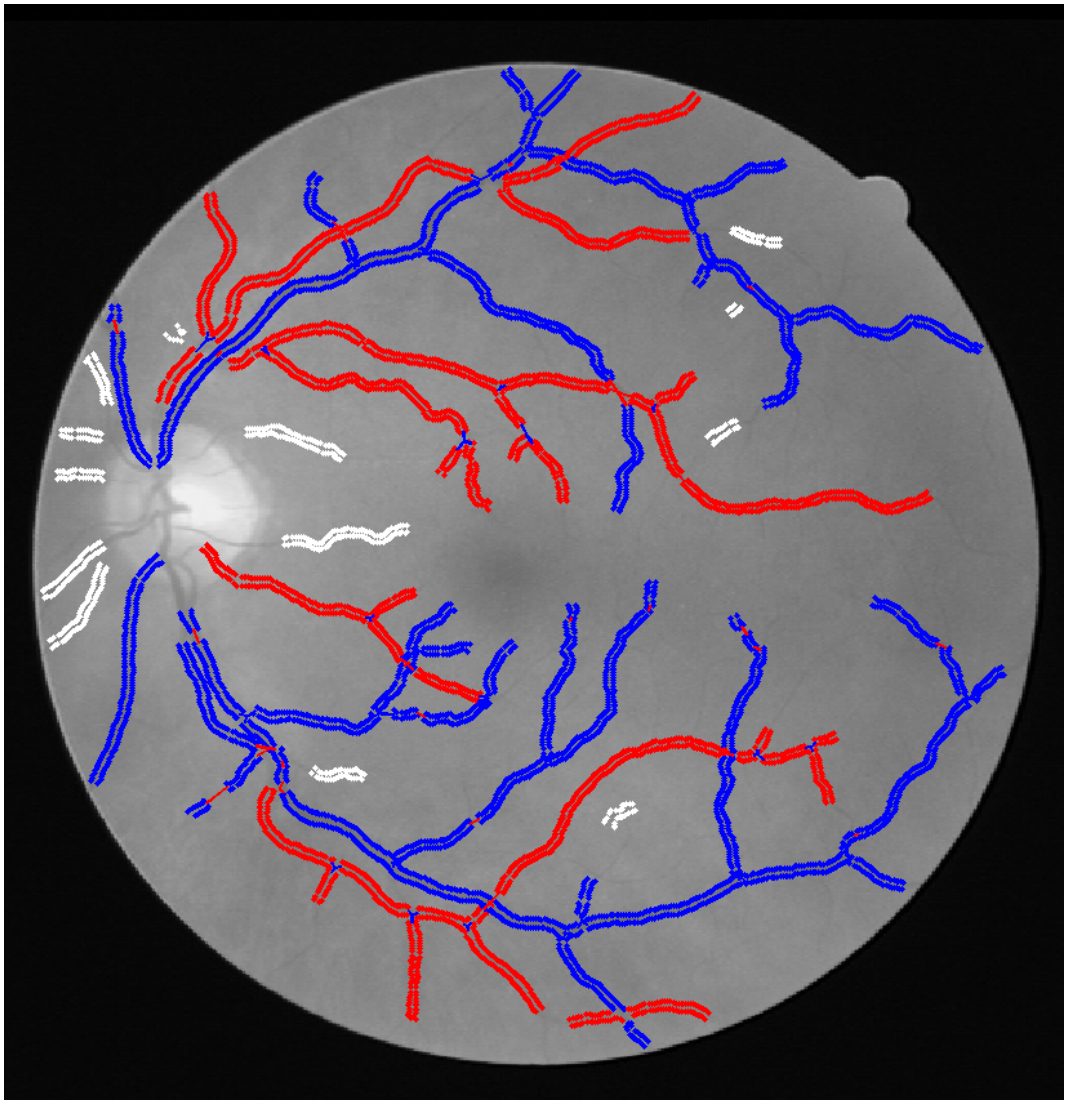

Fig. C.7 Image 7-$DSJS_1$